

© 2017

RUI LI

ALL RIGHTS RESERVED

**VOLTAGE-CONTROLLED TUNABLE SURFACE ACOUSTIC WAVEDEVICES
USING MULTIFUNCTIONAL MGZNO/ZNO STRUCTURES**

by

RUI LI

A Dissertation submitted to the

Graduate School-New Brunswick

Rutgers, The State University of New Jersey

In partial fulfillment of the requirements

For the Degree of

Doctor of Philosophy

Graduate Program in Electrical and Computer Engineering

Written under the direction of

Yicheng Lu

And approved by

New Brunswick, New Jersey

January, 2017

ABSTRACT OF THE DISSERTATION

VOLTAGE-CONTROLLED TUNABLE SURFACE ACOUSTIC WAVE DEVICES USING MULTIFUNCTIONAL MGZNO/ZNO STRUCTURES

By RUI LI

Dissertation Director:
Yicheng Lu

Surface acoustic wave (SAW) devices have been widely used for signal processing, frequency control, and sensing applications. It is also emerging as a promising technology for the miniaturized on-chip microfluidic pumping and biomolecule manipulation. Up to date, most SAW devices operate at fixed frequencies. The frequency tunability is highly demanded in advanced wireless communication and sensing systems for programmable and adaptive applications. The tunable SAW devices can extend the effective operating bandwidth, increase functionality and versatility, and reduce the architecture complexity.

The goal of this research is to demonstrate the voltage controlled tunable SAW devices using the multifunctional MgZnO- and ZnO-based multilayer structures. Two types of novel tunable SAW devices are designed and fabricated. The first device consists of the Ni-doped piezoelectric ZnO (NZO)/ *n*-type semiconductor ZnO/GaN/c-Al₂O₃ multilayer structure. The unique acoustic dispersion relationship in the ZnO/GaN

heterostructure generates the multi-mode SAW responses, facilitating high-frequency operation. The acoustoelectric interaction in the piezoelectric-semiconductor structure is used to realize frequency tuning through modulation of free charges in the semiconductor *n*-ZnO layer and confined charges in the *n*-ZnO/GaN heterojunction. A dc bias voltage is applied to a Ti/Au gate layer deposited on the path of SAW delay line to control the electrical conductivity for tuning the acoustic velocity. For a device operating at 1.25 GHz, the maximum SAW velocity change of 0.9% is achieved within -25 V to 0 V, equivalent to the frequency change of 11.2 MHz. This voltage-controlled frequency tuning device has potential applications. The ZnO/GaN-based tunable SAW device with a buried interdigital transducer (IDT) is also designed and fabricated. The device operates at 1.35 GHz with frequency tunability of 0.9% at a low biasing voltage range of -12V ~ 0V and expanded linear tuning range. This voltage-controlled frequency tuning device has potential applications in resettable sensors, adaptive signal processing, and secure wireless communication.

To extend the multifunctional MgZnO- and ZnO-based tunable SAW technology into the low-cost applications, such as radio-frequency identification (RFID), another prototype of voltage controlled tunable SAW device is directly built on glass substrates using the multifunctional MgZnO/ZnO structure. The dual-input-voltage-controlled tunable SAW device is formed by the integration of a piezoelectric NZO-based SAW delay line with a semiconducting MgZnO (MZO)-based thin film transistor (TFT). The IDT electrodes are buried under the NZO layer. It is found that the interface between MZO channel and SiO₂ gate dielectric layer of the TFT significantly impacts on SAW tuning performances. The MZO-SiO₂ interface is engineered by inserting an ultrathin MgO layer

as a barrier to stop Zn diffusion from MZO into SiO₂. The integrated TFT-SAW device with interface modification enables SAW frequency tuning of 0.53% under solely V_{gs} control. With extra V_{ds} control, the SAW frequency tunability is expanded its tuning range (0.46% - 0.63%). This dual input voltage controlled frequency tuning device on glass technology is promising for low-cost and portable applications such as smart sensors and reconfigurable RFID tags.

DEDICATED TO

My parents and my wife

Leishi Li and Yuchun Lu, who dedicate themselves to raise me and encourage me to

chase the future.

Meng Xia, who has been supportive since the first day we met.

ACKNOWLEDGEMENTS

I would like to express my special appreciation and thanks to my advisor Professor Yicheng Lu, whose invaluable guidance, insightful advice, and continuous encouragement enabled me to complete my doctoral studies and Ph.D. thesis. His tremendous mentorship has been laying down my foundation for future research and professional career.

I would like to sincerely thank my thesis committee: Prof. Jaeseok Jeon, Prof. Mehdi Javanmard and Prof. Dunbar Birnie for taking their valuable time on my thesis and their contributions on thesis modification. Their great encouragements, helpful advice, brilliant comments and insightful questions lead me to the thorough understanding of my research.

I want to express my appreciation to Dr. Paul Sheng, Dr. Lihua Zhang, and Dr. Kim Kisslinger, who provide me extensive help and guidance on device understanding and material characterizations.

I am also grateful to senior students in our group, Dr. Ziqing Duan, Dr. Pavel I. Reyes, Dr. Chieh-Jen Ku, Dr. Yang Zhang, and Dr. Nuri Emanetoglu. Their kind coaching, guiding, help and assistance in tool operation, process design, material characterization and development of research skills during the start of my Ph.D. study made me quickly involved in my Ph.D. research projects.

I wish to thank all my group members, including Mr. Wen-Chiang Hong, Mr. Faraz Khan, Mr. Tengei Xu, Mr. Tanvir Mohsin, Ms. Ke Tang, Ms. Szu-Ying Wang, Mr. Keyang Yang, Mr. Guangyuan Li, Mr. Yuxuan Li, Mr. Pengfei Ye and other previous senior

students, post-doctors and visiting scholars. Their discussion, collaboration, assistant, and friendship support me throughout my whole research life at Rutgers University.

This work was supported by the National Science Foundation under Grant No. ECS-1002178. A part of the research was carried out at the Center for Functional Nanomaterials, Brookhaven National Laboratory, which is supported by the US Department of Energy, Office of Basic Energy Sciences, under Contract No DE-SC0012704.

Table of Contents

Abstract	ii
Acknowledgements	vi
Table of Contents	viii
List of Tables	xi
List of Illustrations	xi
Chapter 1. Introduction	1
1.1 Motivation	1
1.2 Objectives	4
1.3 Dissertation Organization	5
Chapter 2. Technical Background	6
2.1 Piezoelectricity and SAW	6
2.2 Tunable SAW and Applications	11
2.2.1 Tuning through Variable Capacitors	12
2.2.2 Tuning through Modification of SAW Properties	13
2.2.3 Interaction of SAW and Film Conductivity in the Piezoelectric Semiconductor	18
2.2.4 Interaction of SAW and Thin Semiconducting Layer	21
2.3 ZnO, GaN and Its Heterojunction in SAW Applications	23
2.4 SAW and TFT Integration	29
2.5 Summary	31

Chapter 3. Tunable SAW Devices using ZnO/GaN	32
3.1 Device Structure and Physical Operation.....	32
3.2 Material Growth and Properties	36
3.2.1 ZnO Film Deposition.....	36
3.2.2 Material Characterizations.....	40
3.3 SAW Characteristics in ZnO/GaN-based Multilayer Structure	45
3.4 Frequency Tunability	48
3.5 The Effect of Buried IDT Design.....	57
3.6 Summary	75
Chapter 4. Tunable Surface Acoustic Wave Device Integrated with Thin Film Transistor Glass.....	77
4.1 Vertically Integrated TFT-SAW Device Structure	78
4.2 Material Characterizations	81
4.3 SAW Characteristics in NZO Piezoelectric Layer	83
4.4 Operation Principle	86
4.5 TFT Transfer Characteristics	87
4.6 Dual-Voltage Input for SAW Frequency Tuning.....	97
4.7 Summary	100
Chapter 5. Conclusions and Future Work.....	102
5.1 Conclusions	102

5.2 Suggestions for Future Work	104
5.2.1 Tunable SAW on ZnO/GaN Heterostructure	104
5.2.2 Tunable SAW on Multifunctional MZO/ZnO Structure	105
Appendix.....	107
References.....	109
Publications.....	119

List of Tables

Table 2. 1 Material constants of ZnO, AlN and GaN[10]	26
Table 3. 1 SAW velocity and piezo coupling coefficient of ZnO and GaN[67], [96].....	58
Table 3. 2 Simulated frequency range for 3rd HOWM using difference IDT configurations and NZO thickness.....	69

List of Illustrations

Figure 2. 1: Schematic of the sense of particle motions of (a) Rayleigh and (b) Love wave.	8
Figure 2. 2: A SAW device with a delay line employing two IDTs.	10
Figure 2. 3: A summary of current technologies for realizing the tunable SAW.	12
Figure 2. 4: Schematic drawing of a multi-IDT switching configuration. [1].....	14
Figure 2. 5: A traveling wave of electric field accompanies the traveling wave of potential. The E-field can extend above or underneath the piezoelectric at the distance of a wavelength. [42]	17
Figure 2. 6: Change in sound velocity $\Delta v/v_0$ (a) and attenuation coefficient per unit wave vector k ; (b) in units of effective coupling coefficient K^2 as a function of the ratio σ_d/σ_m	22
Figure 2. 7: (a) K^2 and (b) v for the 2 nd and 3 rd HOWMs propagating in ZnO/Al _x Ga _{1-x} N heterostructures on c-Al ₂ O ₃ ($x = 0, 0.5, 1.0$). [10].....	28
Figure 3.1: Schematic representation of the ZnO/GaN heterojunction based tunable SAW device structure fabrication flow chart.	35

Figure 3. 2 A schematic diagram of Rutgers MOCVD reactor for ZnO and $Mg_xZn_{1-x}O$ growth.	37
Figure 3. 3: A schematic diagram of an RF sputtering system in Rutgers MERL.	39
Figure 3. 4: PL spectrum of ZnO/GaN heterostructure measured at room temperature..	41
Figure 3. 5: XRD two theta scan spectrum of GaN template and ZnO/GaN heterostructure	42
Figure 3. 6: FESEM image of piezoelectric ZnO layer on top of GaN template.	43
Figure 3. 7: A ZnO/GaN heterostructure cross-sectional TEM image.	44
Figure 3. 8: The curves represent the SAW dispersion simulation results using the transmission line model. The symbols represent the testing results from the devices with the specific total thickness of Ni:ZnO and GaN (h) and the IDT period (P) in μm	47
Figure 3. 9: Simulation results of electromechanical coefficient K^2 of the Ni:ZnO/GaN SAW devices.....	48
Figure 3. 10: A representative SAW response in the Ni-ZnO/GaN structure shows the base wave mode and three higher order modes	49
Figure 3. 11: Normalized phase velocity change vs. bias voltage for the tunable SAW devices with various semiconductor n-ZnO thicknesses d_{ZnO} (50 nm and 120 nm). The inset is the measured SAW response, showing the center frequency of 1.245 GHz. The arrows point the bias voltages which result in full depletion of 50 nm and 120 nm n-ZnO layer, respectively.	51
Figure 3. 12: SAW attenuation as a function of bias voltage for devices with 50 nm and 120 nm semiconducting n-ZnO layer, respectively.	52

Figure 3. 13: A schematic drawing of conduction band energy levels in the Ni-ZnO/n-ZnO/GaN structure under the negative bias voltage.....	54
Figure 3. 14 The schematic cross-section of the tunable SAW device with (a) exposed and (b) buried IDT configuration.	59
Figure 3. 15 XRD Spectrum for NZO grown on an GaN/Al ₂ O ₃ template.	60
Figure 3. 16 SEM image of overall Au/Ti/NZO/n-ZnO/GaN/Al ₂ O ₃ structure. Inset: TEM image of n-ZnO/GaN interface.	61
Figure 3. 17: The schematic diagram of the NZO/ZnO/GaN-based tunable SAW devices process flow chart with (a) exposed IDT, and (b) buried IDT.....	63
Figure 3. 18: Top view of buried IDT SAW device.	64
Figure 3. 19 TLM simulation result of electromechanical coefficient K^2 of the 0.4 μm NZO/n-ZnO/GaN SAW devices with exposed IDT structure	65
Figure 3. 20 TLM simulation result of electromechanical coefficient K^2 of the 0.8 μm NZO/n-ZnO/GaN SAW devices with exposed IDT structure.	66
Figure 3. 21 TLM simulation result of electromechanical coefficient K^2 of the 1.5 μm NZO/n-ZnO/GaN SAW devices with exposed IDT structure.	67
Figure 3. 22 TLM simulation result of electromechanical coefficient K^2 of the 0.8 μm NZO/n-ZnO/GaN SAW devices with buried IDT structure.	68
Figure 3. 23: Typical transmission spectrum for the tunable SAW devices with exposed and buried IDT.....	72
Figure 3. 24: Normalized frequency changes vs. bias voltage for devices with exposed and buried IDT.....	73

Figure 3. 25: SAW attenuation coefficients as a function of bias voltage for devices with exposed and buried IDT, respectively.	74
Figure 4. 1: 3D schematic representation of the MgZnO based tunable SAW device on glass.....	78
Figure 4. 2: TFT settings in the z-x plane with S and D contacts.....	80
Figure 4. 3: SAW configuration in a y-z plane with IDT buried between SiO ₂ and piezoelectric NZO layer.....	80
Figure 4. 4: XRD patterns of c-oriented NZO film grown on a glass substrate.	82
Figure 4. 5: AFM image of an NZO film grown on a glass substrate.	82
Figure 4. 6: (a) Cross-sectional SEM image of NZO film directly grown on a glass substrate. (b) Bird view SEM image of NZO film directly grown on a glass substrate.	83
Figure 4. 7: The electromechanical coefficient K^2 versus operating frequency for TFT-SAW devices with different SiO ₂ thickness.	84
Figure 4. 8: The K^2 versus SiO ₂ layer thickness at the center frequency of 330 Mhz.	85
Figure 4. 9: Measured frequency change and measured I_{ds} - V_{gs} transfer characteristics of the regular MZO tunable SAW device. V_{ds} is fixed at 0.1 V.	89
Figure 4. 10: Measured frequency change and measured I_{ds} - V_{gs} transfer characteristics of the m-MZO tunable SAW device. V_{ds} is fixed at 0.1 V.	91
Figure 4. 11: (a) Cross-section TEM of SiO ₂ /MZO structure, the black arrows indicate the nanocrystal structure found in amorphous SiO ₂ ; (b) EDS line scan from MZO layer to SiO ₂ layer; (c) the EDS point detection results corresponding to the labeled positions at three locations in (a) and (b): MZO (green dashed box), interface (purple dashed circle), and SiO ₂ (dark blue dotted box).	93

Figure 4. 12: (a) Cross-section TEM of SiO ₂ /MgO/MZO structure; (b) EDS line scan from MZO layer to SiO ₂ layer; (c) EDS point spectrum results corresponding to the labeled positions at three locations in (a) and (b): MZO (green dashed box), MgO (purple dashed circle), and SiO ₂ (dark blue dotted box).	94
Figure 4. 13: Measured frequency change of the m-MZO-NZO tunable SAW device, and (b) SAW attenuation coefficients as a function of bias voltage V_{gs} . The different curve represents various V_{ds} voltage (-10 V, -5 V, 0 V, 5 V, 10 V).....	99
Figure 4. 14: Measured frequency change of the m-MZO-NZO tunable SAW device, and (b) SAW attenuation coefficients as a function of bias voltage V_{gs} . The different curve represents various V_{ds} voltage (-10 V, -5 V, 0 V, 5 V, 10 V).....	100

Chapter 1. Introduction

1.1 Motivation

A surface acoustic wave (SAW) is a type of acoustic wave travels along the surface of certain elastic material SAW devices normally contains one or more interdigital transducers (IDTs) to convert acoustic waves to electrical signals and vice versa by using the piezoelectric effect of certain materials. SAW devices are commonly used for radar, oscillators, domestic TV and mobile phone and the base station as RF frequency band filters. Also, SAW devices are employed in wide area network, wireless local area network communications, wireless passive identifications tags, touch screen, pressure/humidity/temperature/biochemical sensors. As one of the key components in the radio-front end devices, SAW has been applied in every single cell phone, from low-cost GSM handset to multimode multi-band LTE smartphones. The annual production of SAW devices is more than 4 billion units, with over 400 million dollars' market share in 2015.

In a SAW device, the signal frequency is determined by SAW velocity of the material and SAW wavelength. Most of SAW devices operate at the predetermined frequency without agility due to the fixed SAW velocity and wavelength. However, in many modern communication systems, the needs for multi-band and multi-mode devices are growing rapidly. For example, a high-end smartphone must separate the transmit and receive paths for 2G, 3G, 4G, LTE wireless signal, as well as Wi-Fi, Bluetooth, and GPS, using over 15 bands. Signals in the receiving paths must be isolated from one another. To realize these functionalities, a multi-band smartphone usually requires over ten filters and ten duplexers. Back to 2011, Samsung Galaxy S II smartphones have successfully integrated tunable RF end using ferroelectric capacitors and MEMS variable capacitors. A

tunable device such as an adaptive filter for signal processing is also desired for increased signal to noise performance and security concerns. It can extend the effective operating bandwidth, increase functionality and versatility, and reduce the architecture complexity. Furthermore, tunability in the time or frequency domain response is desirable for the system to adapt to its operating environment.

Lots of effort has been made to achieve the tunable SAW devices. Among them, filter banks with selectable IDTs provide frequency variations through switching between multiple filter channels by RF (radio frequency)[1] or mechanical switches.[2] However, the discontinuous frequency tuning and large device dimensions limit its applications in compact mobile systems. Another approach is perturbation of piezoelectric material properties such as stiffness coefficient through an external magnetic field[3] or a high voltage induced in-plane electric field.[4] Recently, Alzuaga et al. reported a tunable SAW device built on a single crystal SrTiO_3 substrate.[5] A 50 V dc voltage was superimposed with an RF signal to achieve -0.7% frequency variation at 2 GHz center frequency using electro-beam lithography with 1 μm minimum feature pattern. However, a threshold voltage of 10 V dc bias was required to initiate frequency tuning. Also, the frequency tuning behavior was single-directional due to charge trapping in SrTiO_3 when the bias polarity altered.

It has been proposed to realize voltage-controlled SAW velocity tuning by using acoustoelectric interaction in the piezoelectric-semiconducting dual layer structure.[6] In this structure, the longitudinal electric field accompanying SAW propagation along the piezoelectric layer interacts with free carriers in the semiconducting layer. This interaction results in acoustic wave attenuation and velocity change due to ohmic loss and piezoelectric

stiffening, respectively. Up to date, the tunable SAW devices operate at the MHz center frequency with a small frequency tuning range. A metal-insulator-semiconductor (MIS) SAW phase shifter based on an AlGaIn/GaN two-dimensional electron gas (2DEG) showed 0.07% velocity tuning.[7] J. Zhu et al. demonstrated a tunable SAW phase shifter built on the $\text{SiO}_2/n\text{-ZnO/piezoelectric ZnO/r-sapphire}$ structure. The device operated at 666 MHz with 0.62% velocity tuning (equivalent to frequency tuning of 2.9 MHz).[8] A velocity tuning range of 1.6% at 434MHz was reported using the epitaxial lift-off (ELO) and quantum well bonding techniques; however, the complicated process limited the yield and hindered technology from manufacturing and practical application.[9]

Another limitation of tunable SAW devices is the fabrication cost. Most tunable devices are built on single crystal substrate materials such as LiNbO_3 [3], [4], [6], [9], STO [5] and $\text{GaN/Al}_2\text{O}_3$ [7],[8] with high-quality 2DEG layer which requires high growth temperature and multi-step depositions. To further reduce the tunable SAW cost for a small distance, low-frequency operations such as indoor wireless sensors, RF tags for the internet of things (IOT). It is important to develop tunable SAW device on lost cost substrate, e.g. glass. Tunable SAW on glass provides the advantages of: (1) potential integration with display technology, especially SAW touch screen display; (2) large area and high volume manufacturing, compatible with current on-glass fabrication technology; (3) this technology is less dependent substrate material, so it is easy to apply on flexible glass or other flexible substrates for further wearable electronics.

Although AlGaIn/GaN material system can provide good quality of 2DEG and High Electron Mobility Transistor (HEMT), the process requirement and fabrication cost is still high. Zinc oxide (ZnO) is a wide bandgap semiconductor, several advantages make it a

good candidate for tunable SAW application: (1) its free exciton binding energy (60 meV) is much higher; (2) a large size native substrate is available; (3) wet etching is feasible; (4) epitaxial films can be grown at much lower temperature; (5) it shows higher radiation hardness; and (6) ZnO nanostructures can be grown on various substrates. Epitaxial ZnO films can be grown on GaN, as the lattice and thermal mismatches between GaN and ZnO are relatively small. By integrating two wide bandgap semiconductor materials ZnO and GaN together, the unique dispersion relationship in the ZnO/GaN structure enables higher-order SAW modes with a large coupling coefficient, high acoustic velocity, and low loss.[10] This structure generates a high frequency, high tunability programmable SAW device for GHz wireless communication and resettable RFID.

1.2 Objectives

In this work, we demonstrate a voltage-controlled SAW phase shifter based on the acoustoelectric interaction in a multilayer structure consisting of a Ni-doped piezoelectric ZnO layer and an *n*-type semiconductor ZnO layer grown on GaN/c-Al₂O₃. The unique acoustic dispersion relationship in ZnO/GaN allows the excitation of the high order SAW mode with high velocity for GHz frequency operation. Concomitantly, the acoustoelectric interaction enables the modulation of the SAW velocity, therefore, tuning the device operating frequency. We also study the effect of IDT location by comparing exposed and buried IDT structure. The results show buried IDT improves SAW operating frequency, increase tunability and reduce SAW propagation loss.

We also develop the tunable SAW device technology on glass to facilitate the low frequency and low-cost applications. Glass substrate is one of the major type low-cost, transparent supporting substrate which suits for large area production. A bottom gate thin

film transistor (TFT) is fabricated on a glass substrate for electric field tuning. SAW signal is generated on Ni:ZnO piezoelectric layer on top and launches along it. The frequency tuning is realized by both gate voltage V_{gs} and drain voltage V_{ds} . We also discovered the Zn diffuses into SiO₂ layer and cause the interface defects and fixed charge in the dielectric, further degrade the TFT performance. A MgO layer is chose as diffusion barrier layer to reduce the Zn intrusion effect. This is the first demonstration of tunable SAW device on glass integrated with TFT structure. It serves as a basic RF front end device for low cost, disposable RF tags, and encrypted communications.

1.3 Dissertation Organization

The motivations and objectives of this dissertation are given in Chapter 1. Chapter 2 introduces the technical background for this dissertation, including the concept of piezoelectricity and surface acoustic device, tunable SAW and its applications, acoustoelectric interaction, and the fundamental properties of ZnO, GaN, and their heterojunction. In Chapter 3, the design, fabrication, and testing of ZnO/GaN based voltage controllable SAW device are discussed in details. In Chapter 4, integrated tunable TFT-SAW built on the glass substrate is demonstrated. The interface between MgZnO and SiO₂ has been studied in detail to reduce the interface defects. Finally, conclusions and suggestions for future work are given in Chapter 5.

Chapter 2. Technical Background

2.1 Piezoelectricity and SAW

Piezoelectricity is the appearance of electrical charge (potential) across certain materials in response to applied mechanical stress, converting mechanical energy into electrical energy and vice versa. The generation of electrical polarization when a piezoelectric material is strained is known as the direct piezoelectric effect, first demonstrated by Pierre Curie and Jacques Curie in 1880 using Quartz and Rochelle salt. It is later understood as the linear electromechanical interaction between the mechanical and the electrical state and only occurs in hemimorphic crystals with no inversion symmetry.[11] The opposite effect, converse piezoelectric effect, refers to the generation of strain in a piezoelectric material when an electric field is applied, was mathematically deduced from fundamental thermodynamic principles by Gabriel Lippmann in 1881 and later confirmed by the Curies experimentally.

In the piezoelectric material, one important parameter used to evaluate the piezoelectricity is the electromechanical coupling coefficient. Due to the additional potential energy stored in each unit cell, a piezoelectric material has an augmented elastic stiffness effect compared to its non-piezoelectric counterpart. This stiffening increases the effective elastic stiffness coefficient by:

$$c_{stiffened} = c(1 + K^2) \quad (2.1)$$

where $K^2 = e^2 / c\varepsilon$ and c , e and ε are the elastic, piezoelectric and dielectric constants for the propagation direction of the acoustic wave in the solid, respectively. K^2 is defined as the electromechanical coupling coefficient, which is the measure of the conversion efficiency between electrical and acoustic energy in piezoelectric materials.

The first type of SAW, Rayleigh wave, was first demonstrated by Lord Rayleigh in 1885.[12] Later in 1911, the second waveform, Love wave, was described by Augustus Edward Hough Love and named after him. Surface waves result from the interaction of solid particle displacement in both longitudinal and shear directions, under constraints of physical boundary condition. In a Cartesian coordinate system, there are three possible particle displacements about the propagation direction, assuming the waves are launching in the z direction. As respect to wave propagation, the particle motion has three independent degrees of freedoms: (1) if the particle is polarized in z -direction parallel to the wave propagation in the z -axis, it is classified as compressional displacement. The particle motion consists of alternating compression and extension parallels to the direction of longitudinal propagation, until the wave propagates through it; (2) if the particle is polarized in the horizontal plane that perpendicular to the wave propagation in the z -axis, it is classified as shear-horizontal displacement (SH); (3) if the particle is polarized in the vertical plane that perpendicular to the wave propagation in the z -axis, the wave is classified as shear vertical displacement (SV). Each mode of surface acoustic waves must have at least two types particle motion out of three categories listed above. For example, the Rayleigh mode wave has both longitudinal and shears vertical particle displacement, while the Love wave mode has longitudinal and shear horizontal particle displacement, as shown in Fig. 2.1.[13] Overall, the generalized SAW (GSAW) has particle motion in the propagation direction and the two shear directions. Surface acoustic wave causes a small surface perturbation less than 20 angstroms, and the wave vanishes vertically within ten wavelengths. The velocity of SAW wave has a normal range of 2,500 -10,000 m/s and the frequency is in the ranges of 10 MHz -3 GHz.

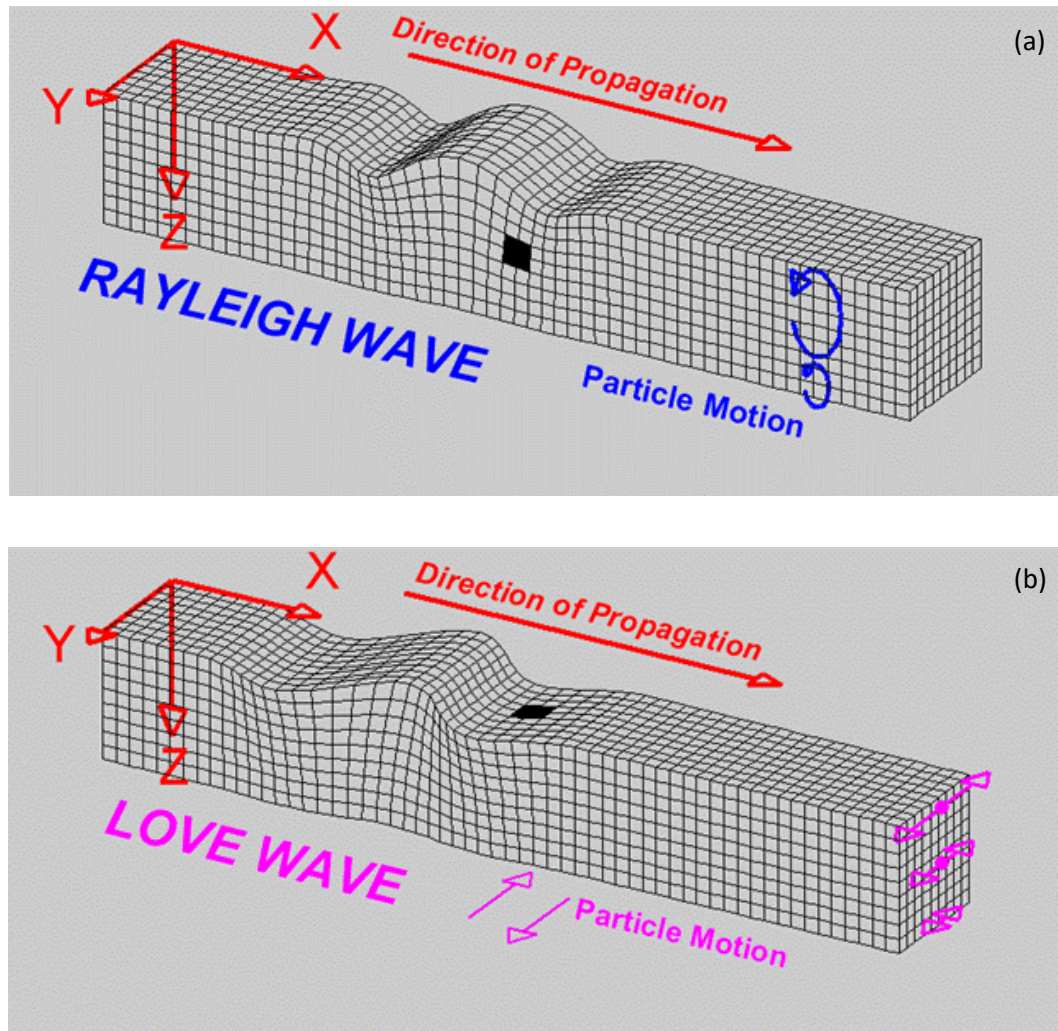


Figure 2. 1: Schematic of the sense of particle motions of (a) Rayleigh and (b) Love wave.

SAW technology, as applied to modern electronic systems, arose originally from radar technology however it was not extensively using in an electronic system and sensing until the 1960s. In 1965, White and Voltmer[14] demonstrated the basic SAW delay line structure by using two sets of thin metal spatially periodic electrode on a polished piezoelectric plate. Those electrodes consist of two interlocking comb-shaped arrays of metallic electrodes are referred to interdigital transducers (IDTs) and mostly used periodic electrode structures and sensors.[15] Starting from the 1980s, the SAW devices began to

be used for consumer electronics and in telecommunications. SAW devices have been made to meet the needs of acoustic filter technology[16] and later spanned fields of communication,[17] signal processing,[18], [19] chemical sensing.[20], [21] Recently SAW devices have been extensively studied in the biomedical related application, including single particle separation and manipulation[22], [23] and low-cost lab on chip bio-sensors.[24], [25]

Figure 2.2 shows the simplest type of SAW device with a delay line employing two IDTs, usually made of thin-film metal interleaved comb structures, on top of a piezoelectric substrate. The input IDT converts signal voltage variations into mechanical acoustic waves and the output IDT converts mechanical SAW vibrations back into output voltages. If an alternating electric field is applied to the comb structure, a time-harmonic periodic mechanical deformation is induced in the piezoelectric substrate underneath due to the voltage difference between two adjacent fingers. Thus, the transducer excites periodical mechanical deformation of the piezoelectric substrate and generates mechanical wave perpendicular to the finger direction. This mechanical wave propagates along the surface in both directions. The second set of IDT fingers receive the incoming wave and reversely convert the mechanical energy back to a suitably filtered electrical signal due to the piezoelectricity of the substrate.

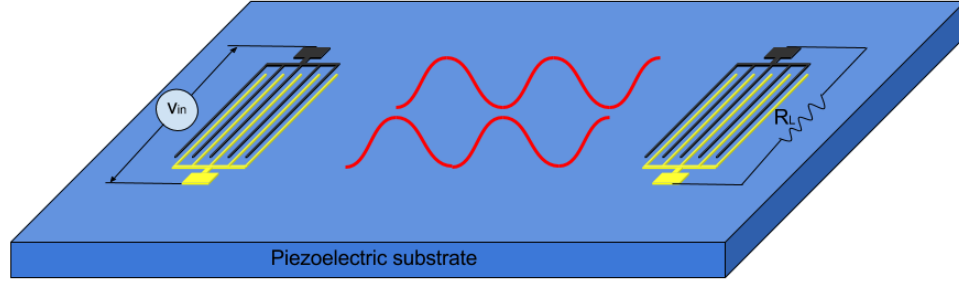


Figure 2. 2: A SAW device with a delay line employing two IDTs.

Considering applying a frequency variable input signal at input IDT and receiving the output signal at its counterpart. As the SAW propagates along the piezoelectric crystal surface SAW device provides the function of frequency filter by:

$$H(f) = H_1(f) H_2^*(f) L(f) = H_1(f) H_2^*(f) e^{-jkx(f)} = V_{output} / V_{input} \quad (2.2)$$

where $H_1(f)$ and $H_2(f)$ are individual responses of input and output IDTs, $H_2^*(f)$ is the conjugate of $H_2(f)$, $k=2\pi/\lambda$ is the wave vector and $x(f)$ is a frequency dependent separation between those segments of input and output IDTs that excited at frequency f . In a special case where input and output IDTs have uniform finger separation and finger apodization overlap, $x(f)$ can be reduced to a constant, which is the distance between two IDT sets midpoints.

In the design and application of SAW devices, the center frequency and 3dB bandwidth are the key parameters. For a SAW device, the wavelength λ is a structural parameter and quantitatively equals to the period (P) of the inter-digital transducers (IDTs). The basic relationship between acoustic velocity v_{SAW} , center frequency f_c , and wavelength λ is:

$$v_{SAW} = \lambda \cdot f_c \quad (2.3)$$

2.2 Tunable SAW and Applications

With the continuing explosive demands of mobile communications on a global scale, whether measured regarding users, handsets, data traffic, networks, frequency bands, ubiquitous, reliable wireless connectivity has never been more important. By keeping up with Moore's law scaling, the computing speed and storage capacity of computer and handset increase exponentially. However, the wireless data communication speed has been overlooked, and the traditional RF front-end architectures became the bottleneck of wireless communication technology.

A tunable RF function can be defined as whose target frequency of operation and performance parameters are dynamically adjustable by an external signal. However, current front-end architectures are generally "switchable" between separated components or modules. To achieve a high level of precision, digitalized software control and complicated circuit design has been used. In most commercial mobile phone contains at least one tunable RF function implemented using either microelectromechanical systems (MEMS) or ferroelectric based variable capacitors.

SAW technology has advantage of simple structure, few mask layers, and low cost. It has been serving 2G and 3G cell phone applications (all GSM bands and most CDMA bands) very well. On the other hand, while tunable SAW technology is arriving on the horizon, some electronic component manufacturers, including Motorola,[26] Qorvo (former TriQunt)[27] and Murata,[28] have already demonstrated the early state products. The proposed approaches mainly include three categories based on the operation mechanisms as summarized in Figure 2.3.

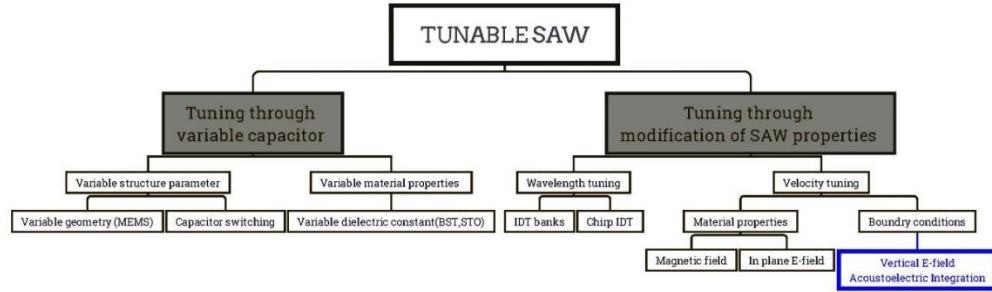


Figure 2. 3: A summary of current technologies for realizing the tunable SAW.

2.2.1 Tuning through Variable Capacitors

The existing methods to achieve tunability are usually through the modification of external components, such as connecting a nonprogrammable SAW to an additional variable device. In this approach, the tunability originates from another programmable device other than SAW itself. A SAW filter or resonator can be described using an RLC equivalent circuit. By adding variable capacitors (VCs) to each SAW device, it changes the effective capacitance through the external signal and enables the capability of continuous passband edges location adjustment. A variable capacitor is a capacitor whose capacitance may be altered through external control mechanically or electronically. In general, variable capacitor can be divided into two categories: MEMS VCs and ferroelectric thin films VCs. MEMS VCs are usually involved with movable mechanical components, which either changes the capacitance dielectric gap, area or performs the switching function between discrete capacitors. MEMS VCs have the advantage of high-quality factor (Q), while it suffers from complicated fabrications processes and slow tuning speed limited by mechanical movement.

Unlike the MEMS methods to change capacitor configuration, an alternative way to realize tunable capacitor is through variable physical parameter-dielectric constant.

Dielectric constant is independent of electrical field, however, for a special class of high permittivity materials, such as barium strontium titanate (BST)[29], [30] and Strontium titanate (STO),[30] the effect can be quite pronounced.

2.2.2 Tuning through Modification of SAW Properties

Tunability can also be achieved at device level without extra effects in designing more components. As described in Eqn. (2.3) $v_{SAW} = \lambda \cdot f_c$, the signal frequency is a function of SAW wavelength and SAW velocity, which provides two categories for tuning, 1) variable wavelength and 2) variable velocity.

(a) Wavelength Tuning:

The SAW wavelength is usually determined by the period of IDT (P), a fixed design parameter during fabrication. To achieve different wavelength, Zhu et al. placed 11 IDTs filter banks paralleled in the SAW propagation path. Desired time delay or frequency spectrum is achieved by selecting or combining various IDTs.[1], [31] Figure 2.4 shows the schematic diagram of the tunable SAW device with RF switch.

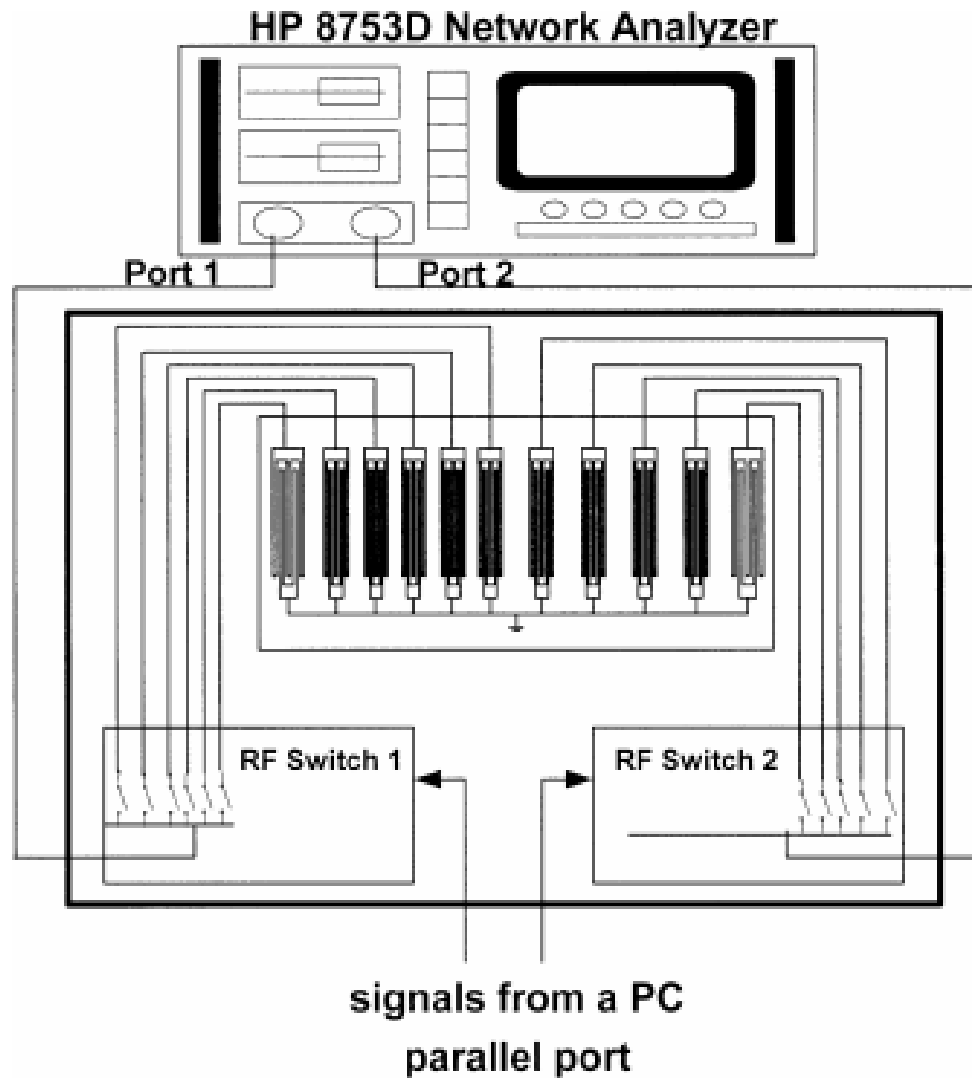


Figure 2. 4: Schematic drawing of a multi-IDT switching configuration. [1]

However, major drawbacks of filter bank approaches are 1) digitized, non-continuous tuning with a large time delay; 2) large device dimensions due the additional components. These drawbacks make the filter bank based tunable SAW filters impractical for some applications which require miniaturized components, such as cellular phones or wireless sensors. Chirp IDT structure can achieve a limited tunability at the cost of low wave intensity.[23], [32] A chirp IDT has a linear gradient in the pitch that allows it to

resonate at a wide range of frequencies, as shown in Figure 2.4. Thus it can generate of different wavelength waves by tuning the electric signals.

(b) Acoustic Velocity Tuning

In one-dimensional case, acoustic velocity can be solved using the wave equations:

$$\rho \frac{\partial^2 u}{\partial t^2} = c_{stiff} \frac{\partial^2 u}{\partial x^2} - \frac{e}{\varepsilon} \frac{\partial D}{\partial x}$$

$$u(x, t) = u_0 e^{i(kx - \omega t)}, \quad D(x, t) = D_0 e^{i(kx - \omega t)}$$

$$v_{oc} = \frac{\omega}{k} \tag{2.4}$$

Based on the partial differential wave equation, acoustic velocity is related to piezoelectric material properties and SAW propagation boundary conditions. The perturbation of piezoelectric material properties such as stiffness coefficient or strain stress will change the coefficient of the wave equation, thus change acoustic velocity. A magnetic field is applied to the magnetostrictive material adjacent to piezoelectric layer a relatively high tunability is achieved through the effective stiffness coefficient tuning by magnetic field.[3], [33]–[36] However, the feasibility of mobile application of this device is limited by the requirement of additional equipment for magnetic field generation. An alternative way to adjust the effective stiffness is through the electrical field when a dc voltage is applied on a piezoelectric film, perpendicular to SAW propagation direction. The electric field induced strain change will change the acoustic velocity. However, this electrical field is relatively small due to the large distance between to electrodes (mm), which resulted in either kV applied voltage[37] or ppm level tuning range.[38] A better solution was proposed recently by using a non-linear electrostriction single crystal SrTiO₃ (STO) substrate. A 50V dc control voltage superimposed with an RF signal, which induced up to

0.5 MV/cm electrical field between two IDT fingers.[5] -0.7% frequency variation at 2 GHz center frequency was achieved. However, it required a minimum 10 V dc bias as threshold voltage, which limited portable low power applications. Also, the tuning was single directional due to STO charge trapping related frequency shift when bias polarity altered.

It was proposed to realize voltage-controlled SAW velocity tuning by using acoustoelectric interaction in the piezoelectric-semiconducting dual layer structure.[6] In this structure, the longitudinal electric field accompanying SAW propagation along the piezoelectric layer interacts with free carriers in the semiconducting layer. This interaction results in acoustic wave attenuation and velocity change due to ohmic loss and piezoelectric stiffening, respectively. Up to date, this kind of tunable SAW devices operates at the MHz center frequency with a small frequency tuning range. A metal-insulator-semiconductor (MIS) SAW phase shifter based on an AlGaIn/GaN two-dimensional electron gas (2DEG) showed 0.07% velocity tuning.[7] J. Zhu et al. demonstrated a tunable SAW phase shifter built on the $\text{SiO}_2/n\text{-ZnO/piezoelectric ZnO/r-sapphire}$ structure. The device operated at 666 MHz with 0.62% velocity tuning (equivalent to frequency tuning of 2.9 MHz).[8] A velocity tuning range of 1.6% at 434MHz was reported using the epitaxial lift-off (ELO) and quantum well bonding techniques; however, the complicated process limited the yield and hindered technology from manufacturing and practical application.[9]

(c) Acoustoelectric Interaction

Due to the coupling of mechanical and electrical properties, the mechanical wave propagates along the piezoelectric substrate will induce a traveling wave potential $\Phi(x, y, t)$ at the surface, as shown in Figure 2.5. The spatial variation of surface potential

$\Phi(x, y, t)$ creates electric fields E along both perpendicular and longitudinal directions of SAW launching. The perpendicular component $E_y = \partial\Phi/\partial y$ extends above or beneath the surface by a distance on the order of one acoustic wavelength.[39] This phenomenon of mechanical energy loss/conversion is also referred as piezoelectric stiffening, meaning given the total amount of energy, compared with the non-piezoelectric material, less deformation is induced. So the piezoelectric matter “seems” to be stiffer. The quantitative method to describe energy conversion in piezoelectric material is achieved by define the electromechanical coupling coefficient $K^2 = E_{\text{converted}}/E_{\text{total}}$, as a measure of the strength of the piezoelectricity of a given material. It is also provided by $K^2 = e^2 / c\epsilon$.

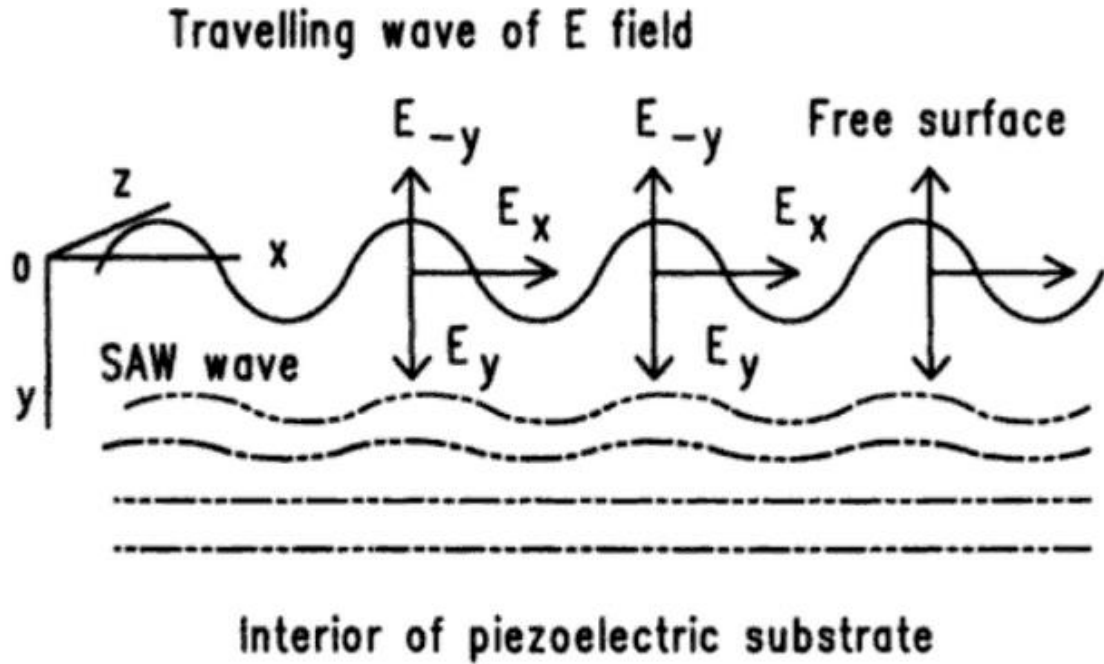


Figure 2. 5: A traveling wave of electric field accompanies the traveling wave of potential. The E-field can extend above or underneath the piezoelectric at the distance of a wavelength. [39]

2.2.3 Interaction of SAW and Film Conductivity in the Piezoelectric Semiconductor

The basic equations which govern the propagation of the acoustic wave in the piezoelectric semiconducting medium can be described using the mechanical stress T and the electrical displacement D with the mechanical strain S and the electric field E and the coupled equations (A.6) and (A.7) in appendix. For some applications, we can effectively reduce complexity by considering one-dimensional wave equations. Under one dimensional condition, the equations are:

$$T(x,t) = cS(x,t) - eE(x,t) \quad (2.5)$$

$$D(x,t) = eS(x,t) + \varepsilon E(x,t) \quad (2.6)$$

Where c , ε , and e are respectively the elastic constant at the constant electric field, the dielectric permittivity at constant strain, and the piezoelectric constant, which are spatial and time independent in homogenous materials.

In a homogenous material with no the body forces, the equation of motion describes the relationship between displacement $u(x,t)$ and mechanical stress $T(x,t)$ is:

$$\frac{\partial T(x,t)}{\partial x} = \rho \frac{\partial^2 u(x,t)}{\partial t^2} \quad (2.7)$$

Also:

$$S(x,t) = \frac{\partial u(x,t)}{\partial x} \quad (2.8)$$

where ρ is the mass density. The one-dimensional longitudinal wave equation is

$$\rho \frac{\partial^2 u}{\partial t^2} = c \left(1 + \frac{e^2}{c\varepsilon} \right) \frac{\partial^2 u}{\partial x^2} - \frac{e}{\varepsilon} \frac{\partial D}{\partial x} \quad (2.9)$$

(a) Open Circuit Condition

Considering a SAW is launching on top of an idea piezoelectric material with zero conductivity ($\sigma=\infty$) along the x -axis.

As no net charge existing on the piezoelectric material surface ($Q=0$), Poisson's equation requires the derivative of the electric displacement to be zero ($\frac{\partial D}{\partial x}=0$). Eqn. (2.9)

is reduced to:

$$\rho \frac{\partial^2 u}{\partial t^2} = c \left(1 + \frac{e^2}{c\epsilon} \right) \frac{\partial^2 u}{\partial x^2} \quad (2.10)$$

The general plane wave solution with time dependency is in the form of:

$$u(x,t) = u_0 e^{i(kx - \omega t)} \quad (2.11)$$

Where $u(x,t)$ is the mechanical displacement amplitude, k is wave vector, ω is the angular frequency of the wave and $v = \omega/k$ is acoustic velocity. Combining Eqn. (2.10) and (2.11), we can derive the acoustic velocity:

$$v_{oc} = \frac{\omega}{k} = \sqrt{\frac{c \left(1 + \frac{e^2}{c\epsilon} \right)}{\rho}} = \sqrt{\frac{c(1 + K^2)}{\rho}} \quad (2.12)$$

(b) Short Circuit Condition

Assuming the piezoelectric surface with infinite conductivity ($\sigma=\infty$), which shields the internal electric field. The piezoelectric effect disappears due to electrical loss. Thus, the piezoelectric constant e is zero. The wave equation (2.10) reduces to:

$$\rho \frac{\partial^2 u}{\partial t^2} = c \frac{\partial^2 u}{\partial x^2} \quad (2.13)$$

which describes a longitudinal sound wave in a medium appearing to be non-piezoelectric. The acoustic velocity is called short circuit velocity and given by:

$$v_{sc} = \frac{w}{k} = \sqrt{\frac{c}{\rho}} \quad (2.14)$$

Combining Eqn. (2.12) and (2.14)

$$\frac{v_{oc} - v_{sc}}{v_{oc}} = \frac{\sqrt{\frac{c(1+K^2)}{\rho}} - \sqrt{\frac{c}{\rho}}}{\sqrt{\frac{c(1+K^2)}{\rho}}} = 1 - \frac{1}{\sqrt{(1+K^2)}} \quad (2.15)$$

As electromechanical coupling coefficient K^2 is usually less than 5%, applying second order Taylor expansion, K^2 can be expressed as in Eqn. (2.24) to obtain K^2 value experimentally.

$$K^2 \approx 2 \frac{v_{oc} - v_{sc}}{v_{oc}} \quad (2.16)$$

(c) Limited Conductivity Condition

Considering a piezoelectric semiconductor layer with finite conductivity ($0 < \sigma < \infty$), the acoustoelectric interaction between the semiconductor and longitudinal electric field accompanying the SAW will have two effects on the acoustic wave. 1) The surface acoustic wave is attenuated due to ohmic losses; 2) The surface acoustic velocity is altered by the effective piezoelectric stiffening of the material. The propagation of the SAW in piezoelectric semiconductor with homogeneous bulk conductivity can be described by a frequency dependent relaxation-type model.[40], [41]

Defining the conductivity relaxation frequency

$$\omega_c = \frac{\sigma}{\varepsilon_1 + \varepsilon_2} \quad (2.17)$$

Where ω_c is the conductivity of the semiconductor, ε_1 and ε_2 are the dielectric constants of the piezoelectric substrate and the half-space above it, respectively the reciprocal of ω_c called dielectric relaxation time τ_c . The acoustic velocity and insertion loss are controlled ω_c in the form of:

$$\nu = \nu_0 \left(1 + \frac{e^2 / 2c\varepsilon}{1 + (\omega_c / \omega)^2} \right) \quad (2.18)$$

$$\Gamma = \frac{\omega}{\nu_0} \frac{e^2}{2c\varepsilon} \frac{(\omega_c / \omega)}{1 + (\omega_c / \omega)^2} \quad (2.19)$$

2.2.4 Interaction of SAW and Thin Semiconducting Layer

Consider a thin semiconductor layer with finite conductivity ($0 < \sigma < \infty$) is located on top of perfect piezoelectric surface where acoustic wave is launching. Assuming all the mobile carriers are confined to a conductive layer of thickness d , which is much smaller than the wavelength of the SAW λ in the following analysis. Due to the presence of surface charges, the longitudinal electric field of the SAW will be shielded at the piezoelectric surface, i.e., $z=0$. However, with depth into the material, the screening effect disappears, and SAW potential will recover first and until where the effect of surface conducting layer becomes negligible.

The electric field in the homogeneous bulk semiconductor decreases exponentially with depth ($E(z) \sim E_0 e^{-kz}$). $k = 2\pi/\lambda$ is the SAW wave vector for a homogeneous semiconductor. For the thin semiconducting layer, the available thickness to carry the current is defined as d . The current is only confined near the interface. The effective conduction thickness is reduced by the factor of kd . Thus, both the effective resistance and the time constant τ_0 becomes $1/kd$ times larger:

$$\tau_c = \frac{\tau_0}{kd} = \frac{\varepsilon_1 + \varepsilon_2}{\sigma \cdot kd} \quad (2.20)$$

$$\omega_c = \frac{kd \cdot \sigma}{\varepsilon_1 + \varepsilon_2} = \frac{\sigma_d k}{\varepsilon_1 + \varepsilon_2} = \frac{\omega \sigma_d}{\frac{\omega}{k}(\varepsilon_1 + \varepsilon_2)} = \frac{\omega \sigma_d}{v_0(\varepsilon_1 + \varepsilon_2)} = \frac{\sigma_d}{\sigma_m} \omega \quad (2.21)$$

where τ_0 is the time constant for a piezoelectric semiconductor with conductivity σ , $\sigma_m = v_0 (\varepsilon_1 + \varepsilon_2)$ is the conductivity at which the maximum loss occurs. The fact that here the conductivity is restricted to a thin sheet results effectively in a modification of the relaxation frequency.

The acoustic velocity change and insertion loss now are:

$$\frac{\Delta v}{v_0} = \frac{v - v_0}{v_0} = \frac{K^2}{2} \frac{1}{1 + (\omega_c / \omega)^2} = \frac{K^2}{2} \frac{1}{1 + (\sigma_d / \sigma_m)^2} \quad (2.22)$$

$$\Gamma = k \frac{K^2}{2} \frac{(\omega_c / \omega)}{1 + (\omega_c / \omega)^2} = k \frac{K^2}{2} \frac{\sigma_d / \sigma_m}{1 + (\sigma_d / \sigma_m)^2} \quad (2.23)$$

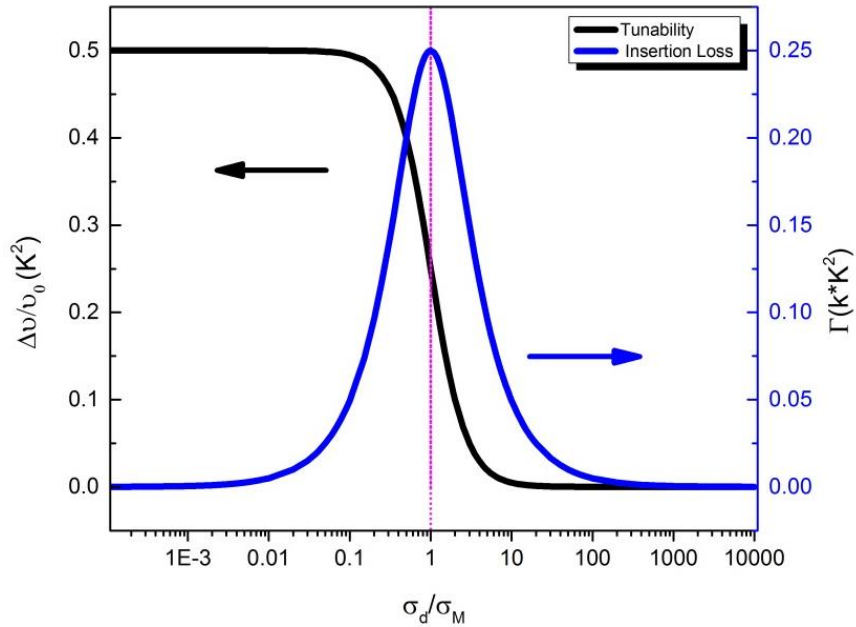


Figure 2. 6: Change in sound velocity $\Delta v/v_0$ (a) and attenuation coefficient per unit wave vector k ; (b) in units of effective coupling coefficient K^2 as a function of the ratio σ_d/σ_m .

2.3 ZnO, GaN and Its Heterojunction in SAW Applications

As a direct wide bandgap semiconductor ($E_g \cong 3.3$ eV at 300K), ZnO has attracted increasing attentions due to its multifunctional properties. Through proper doping or alloying, ZnO can be made semiconducting, piezoelectric, transparent and conducting, or ferromagnetic, leading to versatile applications. A low loss and high electromechanical coupling piezoelectric ZnO film can be obtained through compensation doping such as Li and Ni. Piezoelectric ZnO has a large electromechanical coupling coefficient, widely used in BAW and SAW devices for wireless communication and signal processing since early 70s.[42], [43] ZnO films have been used in conjunction with various substrates, including Al_2O_3 , [44], [45] SiC, [46], [47] diamond, [48], [49] Si, [50], [51] GaAs [52], [53] and quartz. [54], [55] ZnO has several advantages over GaN: (i) its free exciton binding energy (60 meV) is much higher; (ii) a large size native substrate is available; (iii) feasible to wet etching; (iv) epitaxial films can be grown at much lower temperature; (v) it shows higher radiation hardness; and (vi) ZnO nanostructures can be grown on various substrates. Despite these advantages, the development of ZnO as a semiconductor material is still in the research stage, mainly due to the lack of device-quality and controllable p-type doping.

With the development of deposition technology, GaN becomes a primary wide bandgap semiconductor for optoelectronics, particularly in blue LEDs and lasers.[56] GaN-based materials are also attractive for high temperature and high power electronic devices. However, several challenges remain for GaN technology, such as relatively high density of defects in GaN films for laser applications,[57] high-temperature deposition processes,[58] non-availability of large size bulk crystals, and difficulties in wet chemical etching. GaN, AlN, and their ternary $Al_xGa_{1-x}N$ are piezoelectric materials. AlN thin films

have been used for bulk acoustic wave (BAW) thin film resonators.[59], [60] The SAW properties of $\text{Al}_x\text{Ga}_{1-x}\text{N}$ thin films have been investigated as a function of the film composition and substrate material.[10] It has been demonstrated that ultra-high velocity SAW modes with moderate coupling coefficient in AlN and GaN thin films deposited on SiC, diamond, or sapphire substrates can be used for GHz-band mobile communication applications.[61]–[64] The AlN/c- Al_2O_3 structure has a high SAW velocity of 5,910 m/s, a moderate electromechanical coupling coefficient K^2 of about 0.3% and zero-temperature-coefficient-of-delay (TCD) with precise control of AlN thickness.[65], [66] SAW devices on GaN/c- Al_2O_3 with a high velocity of 5,803 m/s, relatively low insertion loss of -7.7 dB, and temperature coefficient of frequency (TCF) of -18.3 ppm/°C in the range of -25 to 50°C have been demonstrated.[67], [68] The 2DEG created within the AlGaIn/GaN heterostructure as the active component in creating SAW, and their RF characteristics are investigated.[69], [70]

Epitaxial ZnO films can be grown on GaN, as the lattice and thermal mismatches between GaN and ZnO are relatively small. The small lattice mismatch between ZnO and GaN ensures a lower defect density of ZnO grown on GaN, in comparison to ZnO grown on sapphire. Research efforts have been made to use ZnO buffer layers for GaN growth on substrates such as sapphire.[71]–[73] ZnO epitaxial thin films have been grown on epitaxial GaN buffer layers on Si.[74] The band alignment of ZnO/GaN heterostructure has been investigated for hybrid optoelectronic devices.[75] A Type-II band alignment was reported, with the valence band maximum of GaN above that of ZnO. The band offsets, ΔE_v , ranged between 0.6 eV to 1.0 eV, depending on the surface preparation. Electrical characteristics of ZnO/GaN heterostructures were measured, showing the formation of confined sheet

carrier at the interface caused by the large band discontinuity in the n-ZnO/n-GaN heterojunction.[76] Hybrid devices reported to date include the use of ZnO as a transparent conductive oxide electrode for GaN,[77] and n-ZnO/p-GaN heterojunction LEDs.[78] J. Zhong et al. have demonstrated an n-ZnO nanotips/p-GaN heterostructure blue-LED, and an integrated ZnO TCO and nanotips/GaN LED with enhanced light emission efficiency.[79]

GaN and ZnO both belong to the wurtzite crystal class, with similar lattice parameters. The material constants of ZnO, AlN, and GaN are shown in Table 2.1. By combining ZnO and GaN, higher order wave modes with large coupling coefficient and high acoustic velocity can be obtained. Through proper doping by Ni, a high-quality piezoelectric ZnO film can be achieved by RF sputtering.[80] The acoustic velocity of ZnO (3,300 m/s) is small than that of GaN (6,000 m/s). The integration of a piezoelectric ZnO with GaN offers additional advantages of higher-order overtone SAW modes with high acoustic velocity and thus high frequency, described as “slow on fast” phenomena.[81] These multilayer structures can be used to realize high frequency and low loss SAW devices.

Table 2. 1 Material constants of ZnO, AlN and GaN[10]

Property		ZnO	AlN	GaN
Lattice Parameter (Å)	a	3.243	3.11	3.189
	c	5.206	4.98	5.185
Density (kg/m ³)	ρ	5720	3255	6095
Elastic Stiffness (GPa)	C ₁₁	157	411	374
	C ₁₂	89	149	106
	C ₁₃	83	99	70
	C ₃₃	208	389	379
	C ₄₄	38	125	101
	C ₆₆	34	131	134
Piezoelectric Constant (C/m ²)	e ₃₁	-0.51	-0.58	-0.2
	e ₃₃	1.22	1.55	0.29
Dielectric Constant	ϵ_{11}	7.57	9	9.5
	ϵ_{33}	9.03	11	10.4
Spontaneous Polarization (C/m ²)	P _{sp}	-0.057	-0.081	-0.034

Y. Chen et al. showed the high frequency and low loss filters could be achieved by ZnO/Al_xGa_{1-x}N (0≤x≤1)/c-Al₂O₃ structures.[10] The layered structure ZnO/Al_xGa_{1-x}N/c-Al₂O₃ (0≤x≤1) provides flexibility to tailor acoustic properties by altering the Al composition, x, in Al_xGa_{1-x}N, and the thickness ratio of ZnO to Al_xGa_{1-x}N. The simulation results in Figure 2.7 show dispersive properties of phase velocity v_{SAW} and piezoelectric coupling coefficient K^2 versus the thickness-frequency product (hf) of 2nd and 3rd higher order wave modes (HOWMs). The K^2_{max} of the 2nd HOWM is estimated to be 4.26% for ZnO/GaN and 3.79% for ZnO/AlN. The hf bandwidth of 2nd HOWM, in which the coupling

coefficient is within $\pm 0.3\%$ of K_{max}^2 , is calculated to be 820 m/s for ZnO/GaN, and 1340 m/s for ZnO/AlN. The hf bandwidth of 3rd HOWM for ZnO/AlN is about 2280 m/s. Also, the $h_{ZnO}f$ bandwidth of the 2nd and 3rd HOWMs broadens with the increasing thickness ratio of $\text{Al}_x\text{Ga}_{1-x}\text{N}$ to ZnO. In comparison to $\text{Al}_x\text{Ga}_{1-x}\text{N}$ film, ZnO/ $\text{Al}_x\text{Ga}_{1-x}\text{N}$ multilayer structure offers advantages of multiple wave modes and broader bandwidth (due to larger hf bandwidth of 2nd and 3rd waves), useful for designing and realizing the high frequency, low loss, and large bandwidth SAW devices.

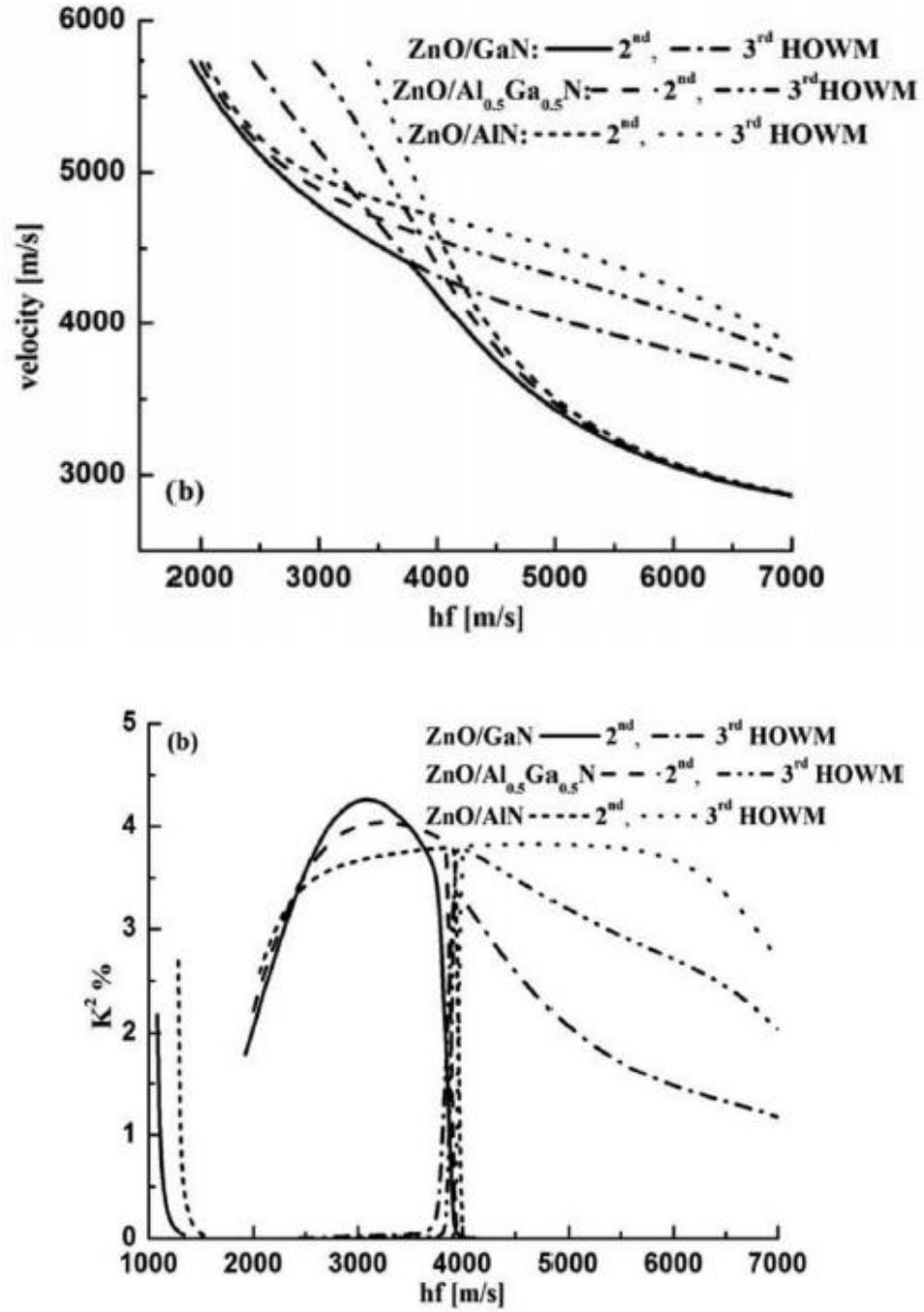


Figure 2. 7: (a) K^2 and (b) v for the 2nd and 3rd HOWMs propagating in ZnO/Al_xGa_{1-x}N heterostructures on c-Al₂O₃ ($x = 0, 0.5, 1.0$). [10]

2.4 SAW and TFT Integration

A thin-film transistor (TFT) is a special kind of field-effect transistor made by depositing thin films of a semiconductor active layer as well as the dielectric layer and metallic contacts over an insulating supporting substrate. In display technology, transistors are embedded within the panel itself, reducing crosstalk, which causes contrast difference in some areas, between pixels and improving image stability. Other applications include photovoltaics, embedded power sources, sensing devices, smart labels, lighting, and integrated logic devices. Hydrogenated amorphous silicon (a-Si:H) and polycrystalline silicon (poly-Si) TFTs are the industry standard for the switching and drive circuitry of monolithic active matrix liquid crystal display (AMLCD) and active matrix organic light emitting diode (AMOLED) technology. Overwhelming advantages for poly-Si TFTs are motivated by the need to address low electron field effect mobility ($<1 \text{ cm}^2\text{-V}^{-1}\text{S}^{-1}$) associated with a-Si TFTs. However, undesirable high off-state leakage current ($>10^{-10}\text{A}$) and high processing temperature are challenges in poly-Si TFT development. As novel displays require low power consumption, high resolution, large area, and fast refresh rate, Si-based TFTs cannot be utilized in novel 3D and high-definition (HD) displays. There has been increasing interest in the use of oxide-based TFTs as electronic backplane switching devices for the next generation large area flat-panel display applications.

The integration of SAW and three-terminal transistors was firstly demonstrated as analog buffer memory or memory correlator in the 1990s. The SAW could operate at ultra-high frequency however the digital/analog system was comparatively slow, the MOSFET or MESFET is connected to delay line as a switch for signal tapping and storage.[82]–[88] Later in the 2000s, with the development of high-quality single crystal heterostructure,

monolithic integration of SAW devices with active HEMTs on AlGaIn/GaN heterostructures has been widely studied for the compact system-on-chip (SOC) solutions for wireless transceivers and sensors. Most SAW and transistor integrations are still based on the connection of individual devices and non-tunable. Ivan Rýger et. al. developed a chemical gas sensor use either SAW or HEMT for separate sensing.[89] Xing Lu et. al. demonstrated an integrated SAW oscillator using GaN SAW and a five stage AlGaIn/GaN HEMT amplifier.[90] Similarly, Oshiyama Satoshi et al. designed a SAW resonator using AlGaIn/GaN HEMT as an amplifier.[91] Lei Shao et. al. reported direct integration of SAW and HEMT: emission and detection of SAW using AlGaIn/GaN HEMT. The source and drain of HEMT are employed as a single pair IDT to emit and receive SAW signal. The results showed when HEMT was biased in a saturation region, and 2DEG channel was pinched off, the variation of carrier density due to gate voltage change will cause the rapid change of AC impedance.[92] Up to date, no direct integration of tunable SAW device and TFT has been reported.

Voltage tunable SAW is achieved by acoustoelectric integration effect: SAW velocity is modulated by the sheet conductivity of a semiconducting layer adjacent to the piezo surface through an electrical field. Current tuning methods mostly use vertical voltage as single input, through space charge tuning by MIS capacitor or Schottky barrier.[7], [8] Employ TFT to modulate conducting layer will provide fast charge accumulation and depletion to increase the tuning speed, as well as introduce another parameter, V_{ds} , to form a double input tuning device, which will increase the security level of encrypted programmable communication, such as frequency-hopping spread spectrum.

2.5 Summary

In this chapter, a technical background review for this dissertation is presented. First, the principle and development of the traditional surface acoustic devices and their applications in telecommunications and sensors are presented. The high-performance tunable RF filters are a key component for realization of programmable RF front-end. The acoustic tunability is essential in many applications, such as programmable radio-frequency identification (RFID), adaptive signal processing, secure wireless communication, and resettable sensors. A comprehensive review of various approaches for achieving the tunability of SAW devices, including through external capacitors, change of material properties, and SAW propagation boundary conditions are conducted. Their advantages and disadvantages are analyzed. It is found that the tuning of free carriers in a semiconductor adjacent to SAW propagating in a piezoelectric layer using acoustoelectric interaction provides an efficient way to realize the SAW tuning. Such tunable SAW technology could extend the device functionality and generate novel electronic and sensing applications.

Chapter 3. Tunable SAW Devices using ZnO/GaN

To fulfill the increasing demand for advanced wireless communication and sensing systems for programmable and adaptive applications, a ZnO-based tunable SAW device is designed, fabricated and demonstrated in this research. The basic structure of the ZnO tunable SAW device consists of a piezoelectric ZnO SAW device integrated with an n-ZnO/GaN heterostructure. With a top electrode, the Ni:ZnO layer functionalized as an insulating layer and form an MIS structure with n-ZnO/GaN underneath. The total sheet conductivity is modulated through gate voltage tuning. The device fabrication procedure is described in this chapter. The performance of the prototype device is evaluated with respect to the acoustic velocity tunability, attenuation changeover external bias. The correlation between the space charge density and tunability is presented and discussed based on MIS and heterojunction model.

3.1 Device Structure and Physical Operation

The structure of a prototype tunable SAW chip using ZnO/GaN heterostructure grown on c-sapphire is schematically described Figure 3.1. In this device, ZnO/GaN tunable acoustoelectronic devices have unique advantages over the $\text{Al}_x\text{Ga}_{1-x}\text{N}/\text{GaN}/\text{c-Al}_2\text{O}_3$ and ZnO/MgZnO counterparts, including:

- (i) It can use higher order wave modes due to the dispersion in ZnO/GaN multilayers; leading to high frequency (multi-GHz) operation.
- (ii) Possessing higher acoustic velocity and larger electromechanical coupling coefficient (K^2) over a broad frequency range.
- (iii) Offering broad tunability at a low bias voltage, much better than the existing devices. By combining the filter banks (for selecting the center frequency) with the tunable

SAW (for fine tuning at the center frequency, $> \sim 2\%$ SAW velocity tuning), the tuning range can be dramatically increased for wide adaptive signal processing and flexible applications.

(iv) It is cost-effective, as the device excludes the high quality thick piezoelectric $\text{Al}_x\text{Ga}_{1-x}\text{N}$ layers and its quantum wells grown under high temperature and low growth rate.

The ZnO tunable SAW device fabrication procedure mainly includes 1) MOCVD growth of n-ZnO layer; 2) Ni:ZnO deposition by RF-sputtering; 3) top electrode patterning and 4) SAW aluminum IDT patterning. Multiple processing techniques are used in the device fabrication including photolithography, wet etching, e-beam evaporation and Al etching.

The surface cleaning process is required between all the steps using an ultrasonic cleaner. The sample cleaning process involves:

- (i) Clean in acetone for five mins.
- (ii) Clean in methanol for five mins.
- (iii) Clean in DI water for five mins.
- (iv) Dry the substrate out with ultra-pure nitrogen.
- (v) Bake the surface at 100°C under nitrogen ambient.

After cleaning of $4\text{-}\mu\text{m}$ -thick n-type GaN/c- Al_2O_3 ($n=6\times 10^{16}\text{ cm}^{-3}$) substrate, an n-type semiconductor ZnO layer (n-ZnO) with a carrier concentration of 10^{17} cm^{-3} is deposited by metal-organic chemical vapor deposition MOCVD at $\sim 500^\circ\text{C}$. The n-ZnO layer thickness is varied (50, 70, 100, and 120 nm) to study the effect of semiconducting layer thickness on the SAW velocity tuning. For exposed IDT structure, although only the n-ZnO layer under gate metal is necessary for charge tuning, no ZnO etching is performed.

This is because the transparency of c-Al₂O₃ provides not enough contrast of 50 nm ZnO layer for optical contact mode lithography in next gate pattern alignment. In next step RF sputtering of Ni:ZnO is directly deposited on n-ZnO without any structure patterning. A Ti/Au (100nm/50nm) layer is formed by electron beam deposition and patterned as top gate using traditional lift-off process. It serves as the gate, on which a dc bias is applied to modulate the vertical electric field in the n-ZnO layer, forming an MIS structure. Finally, on top of piezoelectric ZnO layer, IDT patterns with a period (P) of 5-12 μm are formed by electron beam deposition of an Al layer (150 nm) followed by selective wet chemical etching. There are 20.5 electrode pairs for each IDT. To determine the dispersion characteristics of the SAW modes, the thickness of the Ni-ZnO varies (0.4, 0.8, and 1.5 μm). The delay line, which is defined as the edge-to-edge distance between IDTs, has a value of 1,200 μm . The IDT apertures are 178 μm plus $P/2$ for all devices, with an electrode spacing of $P/4$.

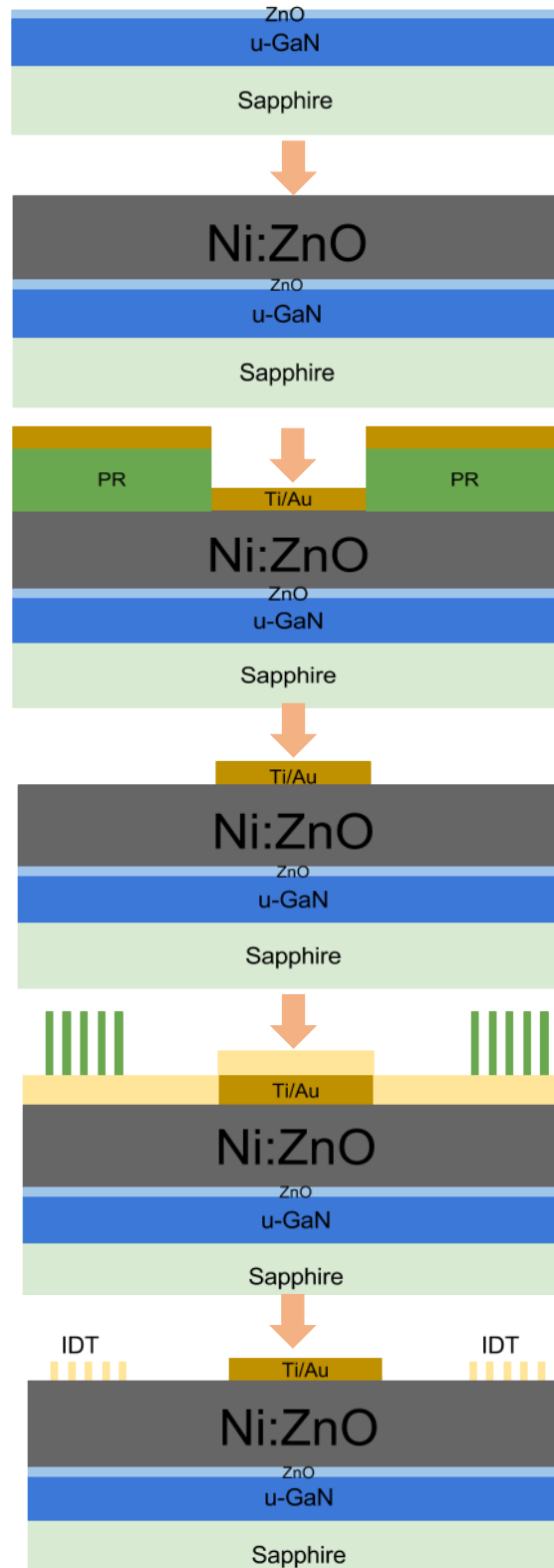


Figure 3.1: Schematic representation of the ZnO/GaN heterojunction based tunable SAW device structure fabrication flow chart.

3.2 Material Growth and Properties

3.2.1 ZnO Film Deposition

ZnO film can be grown both by MOCVD and Sputtering. MOCVD has many advantages such as controllable in-situ doping, available large-area uniformly deposition, high growth rate. Using Rutgers MOCVD system, we can achieve semiconducting ZnO films with high quality. The as-grown ZnO films show intrinsic n-type conductivity with carrier concentration above $\sim 10^{17} \text{ cm}^{-3}$, and resistivity of 1 to 100 $\Omega\text{-cm}$. We choose MOCVD grown ZnO as electrical tuning layer to form ZnO/GaN heterostructure. The n-ZnO is deposited at 500~550 °C, using diethyl zinc $(\text{C}_2\text{H}_5)_2\text{Zn}$ and oxygen as Zn and O precursor, respectively. Ultra-high purity (UHP) Argon gas is used as the carrier gas, which flows through the precursor's bubblers to carry the vapor of precursors into the reactor. In the MOCVD growth of ZnO-based films, one of the major obstacles is the gas phase reaction. The reactions between diethylzinc and oxygen can occur even at room temperature. The particles generated get incorporated into the deposited films, degrading film crystallinity and morphology. To reduce the pre-reaction caused particles, two procures are introduced into MOCVD chamber separately, and 10000 sccm N_2 are dumped from the top chamber as a purge gas to push two precursors down to sample surface, as shown in Fig. 3.2 The MOCVD chamber is pumped a rough pump, and the best vacuum that can be achieved by this system is about 10^{-2} Torr.

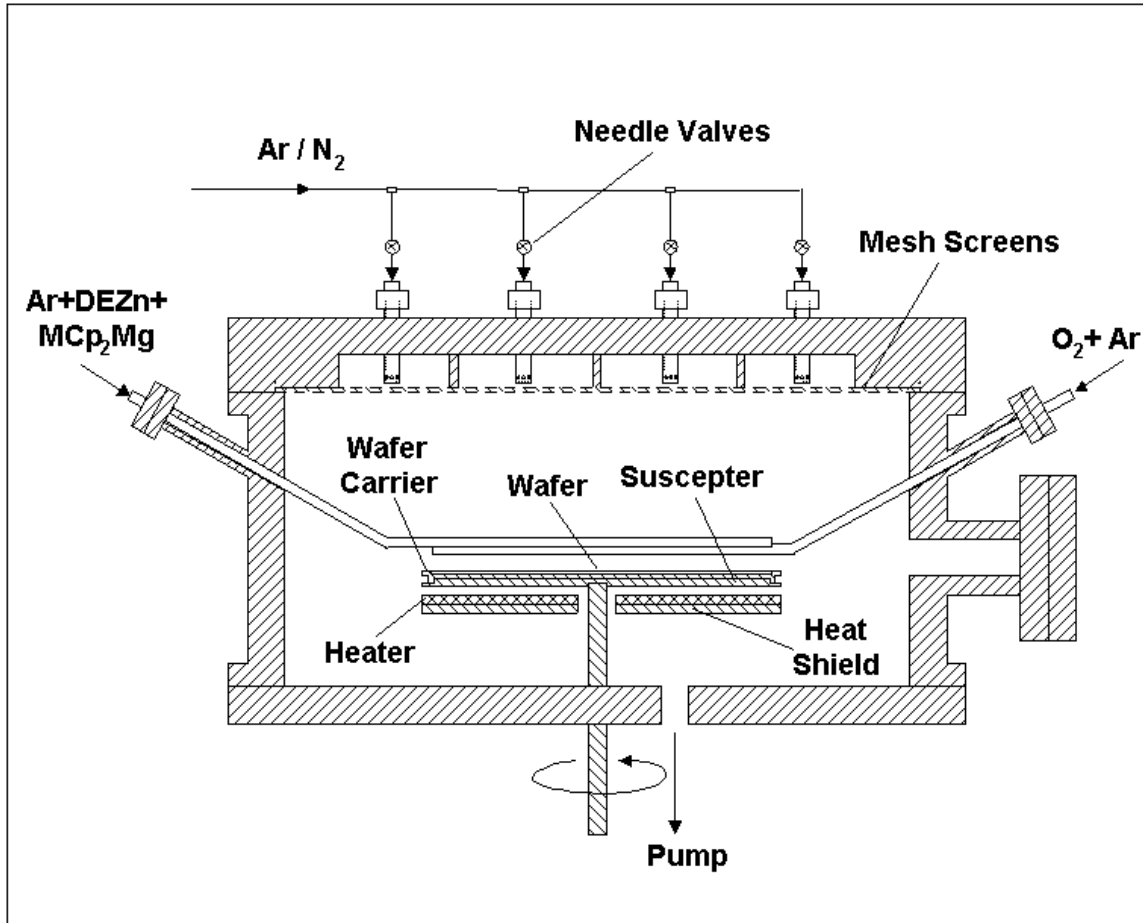


Figure 3. 2 A schematic diagram of Rutgers MOCVD reactor for ZnO and $\text{Mg}_x\text{Zn}_{1-x}\text{O}$ growth.

To achieve good SAW response, in the development of the ZnO/GaN tunable SAW device, it is critical to deposit high-quality piezoelectric ZnO layer. 1) The thickness of the piezoelectric layer determines the excitation of the multiple wave modes and maximal effective electromechanical coupling coefficient. 2) The uniformity and surface roughness of the piezoelectric layer impact the insertion loss of the SAW and the interface quality between piezoelectric and semiconducting ZnO layer. 3) The conductivity of the piezoelectric layer induces a constant ohmic loss that increases insertion loss. However, in MOCVD growth technique, as all the metal-organic precursors have the OH bonds, the

unintentional incorporation of impurities such as hydrogen is inevitable, act as shallow donors. It has been shown that interstitial H forms a strong bond with O in ZnO[93] or substitutes for O in ZnO[94] to form oxygen vacancy, acts as a shallow donor. Therefore, background n-type carrier concentration in ZnO films grown by MOCVD is usually higher than that of sputtered ZnO films. As discussed in the paragraph, MOCVD grown ZnO film has a resistivity range between 1 to 100 Ω -cm. At this low resistivity, ohmic loss dominates and causes high insertion loss of the acoustic wave, which makes MOCVD grown ZnO incompatible with SAW device. Thus, Sputtering ZnO with compensatory doping is required to achieve efficient piezoelectricity with resistivity larger than 10^7 Ω -cm. In comparison with various dopants. We decide to use Ni^{2+} to compensate the excessive carriers to achieve excellent piezoelectricity. Ni is more stable than Li as Li has a large diffusivity in ZnO which results in redistribution problem in the multilayer structure, especially during later subsequent processes. The ionic radii and the valence states are important factors in determining their solubility behavior. Ni can exhibit an oxidation state of Ni^{+2} which can easily substitute Zn^{+2} due to similar ionic radii in 4-fold tetrahedral coordination and are therefore expected to have a very high solubility in ZnO.

A thick piezoelectric ZnO film is deposited by RF sputtering on top of the buffer layer. The RF sputtering targets are prepared by mixing ZnO and NiO (2-3% wt) powder for compensation doping to achieve piezoelectricity. The sputtering chamber is equipped with a standard RF power source. The substrates are rotated and heated to $\sim 125^\circ\text{C}$. Deposition is carried out in a controlled ambient mixture of Ar and O_2 in ratio 1:4, with the overall chamber pressure, is maintained at $\sim 7 \times 10^{-3}$ Torr. Typical deposition rates range

from 0.2 – 0.3 $\mu\text{m/hr}$ due to the low deposition temperature. No post thermal annealing is needed.

The piezoelectric Ni:ZnO is deposited using RF sputtering system in Rutgers MERL. As shown in Figure 3.3. The chamber is equipped with a standard 13.56MHz RF power source on the bottom and a substrate holder, substrate heater and substrate rotation on the top. Ar and O₂ are flown into the chamber from the side as indicated in Fig 3.3. A standard RF power is applied to the sputtering gun and the substrate holder. The distance between the sputtering gun and the substrate holder is maintained at 15 cm to achieve the optimized across wafer uniformity with the help of the substrate rotation.

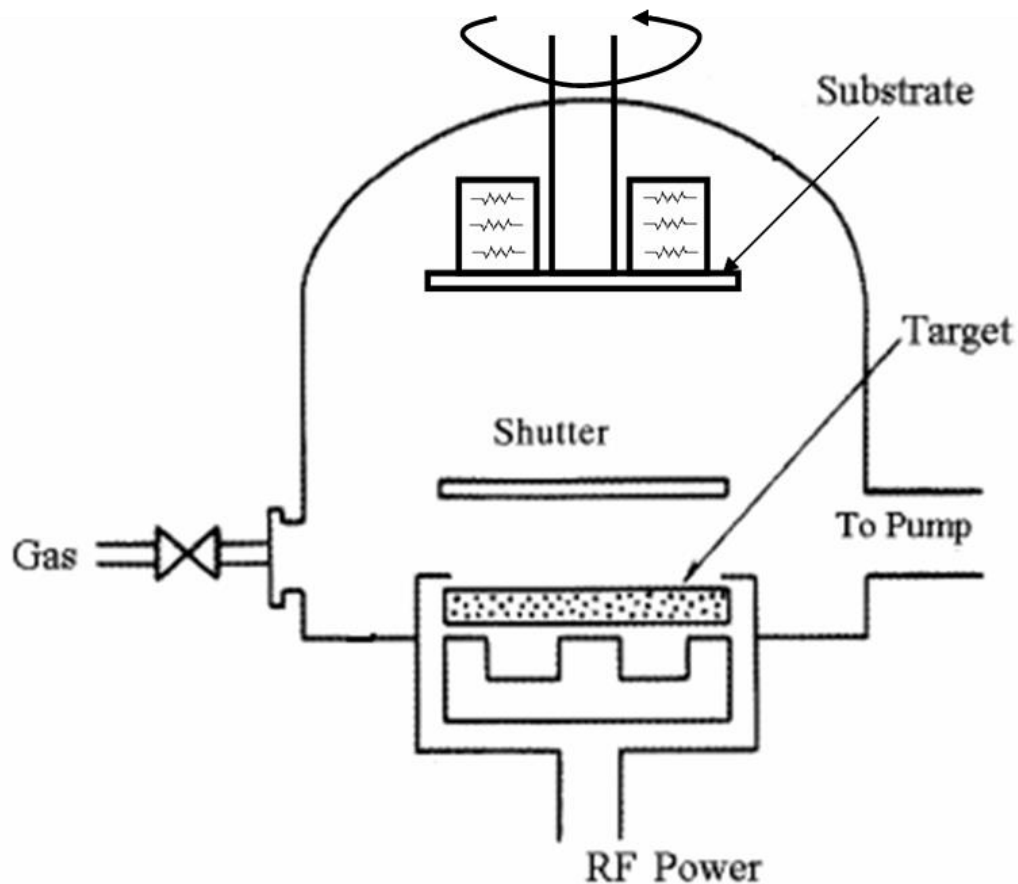


Figure 3. 3: A schematic diagram of an RF sputtering system in Rutgers MERL.

The targets were prepared by mixing the appropriate quantities of 99.995% pure ZnO and NiO. The mixture was cold-pressed using a 3 inch die into 2-inch pellets. The pellets were then sintered at 1100°C in air for 24 hours. After being cleaned in acetone and methanol, the sintered pellets were put on the backing plate using Zirconia glue. The chamber is maintained at a base pressure level of 10^{-6} Torr before the deposition. A mixture of 1:4 Ar and O₂ gasses is fed into the chamber during the deposition at the processing pressure of 7×10^{-3} Torr. The substrate temperature is set at 125 °C to maintain a low thermal budget process.

3.2.2 Material Characterizations

Microstructural characterizations of ZnO are performed by X-ray diffraction (XRD) and Photoluminescence (PL), Scanning Electron Microscopy (SEM) and Transmission Electron Microscopy (TEM). Figure 3.4 shows the room-temperature photoluminescence (PL) spectrum of GaN/c-Al₂O₃ and *n*-ZnO/GaN/c-Al₂O₃ structure. A deep level emission is seen in GaN/c-Al₂O₃ at a 500-600nm wavelength, while a strong near band edge PL peak of ZnO is seen at 3.29 eV with a full-width half maximum of 107 meV. No deep level emission is observed, indicating the ZnO high quality. Figure 3.5 shows XRD scan indicating the excellent crystallinity of ZnO and GaN films. The epitaxial relationship between ZnO and GaN is (0002) ZnO || (0002) GaN. The scanning electron microscopy (SEM) shows a cross section of a ZnO film grown on GaN template (Figure 3.6). An obvious columnar structure is observed along c-axis (0001) direction, which consistent with previous XRD spectrum. The high-resolution cross-sectional bright field transmission electron microscopy (BF-TEM) image of a ZnO/GaN heterojunction in Figure 3.7 shows an atomically flat interface between *n*-ZnO and GaN.

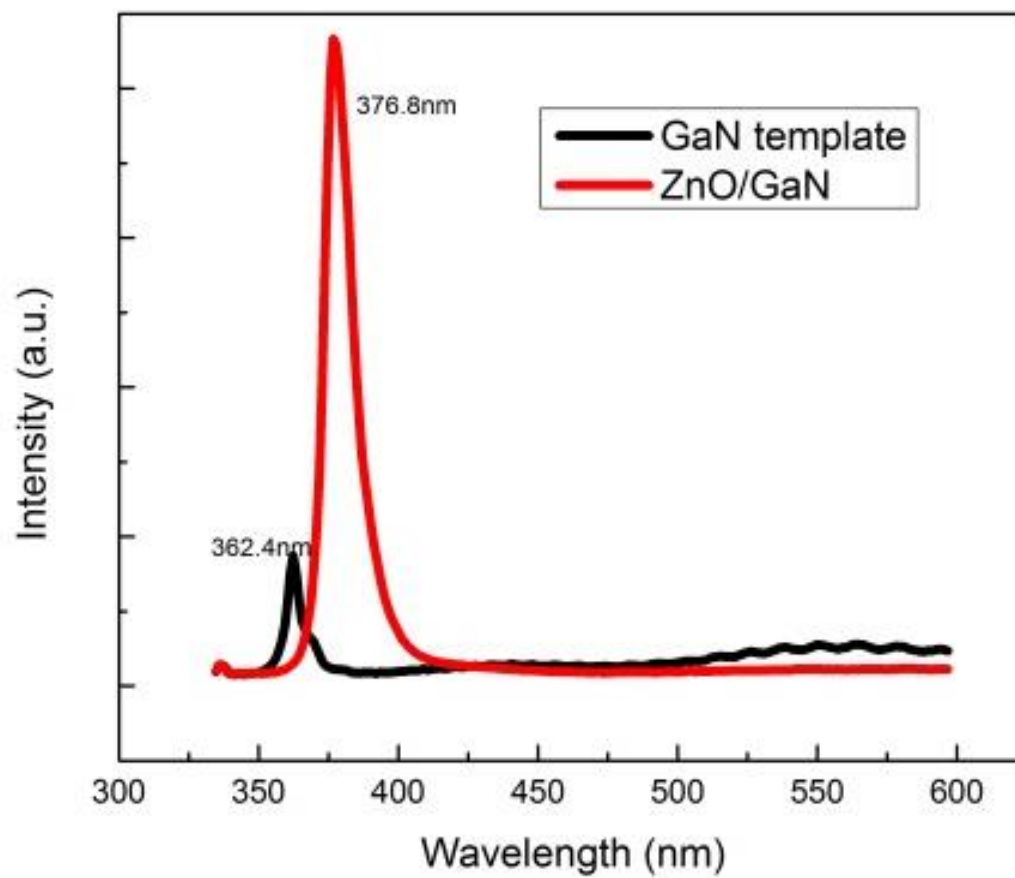


Figure 3. 4: PL spectrum of ZnO/GaN heterostructure measured at room temperature.

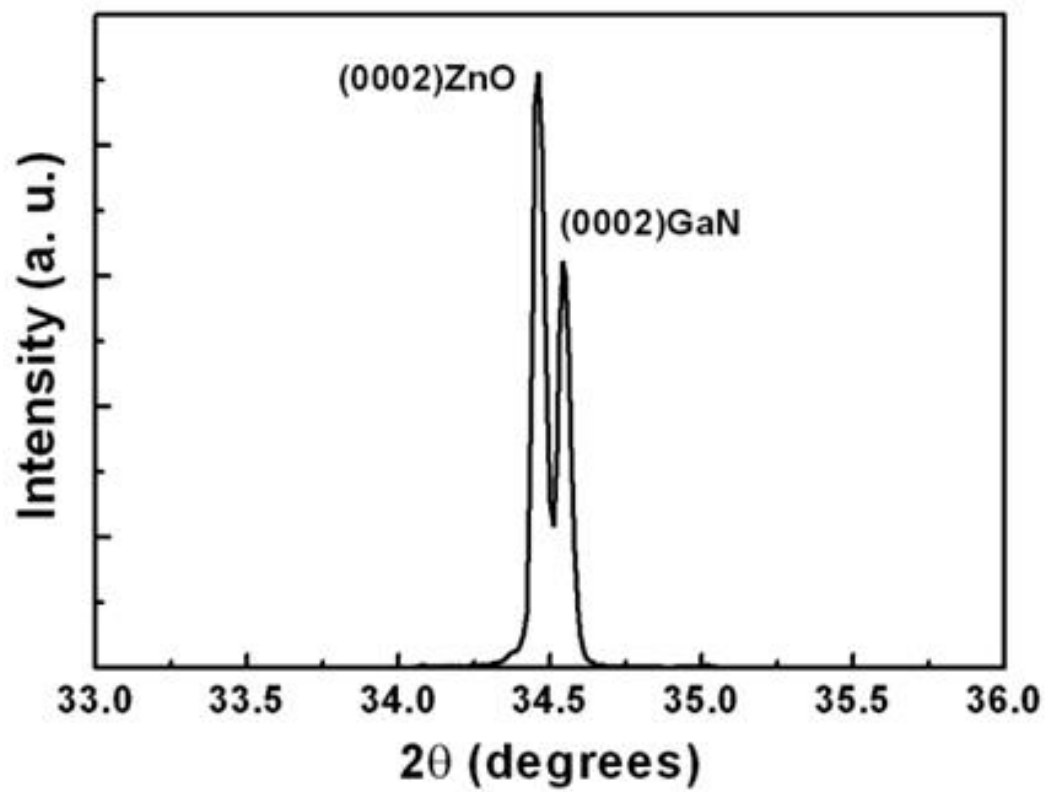


Figure 3. 5: XRD two theta scan spectrum of GaN template and ZnO/GaN heterostructure

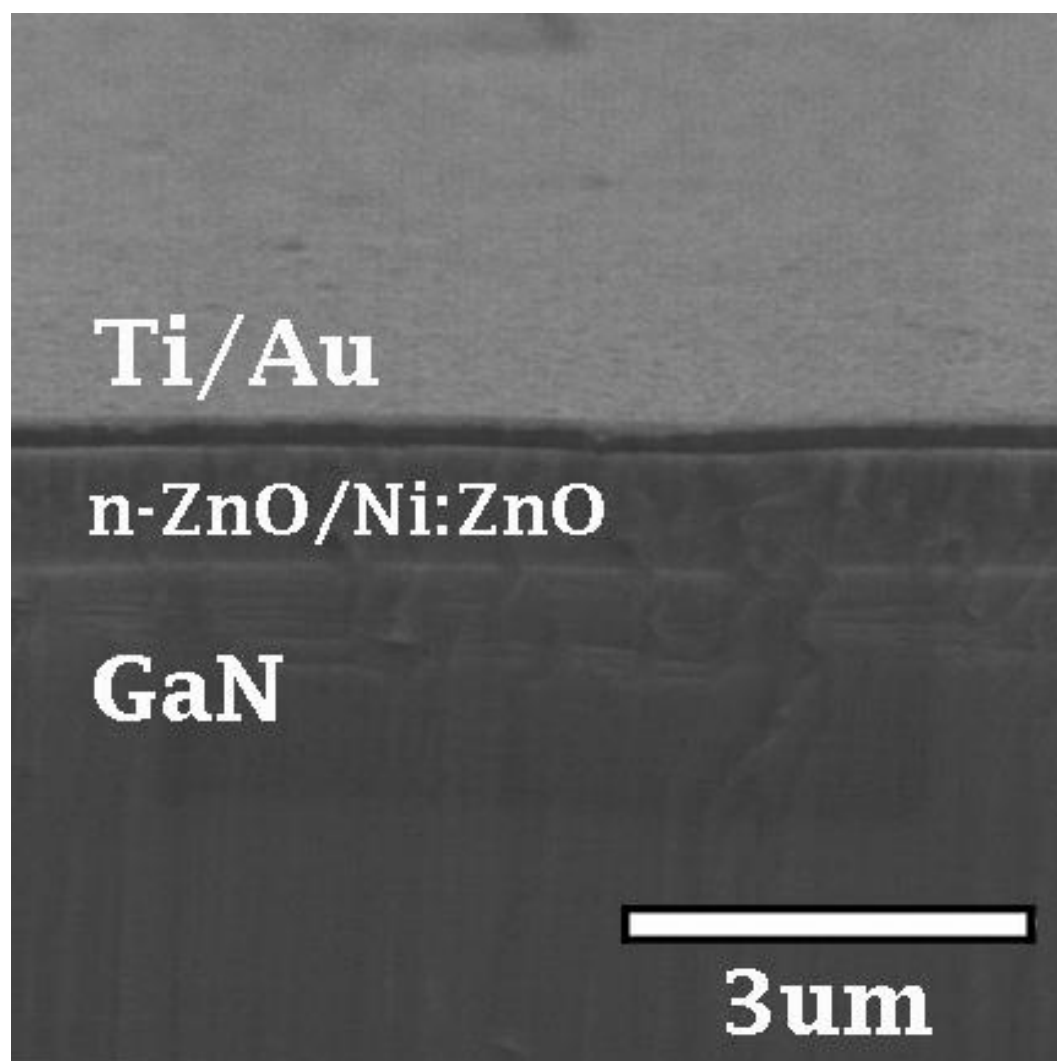


Figure 3. 6: FESEM image of piezoelectric ZnO layer on top of GaN template.

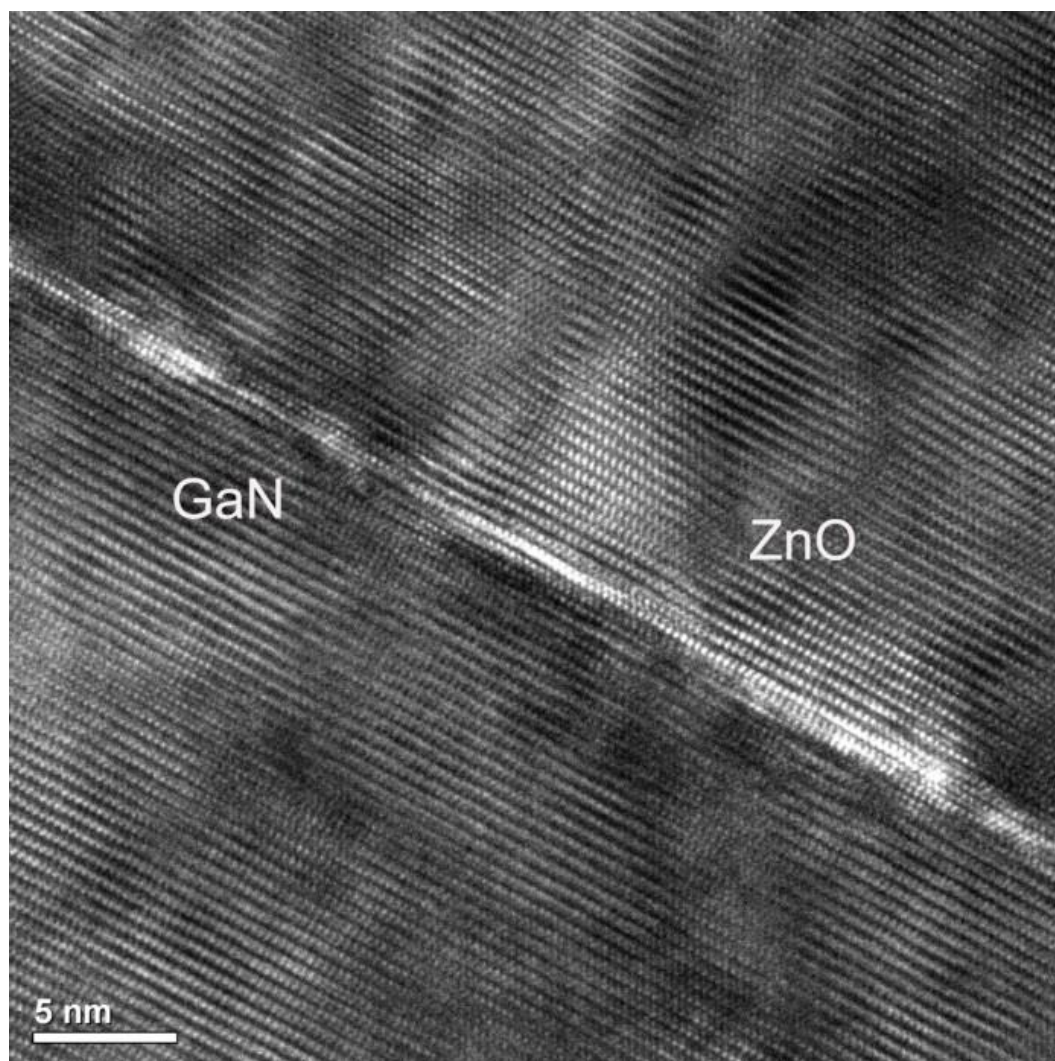


Figure 3. 7: A ZnO/GaN heterostructure cross-sectional TEM image.

3.3 SAW Characteristics in ZnO/GaN-based Multilayer Structure

The SAW dispersion properties of the ZnO/GaN/c-Al₂O₃ system were investigated using the transfer matrix method. It has been shown the high frequency and low-loss SAW devices can be achieved by depositing piezoelectric thin films on high acoustic velocity substrates.[10] Zinc oxide films on high-velocity, low loss substrates such as sapphire, have high coupling factor, higher-order generalized SAW modes. SAW devices on GaN/c-Al₂O₃ can provide a high velocity of 5803 m/s, relatively low insertion loss of -7.7 dB.[95] By combining ZnO and GaN; we can take advantage of the inherent advantages of higher order wave modes with large coupling coefficient and high acoustic velocity provided by both materials. Studies show that compared to single layer Al_xGa_{1-x}N, the ZnO/Al_xGa_{1-x}N multilayer structures can be used to realize high frequency and low loss SAW devices and broad bandwidth SAW devices.[10] As the ZnO/GaN SAW device uses a layered material system, the acoustic velocity will be dispersive, and multiple wave modes which satisfy the boundary conditions will be excited. It is advantageous to use the higher order wave mode with large electromechanical coupling coefficient to attain a high frequency of operation, which is an advantage provided by ZnO/GaN structures. It has dispersive velocity characteristics, as ZnO has lower SAW velocities compared to GaN and sapphire.

For the analysis presented in this section, the effective coupling is defined with respect to the open surface (v_{oc}) and short surface (v_{sc}) velocities. Usually, a SAW device is designed to have a maximum coupling at the operating frequency. For the desired frequency, the film thickness is derived from the hf product at which maximum coupling occurs. The phase velocity and is determined from their respective velocity vs. hf curves.

It is common practice to plot the velocity and coupling coefficient curves versus the product of film thickness and frequency (hf), in which way the velocity and coupling coefficient values can be derived for any given film thickness (h). The theoretical Generalized SAW wave dispersion curves were simulated in Figure 3.8 using Adler's transfer matrix method. The simulation results for the generalized SAW modes (solid lines) show four different modes: one base mode, and three high order wave mode (HOWM). A SAW mode and its various orders are determined by the Eigenfunctions of the wave equation taking into consideration of the geometry of the device as spatial boundary conditions, as well as the material properties of ZnO/GaN to form the permittivity tensor. The resulting Eigenfunctions represent the supported SAW waves and fall within a range of frequencies allowed by both the acoustic velocities of the materials and the boundary conditions of the device. The mode that sits within the lowest dispersion curve is the base mode, and the other modes that fit the next tier of dispersion curves are the higher order modes.

To determine the SAW mode for ZnO/GaN SAW device, we fabricated multiple devices with a various piezoelectric layer thickness (h) and different IDT period (P), which related to the SAW frequency (f). The layer thickness (h) stands for the total thickness of Ni:ZnO (0.4, 0.8, and 1.5 μm) and GaN (4 μm). Moreover, the IDT patterns with different periods ($P=5\text{ }\mu\text{m}$, 6 μm , 7 μm , 8 μm , 9 μm , 11 μm , and 12 μm) are selectively fabrication of h values. Figure 3.8 shows the simulation results for the generalized SAW modes (solid lines) agree well with the measured data from the fabricated devices (various symbols represent multiple devices with the specific h and P value), confirming the four-mode SAW operation. The 3rd HOWM possess high wave velocity ($\sim 5500\text{m/s}$) at frequency thickness

product also at ~ 5500 m/s. It also shows that the device with total thickness $h=4.8 \mu\text{m}$ ($0.8 \mu\text{m}$ Ni-ZnO and $4.0 \mu\text{m}$ GaN) and IDT period $P=6 \mu\text{m}$ offers the highest acoustic phase velocity.

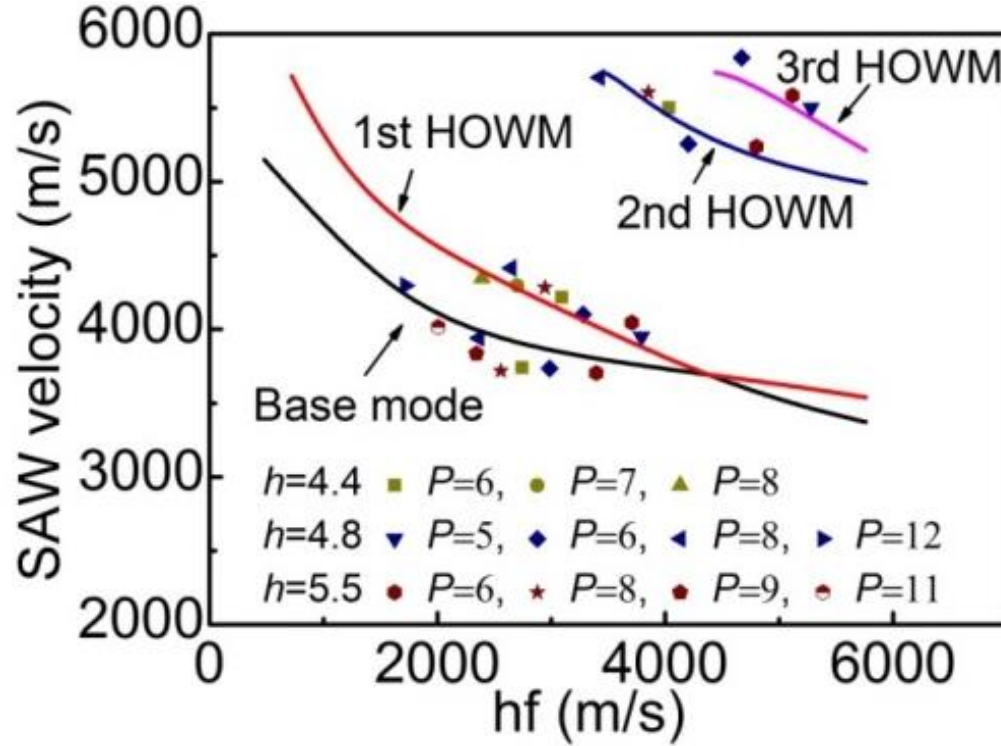


Figure 3. 8: The curves represent the SAW dispersion simulation results using the transmission line model. The symbols represent the testing results from the devices with the specific total thickness of Ni:ZnO and GaN (h) and the IDT period (P) in μm .

The K^2 is simulated as shown in Figure 3.9. The most interesting mode to consider from the dispersion characteristics is the 3rd order generalized SAW mode (3rd HOWM). Besides a high SAW velocity thus high operating frequency as shown, it also possesses a large electromechanical coupling coefficient K^2 ($\sim 4.5\%$) in a wide thickness-frequency product (hf) window (3,000 m/s to 5,500 m/s). This indicates the optimal layer structure with the IDT period of $6 \mu\text{m}$ provides both of high velocity and a large electromechanical

coupling coefficient in a broad frequency bandwidth, benefiting design of high frequency and low loss SAW devices.

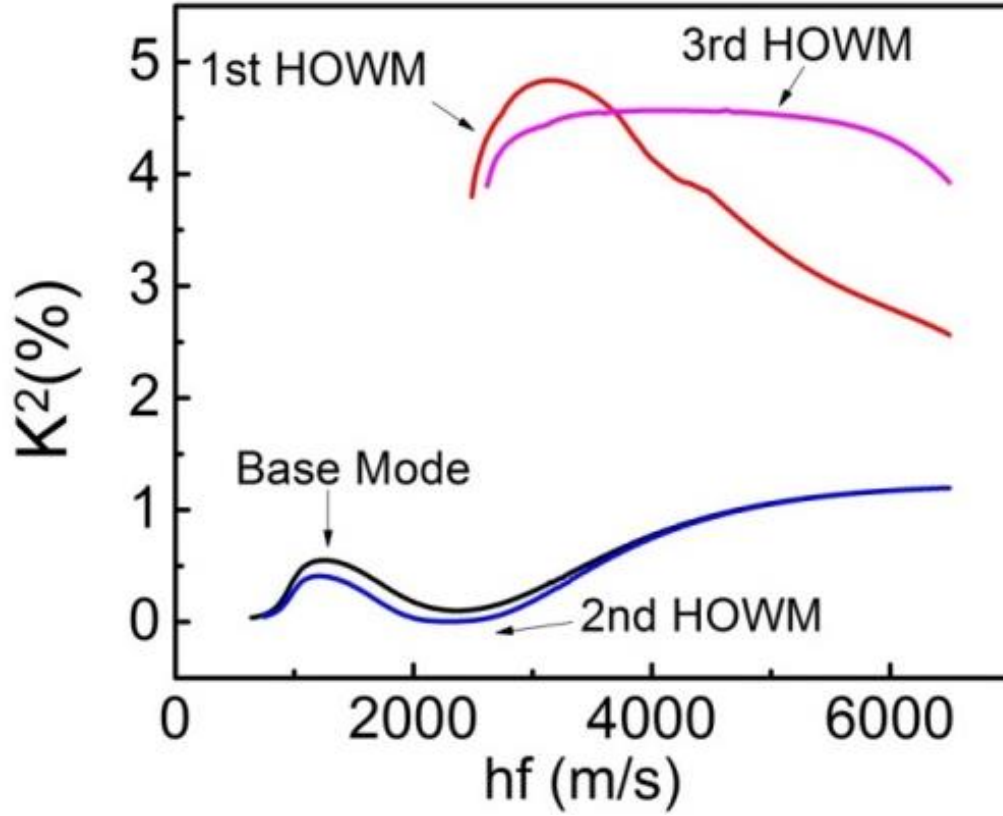


Figure 3. 9: Simulation results of electromechanical coefficient K^2 of the Ni:ZnO/GaN SAW devices.

3.4 Frequency Tunability

The optimal device structure has been designed as: piezoelectric layer thickness is $0.8 \mu\text{m}$ ($h=4.8 \mu\text{m}$) and the IDT period (P) is $6 \mu\text{m}$, which provides both of high velocity and large electromechanical coupling coefficient in a broad frequency bandwidth, benefiting design of high frequency and low loss SAW devices. Base on this device structure, we first achieve four-mode SAW response by measuring the transmission parameter S_{21} . Then we test Ni:ZnO/n-ZnO/GaN tunable SAW device with a different n-

ZnO layer thickness ($t=50$ nm and 120 nm). The thickness dependency of frequency tunability and insertion loss has been shown. Based on these results, we further discuss the tuning mechanism of Ni:ZnO/n-ZnO/GaN tunable SAW device through gate depletion.

A representative acoustic spectral response exhibits multiple generalized surface acoustic waves with a base mode and three higher-order wave modes (HOWM) as shown in Figure 3.10. Four different characteristic frequencies are observed at 600MHz, 670MHz, 770MHz, and 980MHz for this device.

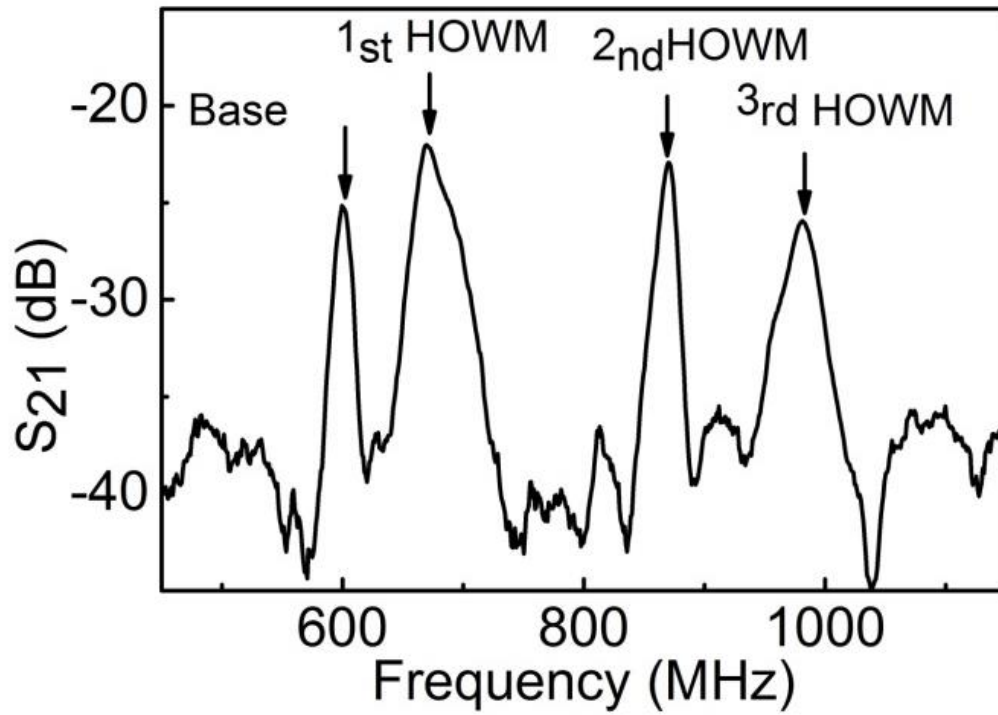


Figure 3. 10: A representative SAW response in the Ni-ZnO/GaN structure shows the base wave mode and three higher order modes

Based on the optimization of piezoelectric Ni-ZnO film thickness ($h=4.8$ μm) and IDT configuration ($P=6$ μm), the tunable SAW devices with various n -ZnO thicknesses are fabricated. The inset of Figure 3.11 shows a representative frequency response from one tunable SAW phase shifter under zero bias. The S_{21} spectrum shows the 3rd order

generalized wave mode having the center frequency f at 1.245 GHz. It should be pointed out that in the current device design, the minimum feature size is 1.5 μm ($P=6\ \mu\text{m}$). By adapting the device design with smaller feature size and using the sub-micron or nano-scale lithography technology, the multi-GHz operation can be achieved.

The phase shift corresponding to the 3rd HOMW of the devices with various $n\text{-ZnO}$ thicknesses are measured under different dc bias voltages. The normalized frequency shifts ($\Delta f/f$) and the acoustic phase velocity change ($\Delta v/v$) are computed using

$$\frac{\Delta v}{v} = \frac{\Delta f}{f} = \frac{\lambda}{L_{\text{delay}}} \frac{\Delta \phi}{360^\circ}, \quad (3.1)$$

where v is the acoustic phase velocity, f is the SAW center frequency, $\Delta \phi$ is the bias induced SAW phase shift, λ is the SAW wavelength, which equals to the period of IDT (P), L_{delay} is the delay line defined by edge-to-edge distance between IDTs. Figure 3.11 presents the phase velocity tunability of SAW devices with the thinnest (50 nm) and thickest (120 nm) $n\text{-ZnO}$ layer as a function of external bias, whereas the Ni-ZnO piezoelectric layer thickness of the devices is fixed at 0.8 μm . The velocity change of the SAW device increases continuously with increasing negative gate bias voltage. The maximum velocity changes $\Delta v/v$ are 0.9% and 0.72% at -25 V for device with 50 nm and 120 nm $n\text{-ZnO}$ respectively, while the intermediate thicknesses (70 nm and 100 nm) exhibit peak tunability values (not shown here) between these two extreme values.

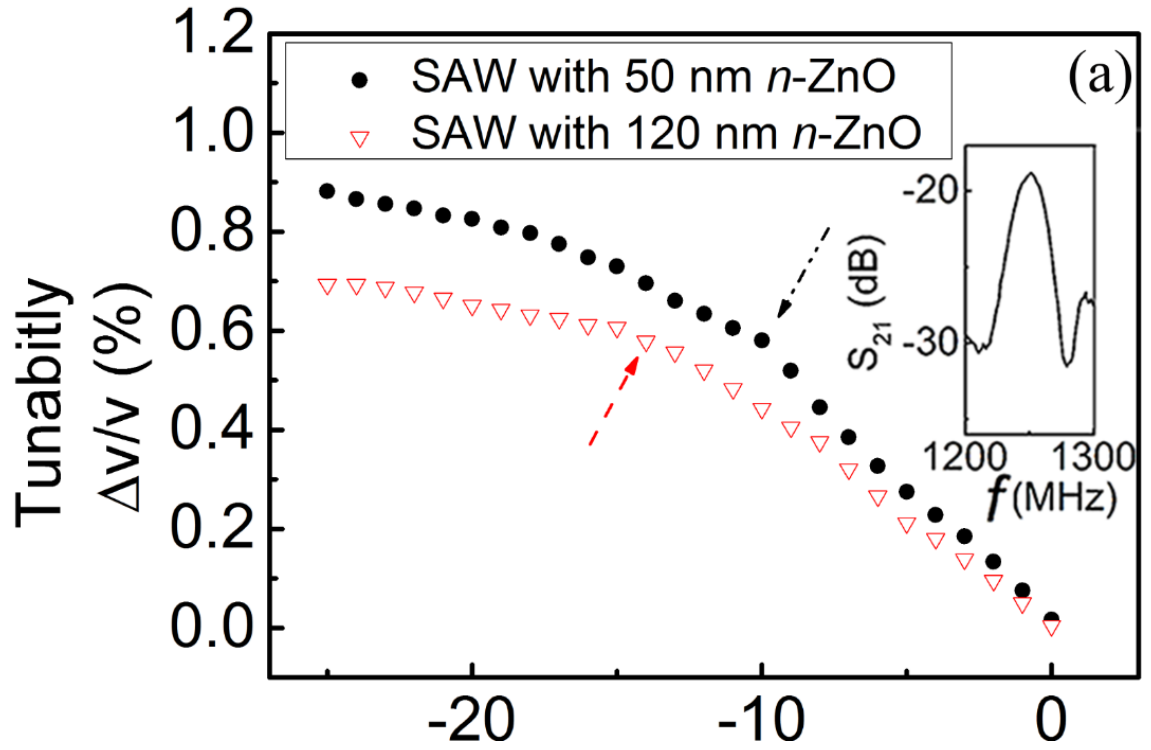


Figure 3. 11: Normalized phase velocity change vs. bias voltage for the tunable SAW devices with various semiconductor n -ZnO thicknesses d_{ZnO} (50 nm and 120 nm). The inset is the measured SAW response, showing the center frequency of 1.245 GHz. The arrows point the bias voltages which result in full depletion of 50 nm and 120 nm n -ZnO layer, respectively.

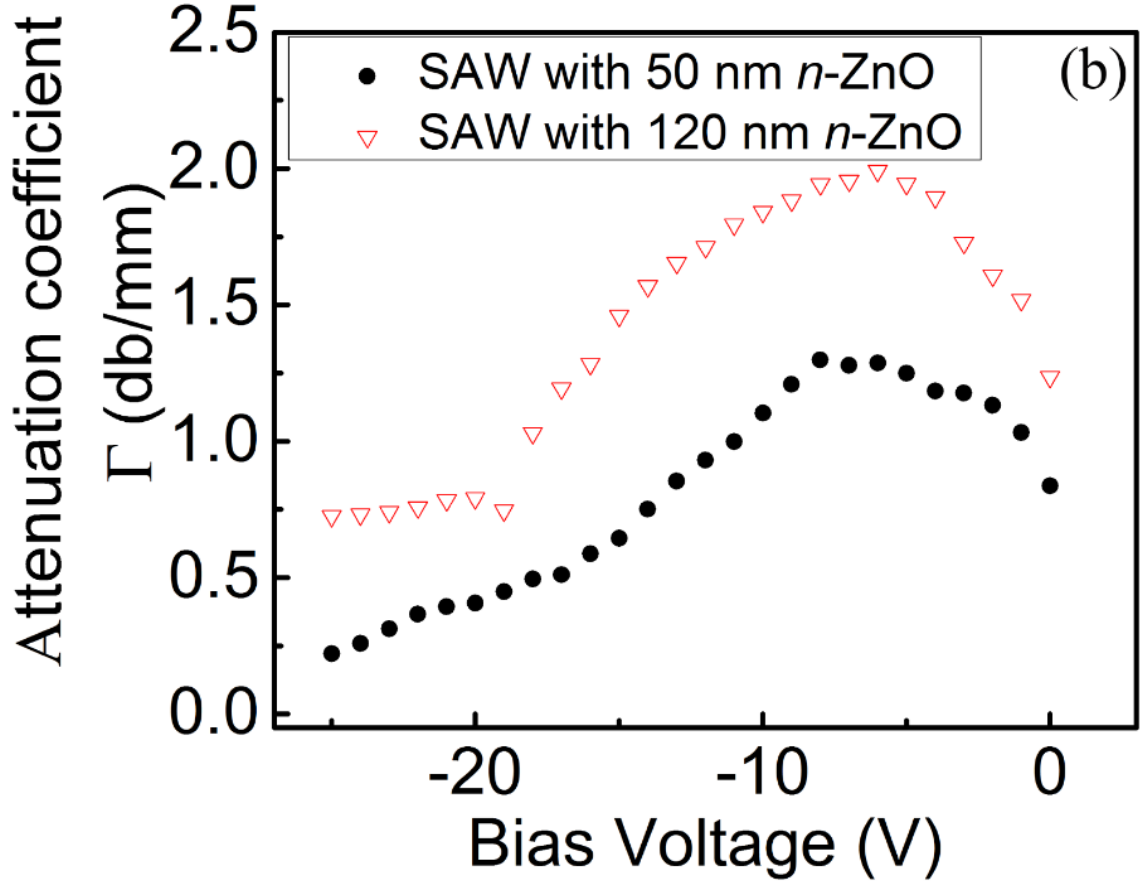


Figure 3. 12: SAW attenuation as a function of bias voltage for devices with 50 nm and 120 nm semiconducting n -ZnO layer, respectively.

The measured SAW attenuations of the two devices are presented in Figure 3.12. The maximum attenuations for the devices with 50 nm and 120 nm n -ZnO are 1.3 dB/mm and 2.0 dB/mm, respectively. The maximum attenuation of the later device is larger due to the thicker semiconductor layer. According to Eqn. (2.16) and Eqn. (2.23), the maximum attenuation is determined by $\Gamma_{\max}=2k(v_{oc}-v_{sc})/v_{oc}$. For different semiconductor layer thicknesses $d_{n\text{-ZnO}}$, v_{oc} keeps as constant while v_{sc} is inversely related to $d_{n\text{-ZnO}}$ due to the ohmic loss induced by mobile charges. Thus, thicker n -ZnO layer results in a larger SAW attenuation Γ_{\max} .

In a piezoelectric/semiconducting dual layer system, the electric field associated with the SAW propagation along a piezoelectric layer would couple with the mobile carriers existing in the semiconducting layer with a sheet conductivity σ_d , causing SAW attenuation and velocity change. As the semiconductor thickness in the dual-layer structure is much smaller than the acoustic wavelength, the velocity change ratio $\Delta v/v_{oc}$ and the attenuation Γ can be written as[6]

$$\frac{\Delta v}{v_{oc}} = \frac{v - v_{sc}}{v_{oc}} = \frac{K_{eff}^2}{2} \frac{1}{1 + (\sigma_d / \sigma_M)^2}, \quad (3.2)$$

$$\Gamma = k \frac{K_{eff}^2}{2} \frac{(\sigma_d / \sigma_M)}{1 + (\sigma_d / \sigma_M)^2}, \quad (3.3)$$

where v_{oc} is the acoustic velocity when the semiconductor layer is fully depleted, which is independent of the semiconductor layer thickness d_{n-ZnO} , v_{sc} is the acoustic velocities when the semiconductor layer is undepleted, K_{eff}^2 denotes the effective electromechanical coupling coefficient of the device, given by $2(v_{oc} - v_{sc})/v_{oc}$, k is the SAW wave vector, σ_M is the relaxation conductivity at which the maximum attenuation occurs, given by $\sigma_M = v_{oc}(\epsilon_p + \epsilon_s)$, ϵ_p and ϵ_s are the dielectric constants of the piezoelectric and semiconducting layer, respectively.

To demonstrate the charge modulation by gate voltage, Fig. 3.13 shows a schematic diagram of the conduction band energy levels of the device under a negative gate bias, where Ni-ZnO is considered as a dielectric layer. From left to right, region A represents the depleted n -ZnO near Ni-ZnO; region B represents the undepleted n -ZnO; and region C represents the electron accumulation layer near the n -ZnO/GaN interface.

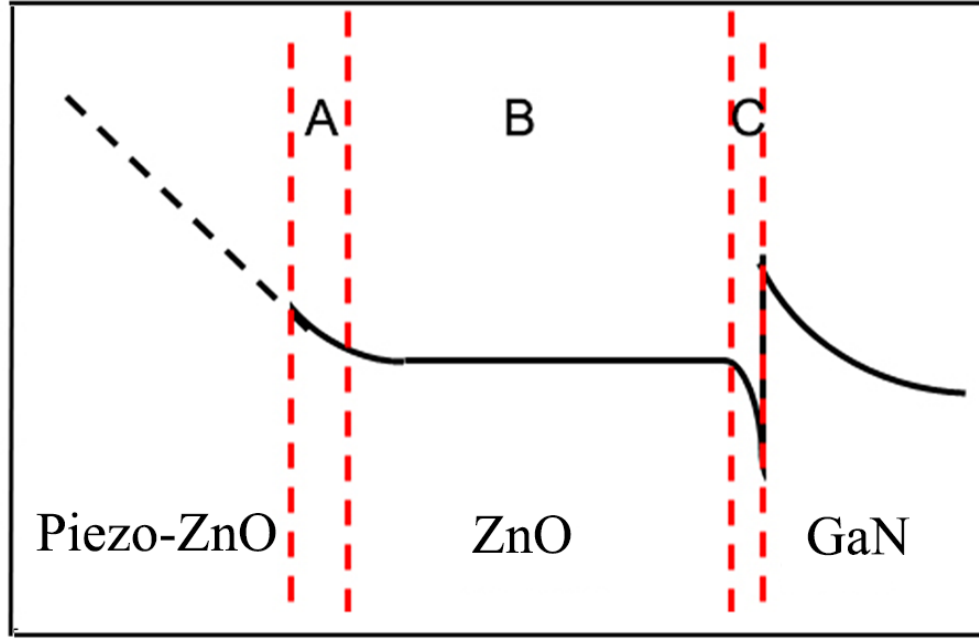


Figure 3. 13: A schematic drawing of conduction band energy levels in the Ni-ZnO/n-ZnO/GaN structure under the negative bias voltage.

In our structure, the sheet conductivity σ_d in can be decomposed into:

$$\sigma_d = q\mu_{accu}n_{accu} + q\mu_{free}n_{free}, \quad (3.4)$$

where n_{accu} and σ_{accu} is respectively the sheet density and the mobility of electrons accumulated near the n -ZnO/GaN interface (region C in Fig.3.13), while n_{free} and σ_{free} is respectively the sheet density and mobility of electrons in the bulk n -ZnO layer (region B in Fig.3.13). Electrons accumulated in region C is induced by spontaneous (n_{sp}) and piezoelectric (n_{pz}) charges at the n -ZnO/GaN interface and the ionized donors ($N_{D,GaN}$) in the depletion region of GaN, near zero bias, it is given by:

$$n_{accu}(V_g \approx 0) = n_{sp} + n_{ps} + \sqrt{2\varepsilon_{GaN} N_{D,GaN} (\Delta E_c - E_n - E_{2D})} / q, \quad (3.5)$$

where ε_{GaN} is the dielectric constant of GaN, ΔE_c is the conduction band discontinuity, E_n is the conduction band energy with respect to the Fermi level in the GaN neutral region, E_{2D} is the heterojunction confinement energy at the n -ZnO/GaN heterointerface. It should be noted that Eqn. (3.5) is independent of the thickness of the n -ZnO layer ($d_{n\text{-ZnO}}$). On the other hand, the bulk free electron density near zero bias is almost proportional to the thickness of the n -ZnO layer. Under abrupt depletion approximation and at a small negative bias, the free electron sheet density n_{free} as a function of negative gate voltage V_g can be written as:

$$n_{\text{free}}(V_g) \approx N_{D,n\text{-ZnO}}(d_{n\text{-ZnO}} - d_{2d}) - \frac{(\phi_B / q - V_g)\varepsilon_{\text{ZnO}}}{qd_{\text{Ni-ZnO}}} \left(1 - \frac{\varepsilon_{\text{ZnO}}}{2qN_{D,n\text{-ZnO}}} \frac{(\phi_B / q - V_g)}{d_{\text{Ni-ZnO}}^2}\right), \quad (3.6)$$

where $N_{D,\text{ZnO}}$ is the ionized donor concentration in the n -ZnO region, $d_{n\text{-ZnO}}$, d_{2d} , and $d_{\text{Ni-ZnO}}$ are the thicknesses of the n -ZnO layer, the heterojunction depletion region, and the piezoelectric Ni-ZnO layer respectively, ε_{ZnO} is the dielectric constant of ZnO, and ϕ_B is the barrier height.

Under a small negative bias, the free charges are depleted first from the Ni-ZnO/ n -ZnO interface. In this low negative bias region, the SAW velocity keeps increasing while the free electron sheet density decreases, until region B of the n -ZnO layer is fully depleted at the voltage indicated by the position of arrows in Figure 3.11. The 0.8 μm -thick Ni-ZnO film acts as a gate dielectric layer during depletion. A larger bias is needed to fully deplete the free electrons in a 120 nm n -ZnO film than in the 50nm n -ZnO (see Eqn. (3.4)). However, the slope of $n_{\text{free}}(V_g)$ is independent of the thickness of the n -ZnO layer. In the high negative bias region, when the depletion depth exceeds region B, the further increase in SAW phase velocity is caused by the continuous depletion of electron density in the

electron accumulated region (region C in Figure 3.13). Modeling further shows that after free electrons n_{free} is fully depleted the slope of n_{accu} (V_g) at large bias is almost the same as the slope of n_{free} (V_g) at low bias. However, the increase of SAW velocity (slope) in this large bias region is slower than that of free charge depletion in the low negative bias region as illustrated in Figure 3.11. This suggests a lower mobility of the electrons in region C than that in region B in Figure 3.13. We attribute it to the interface traps and electron scattering in the ZnO/GaN heterointerface. Further, detailed calculation shows more evidence of a much lower mobility for the accumulated electrons in region C. The relaxation conductivity (σ_M) at which the maximum attenuation occurs is about 1 $\mu\text{A/V}$ (using $v_0=6,200$ m/s obtained from the device). For a structure with an n -ZnO layer thickness of 50 nm, an electron concentration of 10^{17} cm^{-3} , and an electron mobility of 40 $\text{cm}^2/\text{V-s}$, the bulk free electron's contribution (second term in Eqn. (3.4)) to σ_d is about 3.2 $\mu\text{A/V}$. The maximum attenuation ($\sigma_d=\sigma_M$) occurs at $V_g=-4.5$ V (Eqn. (3.3)). However, this is only true when the mobility of the electron in region C in Figure 3.13 (σ_{accu}) is less than 1 $\text{cm}^2/\text{V-s}$. For example, if $\sigma_{accu}=2 \text{ cm}^2/\text{V-s}$, its contribution to the σ_d is also about 3.2 $\mu\text{A/V}$. With a total $\sigma_d=6.4 \mu\text{A/V}$ at zero bias, the maximum attenuation ($\sigma_d=\sigma_M$) occurs at $V_g=-13$ V, which clearly is not the case for our structure. In contrast to free electrons in region B, the slope of n_{accu} (V_g) depends on the thickness of the n -ZnO layer. This could explain why the device with 50 nm n -ZnO film yields the larger maximum SAW velocity change $\Delta v/v_{oc}$ at a gate bias of -25 V, compared to the device with 120 nm n -ZnO.

3.5 The Effect of Buried IDT Design

The voltage-controlled SAW velocity tuning in the piezoelectric-semiconducting dual layer structure through acoustoelectric interaction has been proposed as an effective solution.[6] The interaction between the SAW generated a longitudinal electric field along the piezoelectric layer and the free carriers in the semiconducting layer will result in acoustic wave attenuation and velocity change, due to ohmic loss and piezoelectric stiffening. The piezoelectric ZnO/GaN layer structure provides high-frequency SAW response (1.245GHz), and the interaction between the SAW generated an electric field in the piezoelectric layer and the free carriers in the semiconducting layer results in 0.9% frequency change, equivalent to a frequency change of 11.2 MHz at -25 V bias. Although this device design improves the frequency tunability and reduces operation voltage, it still contains some non-tuning related loss mechanisms which increase overall power consumption. For instance, the n-ZnO layer directly under IDT region does not contribute to SAW tuning. Adversely, this layer provides an electron leak path, thus reduce the energy transfer efficiency between electric power and mechanical SAW energy. To increase the energy efficiency of voltage tunable SAW device and improve the electromechanical coupling coefficient K^2 , a better device structure and process design is needed. In this section, we report a new design of the voltage controlled SAW phase shifter based on the buried IDTs configuration compared with previous exposed IDT. The buried IDTs are sandwiched by GaN and piezoelectric NZO layer, instead of being exposed to air, to improve the acoustic coupling. The n-ZnO layer under IDT region is removed to reduce the energy loss during SAW generation. The tunability and attenuation of two devices are compared, showing a superior performance of buried IDT configuration.

The schematic drawings of the tunable SAW devices with exposed and buried IDT configurations are presented in Figure 3.14 (a) and (b), respectively. The device layer structures of both configurations follow the same order from top to bottom: Au/Ti/NZO/n-ZnO/GaN/Al₂O₃. The core functional structure of the device is based on a piezoelectric NZO on the semiconductor ZnO/GaN heterostructure for frequency tuning. Zinc oxide (ZnO) and gallium nitride (GaN) are both wide band gap semiconductors and belong to the same wurtzite crystal structure group with close lattice parameters. High-quality, high resistivity piezoelectric films can be obtained using NZO target by RF sputtering.[80] In general, in a multilayer material piezoelectric system where a low acoustic velocity thin film is stacked on a high-velocity substrate, high order wave mode will be activated due to the velocity dispersion in the layer structure. The generation of multiple modes due to the “slow” overlayer induced acoustic confinement is usually described as “slow on fast” phenomena.[81] ZnO possesses a higher electromechanical coupling coefficient[67] over GaN[96] as shown in Table 3.1. However, the acoustic velocity of ZnO (3,300 m/s) is small than that of GaN (6,000 m/s). The integration of a piezoelectric ZnO with GaN offers higher-order overtone SAW modes with high acoustic velocity and thus high frequency as well as a high electromechanical coupling coefficient. The thickness of NZO and the IDT period P are optimized to be 0.8 μ m and 6 μ m to achieve the high order mode; therefore, the high-frequency SAW operation.[97]

Table 3. 1 SAW velocity and piezo coupling coefficient of ZnO and GaN[67], [96]

Symbol		ZnO	GaN
SAW velocity [km/s]	v	3.3	6
Piezo coupling coefficient	k^2	11%	4.3%

X-ray diffraction (XRD) analysis was carried to characterize the crystalline property of NZO layer, using a PANalytical X'Pert3 Powder System with Cu K α radiation ($\lambda = 0.1540562$ nm) as shown in Figure 3.15. The (0001) ZnO and (0001) GaN peaks are clearly defined, showing the preferred orientation of NZO along the c-axis. Figure 3.16 shows the field emission scanning electron microscopy (FE-SEM, Hitachi S-800) image of overall Au (100nm)/Ti (50nm)/NZO (0.8 μ m)/n-ZnO (50nm)/GaN (4 μ m)/Al $_2$ O $_3$ structure. The inset of Figure 3.16 shows the high magnification transmission electron microscopy (TEM) image of n-ZnO/GaN interface using JEOL 2100F transmission electron microscope that indicates the excellent crystal quality and the sharp and flat interface, benefiting low loss and high coupling SAW performances.

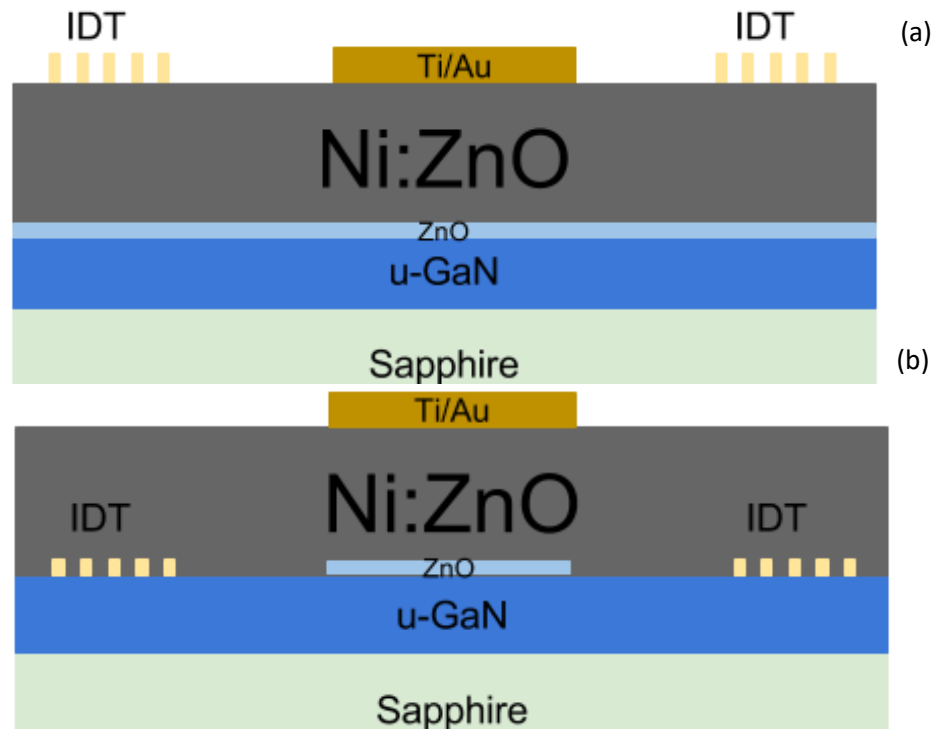


Figure 3. 14 The schematic cross-section of the tunable SAW device with (a) exposed and (b) buried IDT configuration.

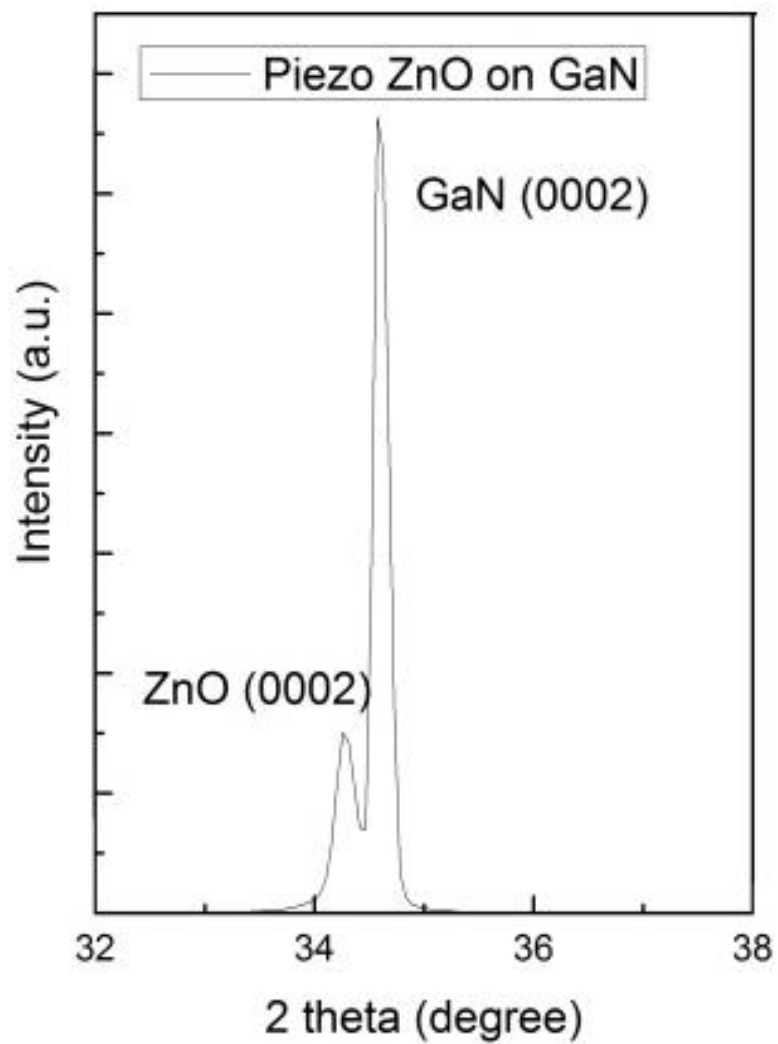


Figure 3. 15 XRD Spectrum for NZO grown on an GaN/Al₂O₃ template.

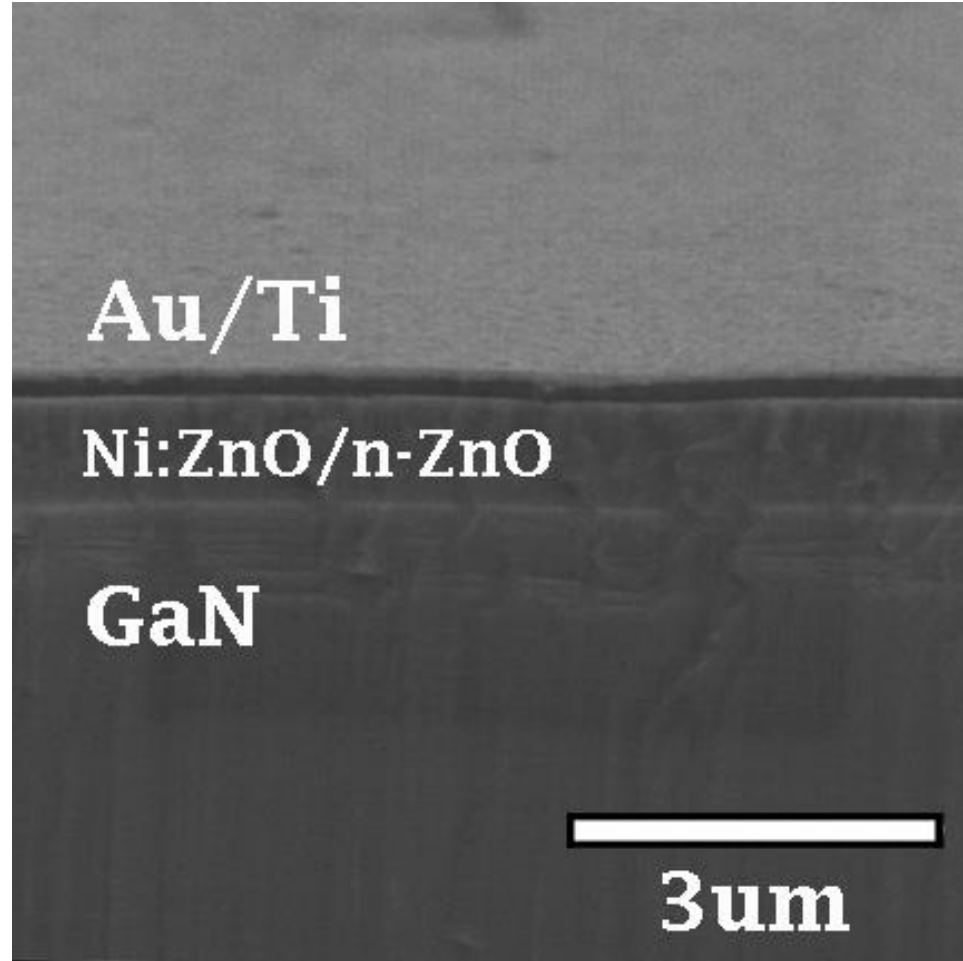


Figure 3. 16 SEM image of overall Au/Ti/NZO/n-ZnO/GaN/Al₂O₃ structure. Inset: TEM image of n-ZnO/GaN interface.

The fabrication process flow chart of the tunable SAW device with exposed and buried IDT configuration is schematically presented in Figure 3.17 (a) and (b), respectively. Both devices started with a 4- μm -thick n-type GaN ($n=6\times 10^{16} \text{ cm}^{-3}$) deposited on a c-Al₂O₃ substrate using metal-organic chemical vapor deposition (MOCVD). 50nm n-ZnO layer was deposited on GaN/Al₂O₃ template by MOCVD. An *n*-type semiconductor ZnO layer (*n*-ZnO) with a carrier concentration of 10^{17} cm^{-3} was then grown on the GaN by MOCVD at $\sim 500^\circ\text{C}$ using DEZn (diethyl zinc), O₂ (5N) and Ar (5N) as precursors, oxidizer, and a

carrier gas, respectively. For exposed IDT structure shown in Fig.3.14 (a), the Ni-doped ZnO layer (0.8 μ m) was directly deposited on n-ZnO by RF sputtering (NZO target: 5 at. % Ni). The deposition was carried out in an ambient mixture of Ar and O₂ (1:3), and the overall chamber pressure was maintained at 8×10^{-3} Torr. A Ti/Au (100nm/50nm) metallization scheme was deposited by electron beam evaporation and then patterned as the top gate using the lift-off process. Finally, the IDT electrodes were formed by deposition of Al (150 nm) followed by a selective wet etching process. For the buried IDT configuration shown in Fig. 3.15 (b), the basic process was essentially same except that the n-ZnO layer was patterned by the wet etching using diluted HCL solution (1:2000). Cr (50 nm) was deposited by E-beam and followed by IDT patterning. The NZO (0.8 μ m) was finally deposited on n-ZnO as well as on the IDTs electrodes. Figure 3.18 shows the top view of buried IDT SAW. The middle square with shiny metallic color is exposed Ti/Au metal top gate. The darker color metals are the IDT patterns buried underneath piezoelectric Ni:ZnO.

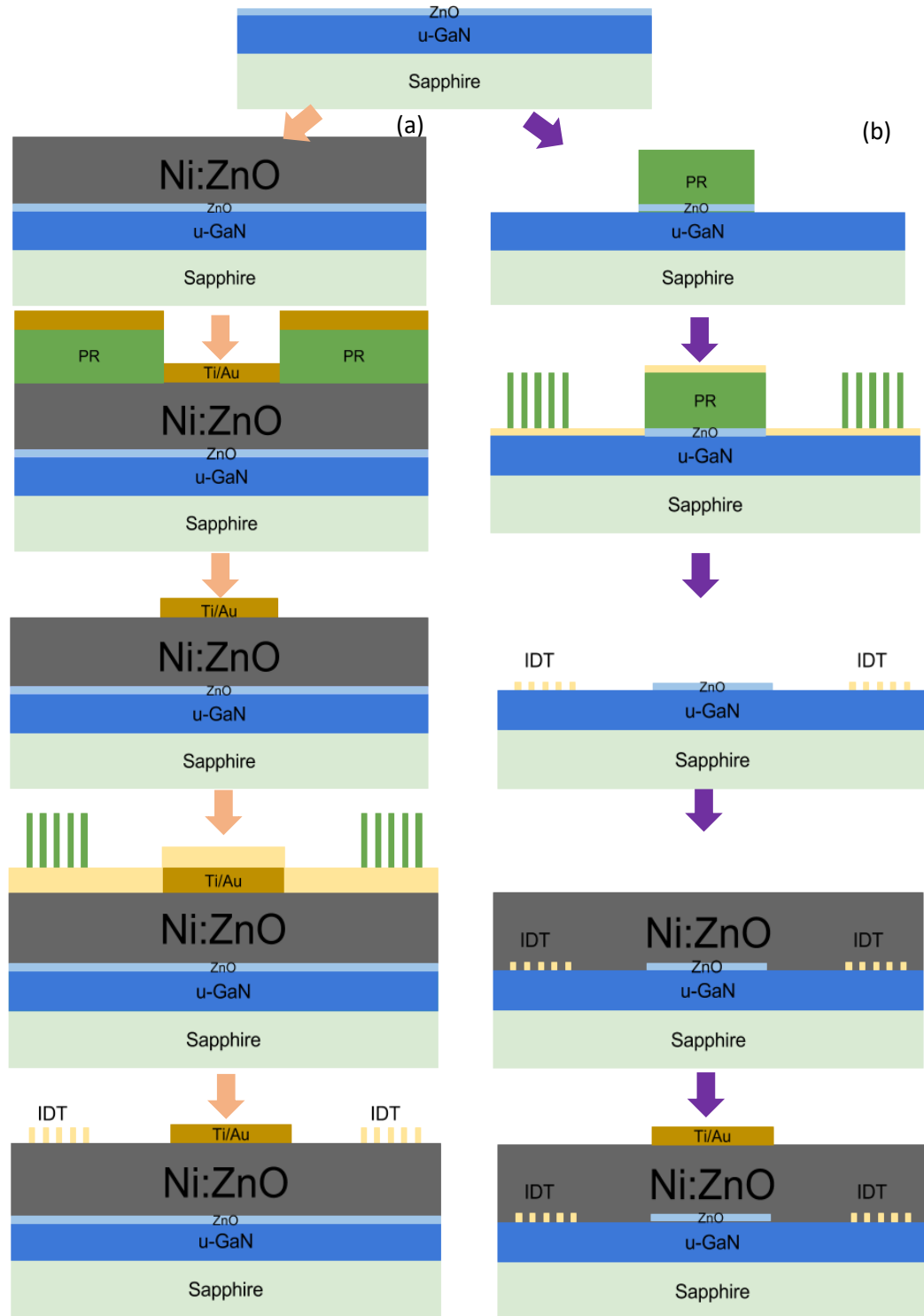


Figure 3. 17: The schematic diagram of the NZO/ZnO/GaN-based tunable SAW devices process flow chart with (a) exposed IDT, and (b) buried IDT.

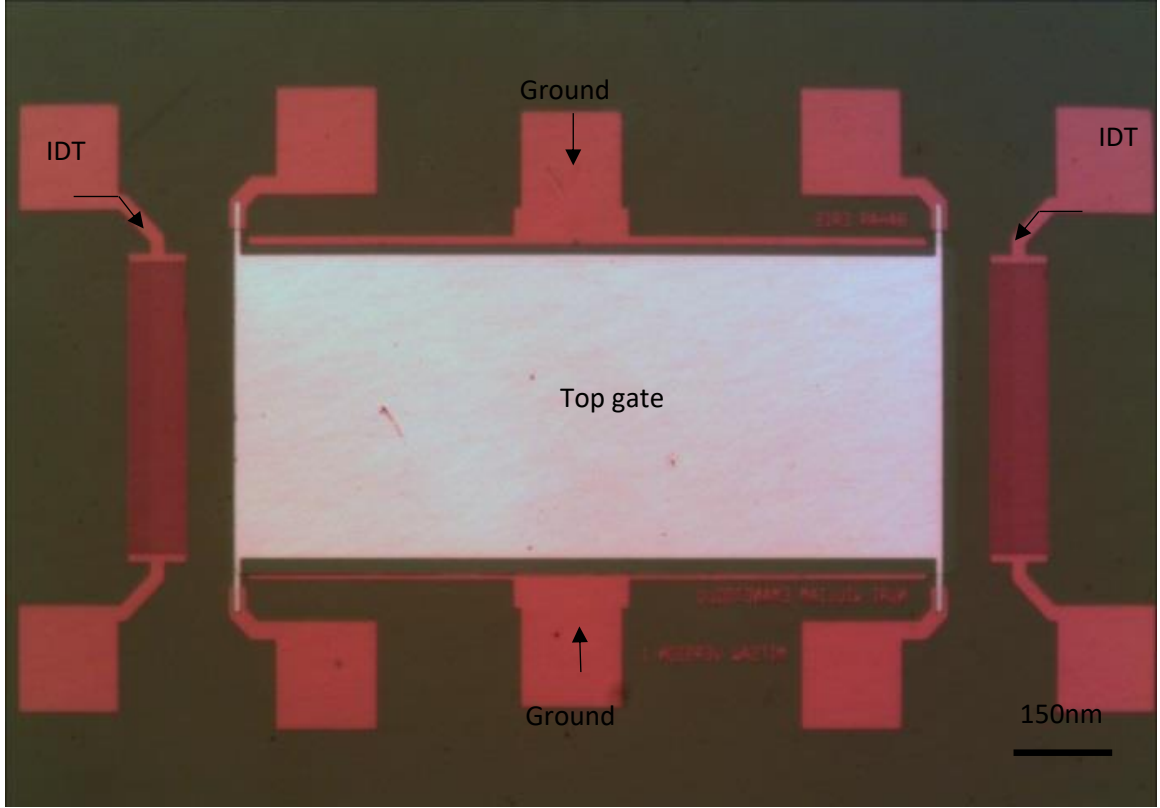


Figure 3. 18: Top view of buried IDT SAW device.

The electromechanical coupling coefficient K^2 of a SAW device pertains to the magnitude of the signal propagation loss accrued from input to output, which directly affects the insertion loss and effective bandwidth of a SAW device. Therefore, it is important to correlate the reduction of the insertion loss with the effective electromechanical coupling coefficient K^2 of the SAW devices with buried IDT configuration. The simulation using the multilayer transmission line model (TLM) is conducted in the ZnO/GaN/Al₂O₃ system for both the exposed IDT and buried IDT configurations. The GaN and ZnO thickness is set to be 4 μm and 0.8 μm , respectively. The values of K^2 of SAWs are calculated using:

$$k^2 = 2 \frac{v_{oc} - v_{sc}}{v_{oc}} \quad (3.7)$$

where v_{oc} is the acoustic velocity of the propagating SAW under free surface (when the semiconductor layer is fully depleted), and v_{sc} is the acoustic velocity of the propagating SAW at electrically shorted conditions (when the semiconductor layer is undepleted). The v_{oc} and v_{sc} were calculated for a range of frequencies using the corresponding free surface and electrically shorted boundary conditions to obtain two dispersion functions $v_{oc}(hf)$ and $v_{sc}(hf)$, where h is the total piezo layer thickness and f is the frequency. The value of K^2 as a function of product hf is then determined from Eq. (3.7).

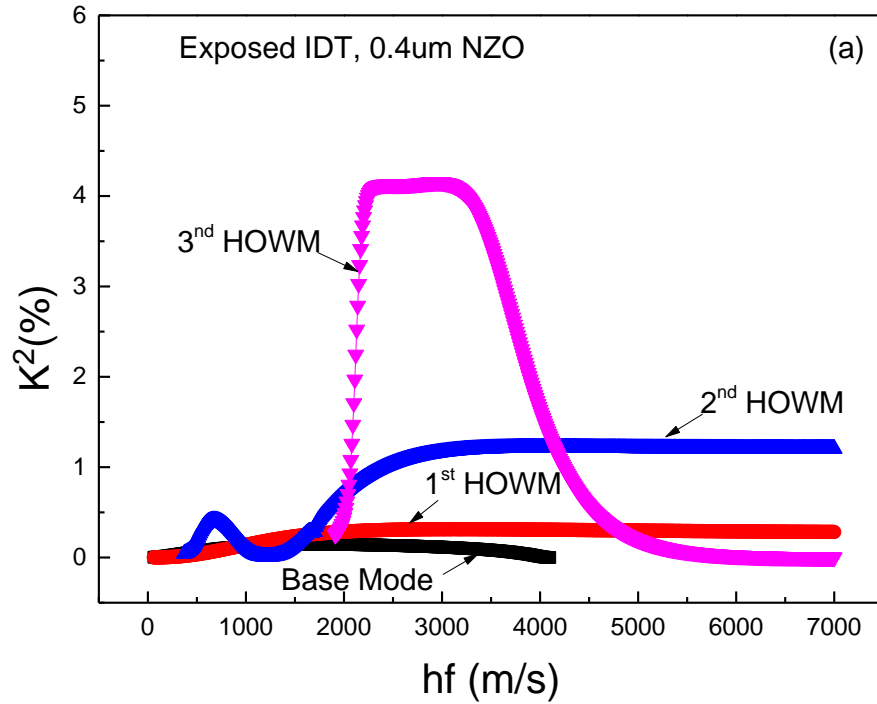


Figure 3. 19 TLM simulation result of electromechanical coefficient K^2 of the 0.4 um NZO/n-ZnO/GaN SAW devices with exposed IDT structure

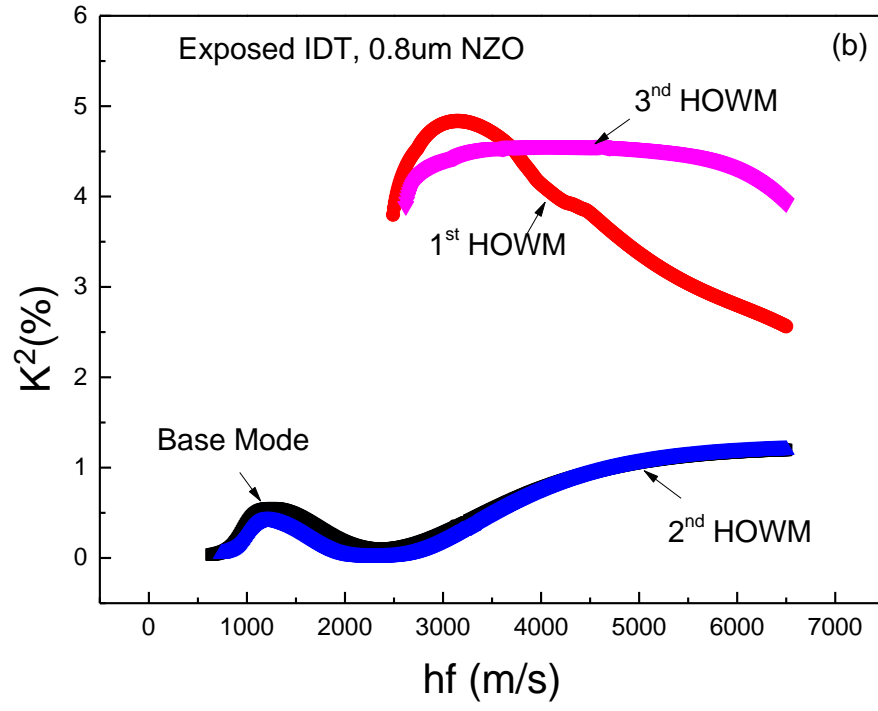


Figure 3.20 TLM simulation result of electromechanical coefficient K^2 of the 0.8 μm NZO/n-ZnO/GaN SAW devices with exposed IDT structure.

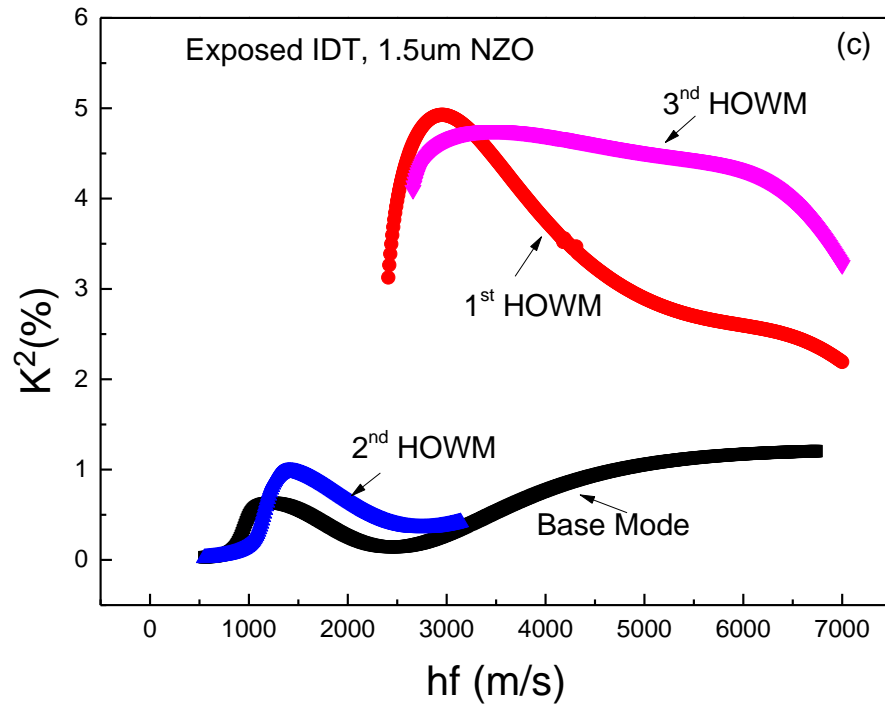


Figure 3. 21 TLM simulation result of electromechanical coefficient K^2 of the 1.5 μm NZO/n-ZnO/GaN SAW devices with exposed IDT structure.

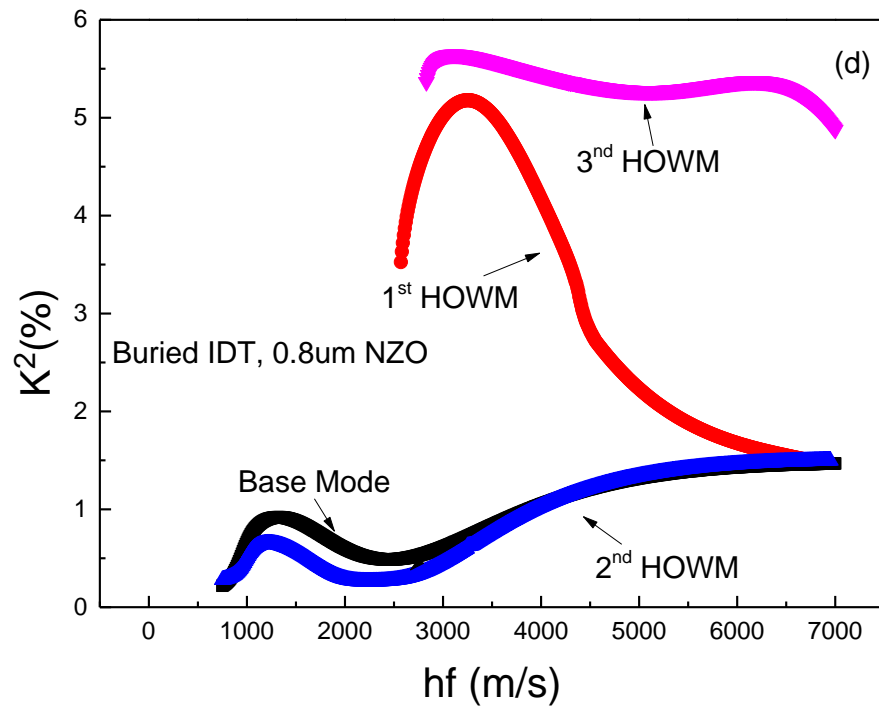


Figure 3. 22 TLM simulation result of electromechanical coefficient K^2 of the 0.8 um NZO/n-ZnO/GaN SAW devices with buried IDT structure.

Table 3. 2 Simulated frequency range for 3rd HOWM using difference IDT configurations and NZO thickness

IDT configuration	NZO layer thickness (um)	Total piezo thickness h (um)	3 rd HOWM simulated K^2	f_{\min} (MHz)	f_{\max} (MHz)
Exposed	0.4	4.4	>4%	511.4	738.6
Exposed	0.8	4.8	>4%	552.1	1337.5
Exposed	1.5	5.5	>4%	483.6	1178.2
Buried	0.8	4.8	>5%	643.2	1568.2

The NZO/n-ZnO/GaN layer structure enables multiple surface acoustic waves: a base mode and three higher-order wave modes (HOWM) [97]. TLM simulation has been carried out using different NZO layer thickness (0.4 um, 0.8um, 1.5 um) based on exposed IDT structure, as depicted in Figure 3.19-3.21. For high-frequency tunable device operation, there are two features of the K^2 vs. hf curves should be considered: the maximum K^2 value at high frequency and wide effective bandwidth. For 0.4 um NZO case, K^2 value of 4% can be only maintained within a small hf product range of (2250 m/s – 3250 m/s), corresponding to the frequency range of (511.4 MHz – 738.6 MHz). With the NZO thickness increases to 0.8 um, the K^2 is improved, and the hf bandwidth of 4% K^2 significantly enlarges to (2650 m/s – 6420 m/s), corresponding to the frequency range of (552.1 MHz – 1337.5 MHz). Further increasing of NZO thickness does improve the maximum K^2 at the lower frequency end. However, no major impact was observed on the bandwidth (2660 m/s – 6480 m/s). Adversely, due to the increased film thickness, the frequency range shifts to (483.6 MHz – 1178.2 MHz). The simulation of three different NZO layer thickness demonstrates 0.8 um is an optimized condition that provides both high-frequency operation and high K^2 .

To analyze the effect of buried IDT, K^2 of the SAW device with buried IDT and 0.8 μm NZO layer is evaluated, as shown in Figure 3.22. Benefited from the unique dispersive properties in the ZnO/GaN heterostructure, buried IDT also possesses the high order wave mode at GHz frequency with good effective coupling coefficient. Compared with Figure 3.20, overall the buried IDT structure has a higher K^2 value over exposed IDT structure. For example, the 3rd HOWM of the device with exposed IDT holds a $\sim 4\%$ K^2 value. However, the device with buried IDT presents a K^2 value of $\sim 5\%$, resulted from the improved electromechanical coupling, which is desired for SAW tuning. Moreover, the buried IDT configuration has a bandwidth occurring at a slightly higher hf range (2660 m/s – 6420 m/s) compared to the exposed IDT (2830 m/s – 6900 m/s). As summarized in Table II, the highest frequency to sustain 4% K^2 is 1.34 GHz in exposed IDT configuration. However, this value increases to 1.57 GHz for a even higher K^2 (5%).

The transmission parameter S_{21} of SAW is measured using an HP 8753D network analyzer and Cascade Microtech probes. The measured center frequency of tunable SAW with both exposed and buried IDT are shown in Fig. 3.23. The measured 3rd HWOM corresponds to the SAW mode at which the device operated at a frequency of 1.245 GHz and 1.35 GHz for the exposed and buried IDTs, respectively, which confirms the simulations results in Figure 3.20 and 3.22. The background noise and peak intensity of exposed IDT is -31 dB and -18 dB. Through buried IDT structure, the background noise level reduces to -60 dB and signal peak increases to -13 dB. The signal to noise ratio is significantly improved due to the reduced loss by adapting buried IDT. In original exposed IDT design, besides the intentionally induced n-ZnO layer under gate area for tuning purpose, there are two additionally loss mechanisms.

During SAW generation, the voltage difference applied on neighboring IDT fingers creates the separated charge distribution on both sides of piezoelectric material and. However, with the n-ZnO underneath the IDT and piezo layer, the charges at the bottom would recombine and convert energy into an ohmic loss. This layer has no function in conductivity tuning but merely reduces the SAW intensity. The second loss is caused by Ti/Au top electrode which is placed directly on the launching path of SAW. Due to this layer, the acoustic waves are partially absorbed, resulting in another loss in SAW momentum energy. By adapting the advanced buried IDT process, the PR layer from n-ZnO etching provides enough contract for layer lithography process. Thus, the unnecessary n-ZnO could be removed without any process challenges and thus reduce the SAW generation related loss. With IDT being moved down to n-ZnO layer, the top metal gate is 0.8 μm away from the acoustic wave propagation surface; it reduces the ohmic loss from Au/Ti pad in exposed IDT structure. Also, because the IDTs are brought close to the GaN layer, a larger portion of the acoustic wave will penetrate into GaN film thus increase the SAW velocity and frequency. As a result, the 3rd HWOM holds a center frequency of buried IDT 1.35 GHz, as opposed to 1.245 GHz for exposed IDT.

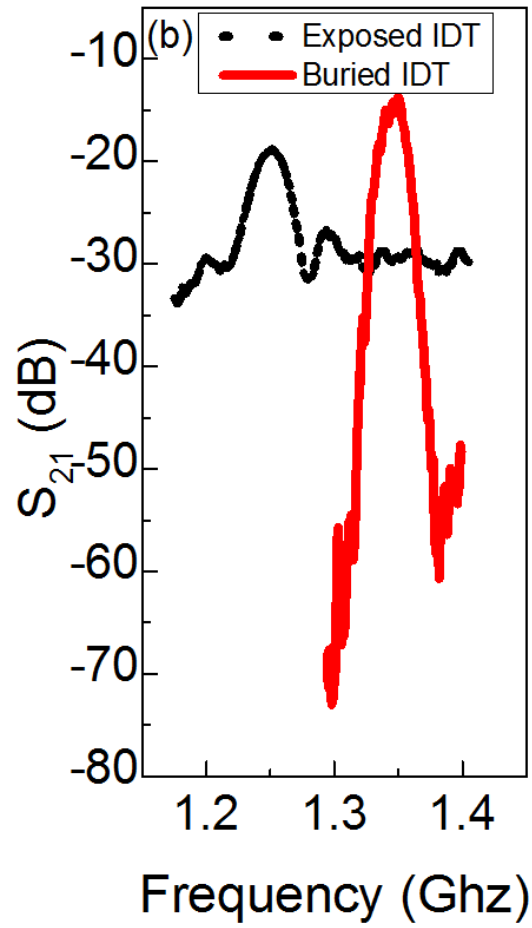


Figure 3. 23: Typical transmission spectrum for the tunable SAW devices with exposed and buried IDT.

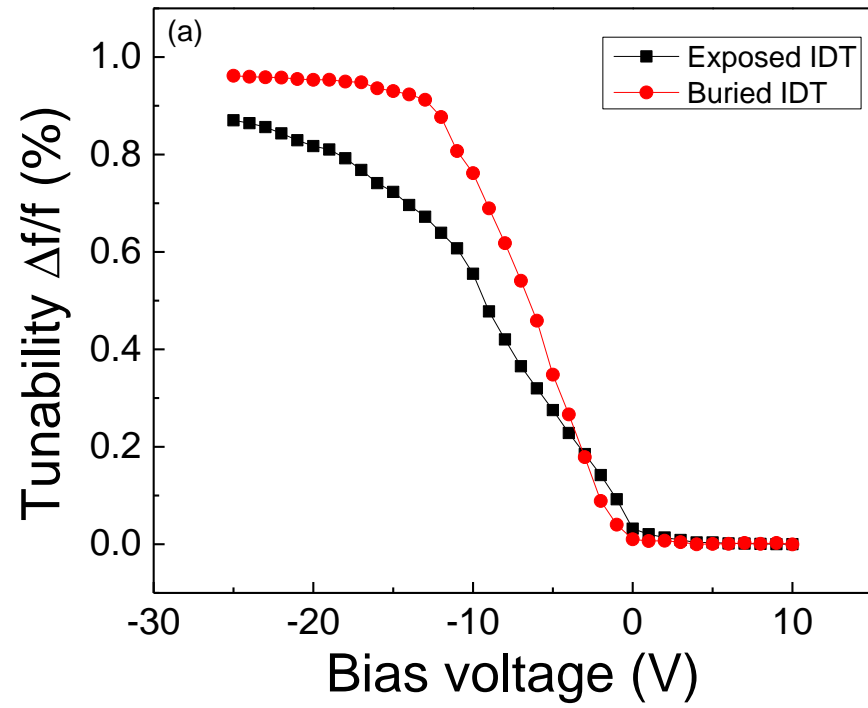


Figure 3. 24: Normalized frequency changes vs. bias voltage for devices with exposed and buried IDT.

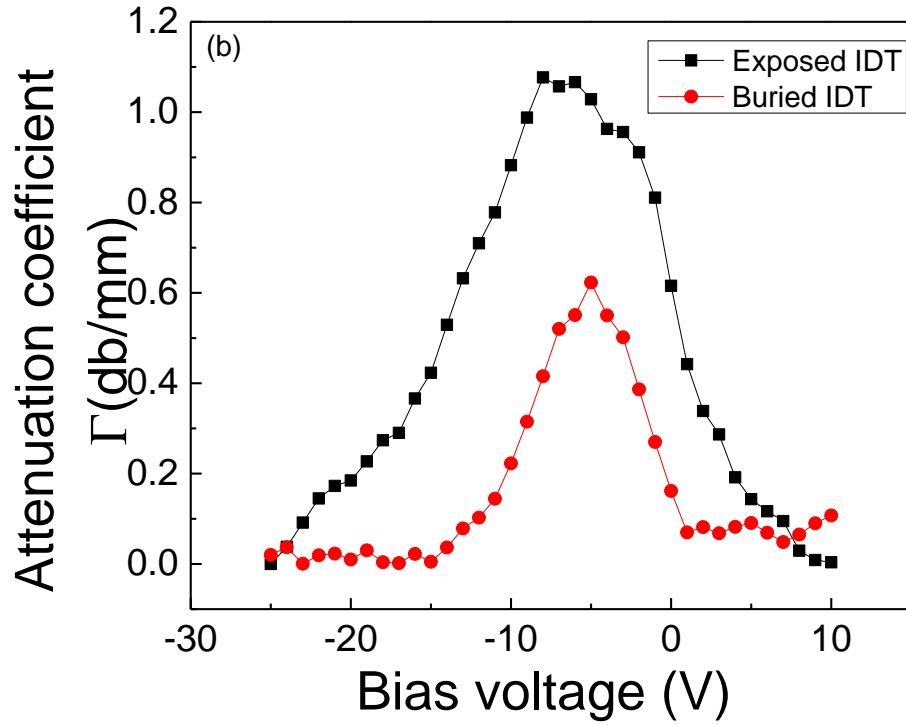


Figure 3. 25: SAW attenuation coefficients as a function of bias voltage for devices with exposed and buried IDT, respectively.

Figure 3.20 presents the frequency tunability $\Delta f/f$ (normalized frequency change) of the NZO/ZnO/GaN -based SAW devices with exposed and buried IDTs as a function of gate bias. In both configurations, all layer thicknesses are kept the same except the IDTs position in the structure. The frequency change of the SAW device increases continuously towards to negative gate bias voltage due to the depletion of the charges in the n-ZnO/GaN hetero-interface and the charges of the free carrier in the n-ZnO layer. The maximum normalized frequency changes $\Delta f/f$ reaches close to 0.9% at -25 V for exposed IDT SAW.

However, for buried IDT SAW, the tunability increases to the same level (0.9 %) merely from -12 V to 0 V. The modulated conductivity achieves the frequency change by

gate bias voltage induced charge depletion. In the buried IDT structure, an acoustic wave is directly traveling through the tuning layer, the acoustic-electric interaction is enhanced thus increases the overall tunability and reduces the required biasing voltage. The measured SAW attenuations of the two devices are shown in Figure 3.25. The maximum attenuations for the devices with exposed and buried IDT are 1.1 dB/mm and 0.6 dB/mm, respectively. The reduced amplitude of attenuations could be attributed to the smaller total loss of the buried IDT structure. In buried IDT structure, the patterned n-ZnO is isolated from neighboring device, removes the possible charge leak path existing in the exposed IDT devices. The increased tunability lowered biasing voltage and expanded linear tuning range are particularly desirable in portable, lower power consumption smart systems.

3.6 Summary

In conclusion, we have demonstrated a voltage-tuned SAW phase shifter using the Ni-ZnO/*n*-ZnO/GaN/c-Al₂O₃ multilayer structure. High-frequency operation at GHz is achieved by using the higher-order mode acoustic wave resulted from the unique SAW dispersion relationship in ZnO/GaN. The acoustoelectric interaction in the piezoelectric-semiconductor structure is used to realize frequency tuning through free charge modulation in the semiconductor n-ZnO layer and confined charge modulation in the *n*-ZnO/GaN heterojunction. Device structure optimization is done through the design of buried IDT. Compared with exposed IDT structure, the buried IDT configuration reduces overall ohmic loss, thus improves the signal to noise ratio. It also enhances the frequency tunability and reduces the biasing voltage range. Buried IDT voltage tunable ZnO/GaN presents a higher frequency, higher tunability, and a lower voltage biasing. The maximum SAW velocity tuning of 0.9% is achieved at 1.35 GHz center frequency, equivalent to a frequency change

of 12.15 MHz. It operates linearly under low gate bias voltage (-12 V, 0 V), at the tuning rate of 0.075% per-volt, corresponding to 1.01 MHz/V. These features are promising for a portable low-power intelligent platform, such as programmable radio-frequency.

Chapter 4. Tunable Surface Acoustic Wave Device Integrated with Thin Film Transistor Glass

In chapter 3, a tunable surface acoustic device has been demonstrated based on MIS structure and ZnO/GaN heterostructure. However, the device tunability depends heavily on the GaN/c-Al₂O₃ substrate and the top metal gate screens other external signal and limits the further application of sensing. Till to date, most tunable devices are based on single crystal materials such as LiNbO₃[3], [4], [9], STO[5] and GaN/Al₂O₃[7], [8], no tunable SAW on transparent glass has been reported. It is necessary to design and develop a bottom gate tunable SAW, of which tunability is less dependent on the substrate material. This device offers 1) the possible application in tunable SAW sensing device with the large area top surface opening. 2) The feasibility of low cost and transparent application using glass or other flexible substrates.

In this chapter, we report a voltage-controlled tunable SAW device on glass using a dual layer structure consisting of a piezoelectric Ni-doped ZnO (NZO) and a semiconductor Mg-doped ZnO (MZO) thin film. The NZO SAW delay line is directly deposited on the bottom gate MZO thin film transistor (TFT) which is made on a glass substrate. It has been demonstrated a small percent of Mg doping into a ZnO channel could improve the thermal stability,[98] as well as the negative bias stress stability[99] as the doped Mg suppresses oxygen vacancies in active channel benefit from the stronger Mg-O bonding. The voltage-controlled frequency tuning is achieved through the acoustoelectric interaction in the MZO-NZO dual layer. Employing TFT to modulate conductivity; therefore, the SAW velocity provides fast charge accumulation and depletion. It increases the dynamic tuning speed. Furthermore, it induces additional fine tuning through the TFT

drain-source voltage V_{ds} . Such a double-input tuning device enables to increase the security level for the encrypted programmable communication at a hardware level, which is desired for certain applications like frequency-hopping spread spectrum.

4.1 Vertically Integrated TFT-SAW Device Structure

The schematic layer structure of a tunable SAW-TFT on glass is shown in Figure 4.1. The Corning® Willow® Glass was chosen as the substrate due to its excellent strength and flexibility. This structure consists of two different types of devices vertically integrated: a staggered bottom gate MZO TFT ($W/L=1200\text{ }\mu\text{m}/400\text{ }\mu\text{m}$) is aligned along x -direction, as the cross-sectional drawing shown in Figure 4.2; and (2) an NZO piezoelectric film is deposited on the top of the TFT channel, serving as a passivation layer and as a SAW medium, as shown in Figure 4.3. 50nm thick Cr was deposited and then patterned on a glass substrate as the bottom gate followed by 100nm SiO_2 deposition as the gate dielectric layer through Plasma Enhanced Chemical Vapor Deposition (PECVD) using SiH_4 and N_2O as precursor gasses on top as gate dielectric layer.

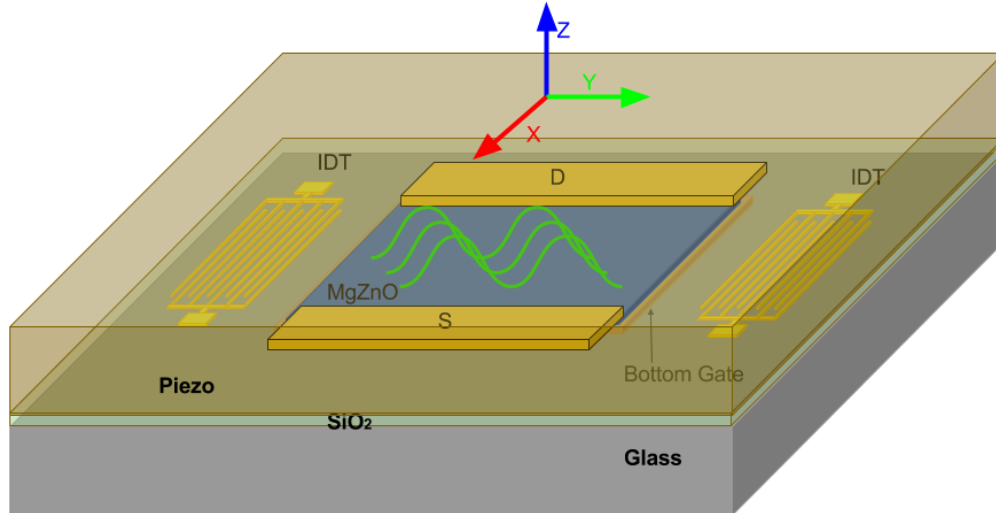


Figure 4. 1: 3D schematic representation of the MgZnO based tunable SAW device on glass.

For the comparison, two types of channel were deposited on SiO₂ dielectric layer: (i) a single layer (SL) of 50 nm Mg_{0.03}Zn_{0.97}O (MZO), and (ii) a dual layer (DL) structure consisting of 5nm MgO intermediate layer followed by a 40nm MZO layer, both of which were deposited using Metal Organic Chemical Vapor Deposition (MOCVD) technique. MgO is deposited on SiO₂ substrate was deposited using MCp₂Mg (bis(methylcyclopentadienyl)magnesium) and O₂ (99.999%) as precursors, respectively. Following MgO deposition, a 40 nm MZO layer is deposited directly on the MgO using DEZn (diethyl zinc) MCp₂Mg (bis(methylcyclopentadienyl)magnesium) and O₂ (99.999%) as precursors without a vacuum break. After channel growth, another 50 nm Cr layer was deposited by electron beam evaporation and then patterned by dry etching, to form the source (S) and drain (D) contacts of the TFT, as well as the IDTs of the SAW delay. A 1.6 μm thick piezoelectric Ni:ZnO (NZO) layer was deposited using RF sputtering (5 at. % Ni in the target) to form the SAW device with IDT underneath the piezoelectric layer. There are 20.5 pairs of the electrode for each IDT with a period of 8 μm. The acoustic waves generated from the bottom surface of the piezoelectric layer are proximity close to the MZO TFT channel layer that enhances the coupling acoustoelectric effect.

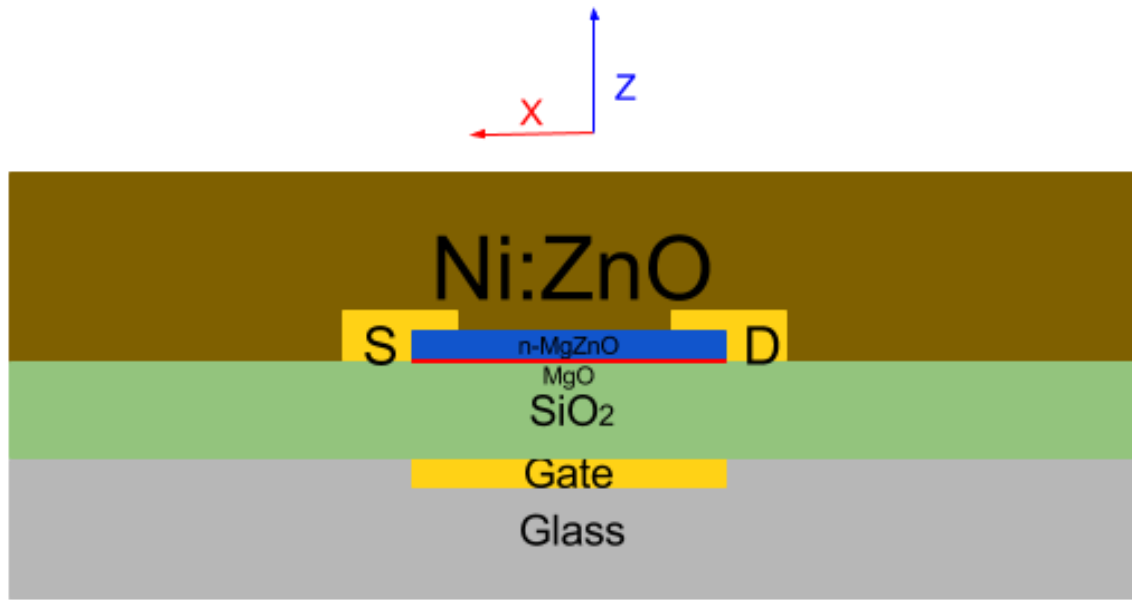


Figure 4. 2: TFT settings in the z - x plane with S and D contacts.

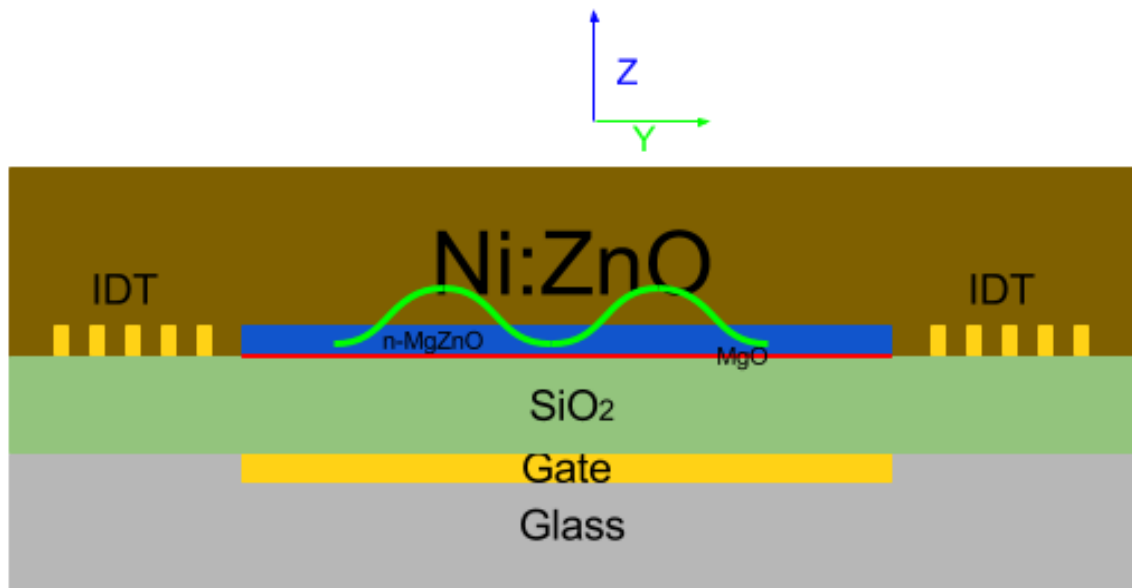


Figure 4. 3: SAW configuration in a y - z plane with IDT buried between SiO_2 and piezoelectric NZO layer.

4.2 Material Characterizations

Figure 4.4 shows X-ray diffraction (XRD) scan of a piezoelectric NZO film on glass with only two peaks from (0002) and (0004), indicating the as-deposited NZO film has preferred c-axis orientation. This is desired for a piezoelectric film with high electrical-mechanical coupling and low loss. The roughness of the film surface is measured by scanning an area of $5 \times 5 \mu\text{m}^2$ using atomic force microscopy (AFM, Park System NX-10) under a tapping mode at 330 kHz as shown in as shown in Figure 4.5. The value of root-mean-square (RMS) roughness of the $1.6 \mu\text{m}$ thick piezoelectric NZO layer on glass is estimated to be $\sim 3.3 \text{ nm}$, indicating the smooth and uniform surface of the NZO film. Figure 4.6 (a) and (b) show the scanning electron microscopy (SEM) images of a cross section and a bird view of an NZO film grown on glass using Hitachi S-800 with an acceleration voltage of 5 KeV. The columnar structures are observed along c-axis (0002) direction, which is consistent with the XRD spectrum.

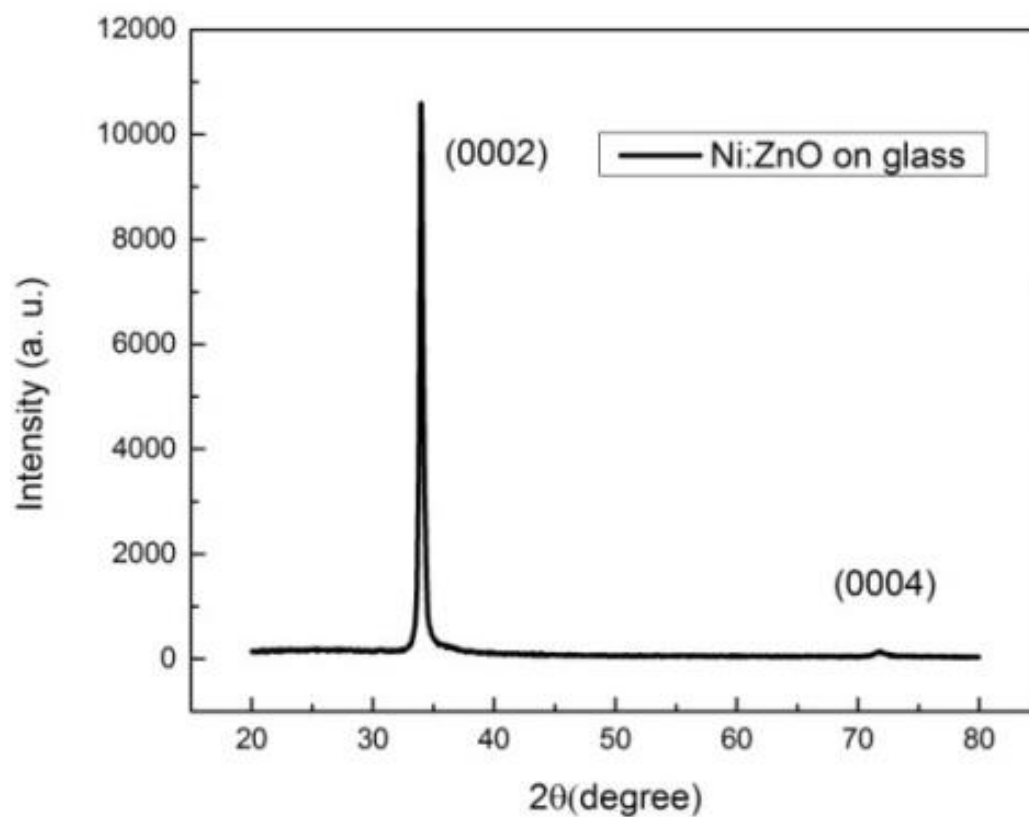


Figure 4. 4: XRD patterns of c-oriented NZO film grown on a glass substrate.

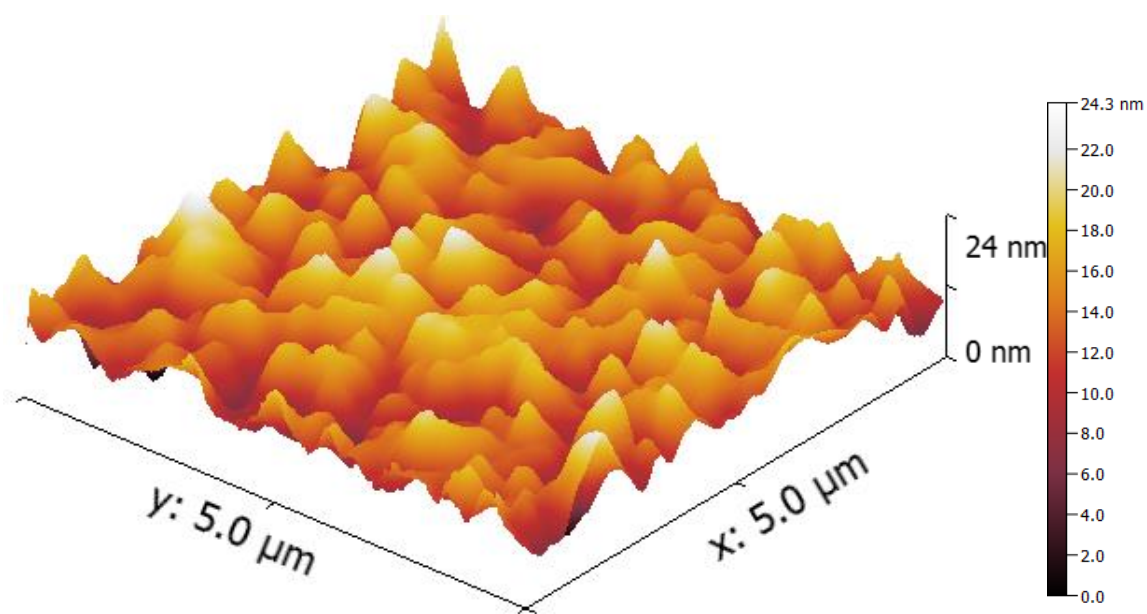


Figure 4. 5: AFM image of an NZO film grown on a glass substrate.

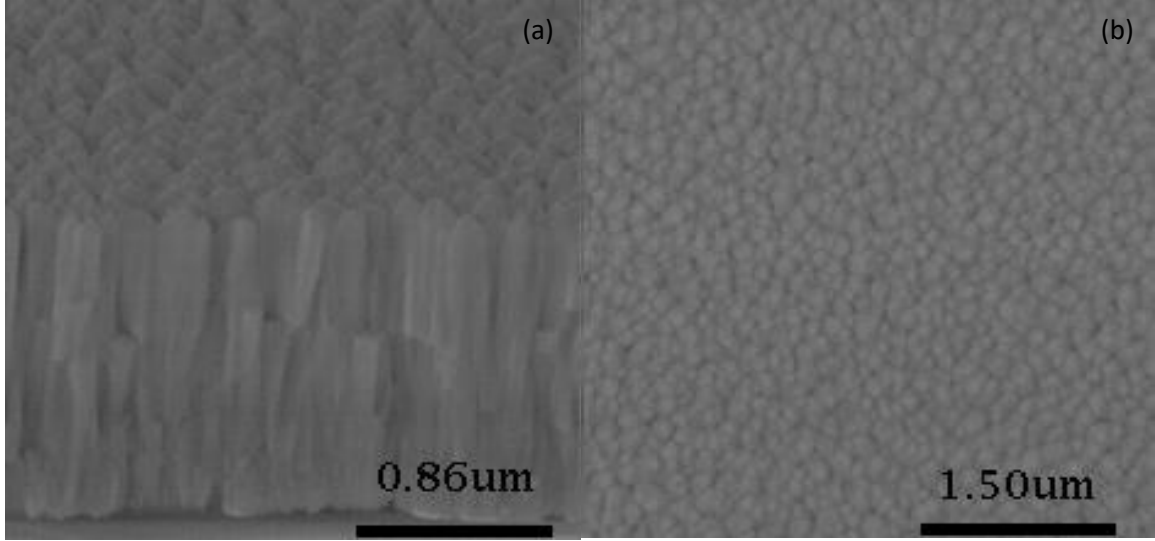


Figure 4. 6: (a) Cross-sectional SEM image of NZO film directly grown on a glass substrate. (b) Bird view SEM image of NZO film directly grown on a glass substrate.

4.3 SAW Characteristics in NZO Piezoelectric Layer

As shown in Figure 4.3, the Cr bottom gate of the TFT would absorb the energy of SAW traveling along the bottom piezoelectric surface. SiO₂ thickness t_{SiO_2} determines the distance between Cr gate pad and the piezoelectric NZO layer. A thinner t_{SiO_2} could increase SAW energy loss due to the metal pad, thus reduce the electromechanical coupling coefficient K^2 ; however, the larger t_{SiO_2} would require a higher gate bias voltage. The effect of SiO₂ thickness on electromechanical coefficient K^2 is simulated using the multilayer transmission line model (TLM).[100], [101] As shown in Figure 4.7, K^2 with various SiO₂ thickness (50 nm, 100 nm, 150 nm, 200 nm, and 250 nm) is plotted as a function of the SAW center frequency. Figure 4.8 plots K^2 simulated at fixed frequency (330 MHz) over SiO₂ thickness. The effective coupling coefficients are calculated to be 0.62%, 1.76%, 2.24%, 2.64%, and 2.66%, respect to t_{SiO_2} of 50 nm, 100 nm, 150 nm, 200 nm, and 250 nm, respectively. The rapid increase of K^2 can be attributed to the better shielding effect

provided by a thicker SiO₂ insulator layer. However, with SiO₂ thickness above 200 nm, in addition to the curve peak shifting to a lower frequency, the coupling coefficient only shows a slight increase. It is found that a further increase in t_{SiO_2} does not significantly benefit the acoustoelectric coupling, but would increase the required gate biasing voltage. The simulation results indicate that the thickness of the SiO₂ has the significant influence on the effective coupling coefficient, and correspondingly, the SAW velocity tunability. In this work, the t_{SiO_2} is designed to be the optimized value 200 nm.

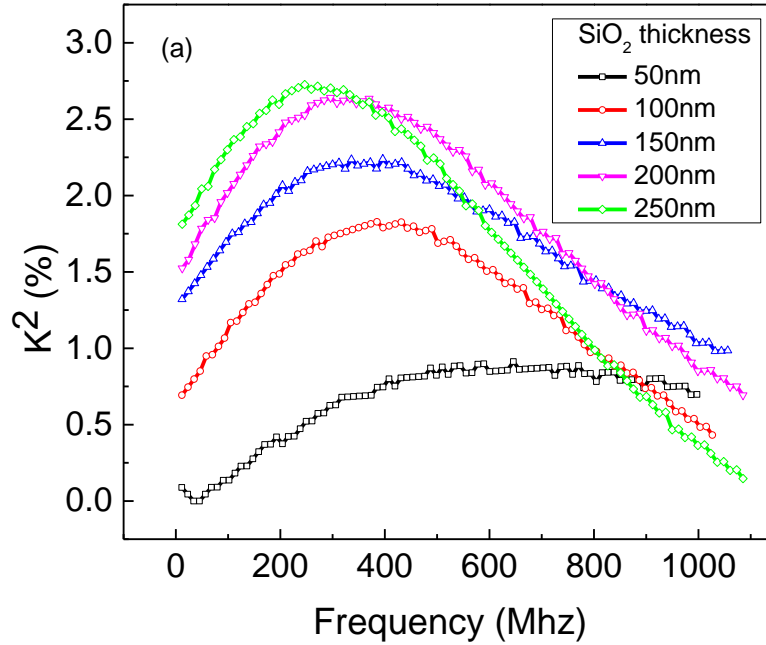


Figure 4. 7: The electromechanical coefficient K^2 versus operating frequency for TFT-SAW devices with different SiO₂ thicknesses.

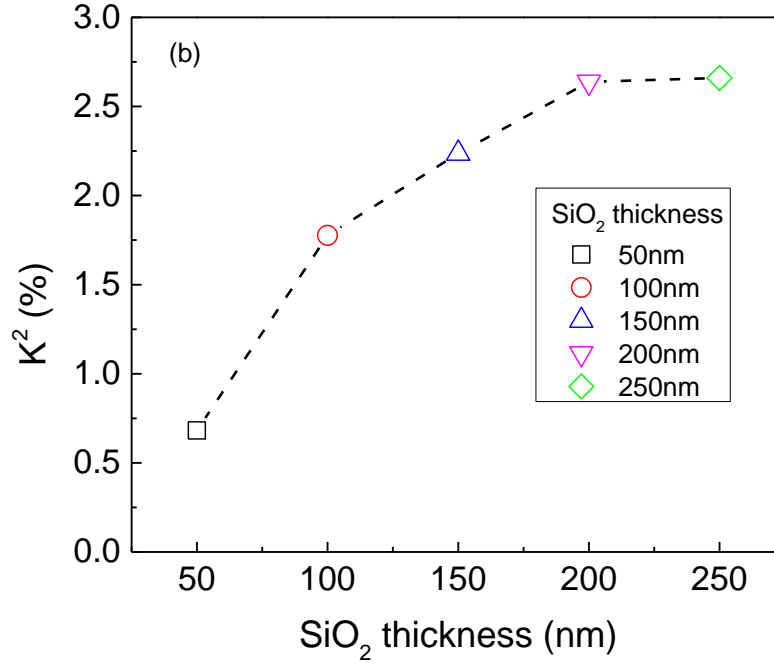


Figure 4. 8: The K^2 versus SiO₂ layer thickness at the center frequency of 330 Mhz.

This device structure provides several unique advantages: (1) by using both two top electrodes as ground. The frequency tuning is achieved solely through gate voltage modulation by the static electric field in a Metal-Oxide-Semiconductor structure. (2) By applying a horizontal voltage between tow electrodes, the semiconductor part of this device is functionalized as a thin film transistor, as shown in Figure 4.3. Additional tuning capability is induced by the source to drain voltage V_{ds} . The vertical integration of SAW (top) and TFT (bottom) enables a dual input tuning device. (3) It has been demonstrated buried IDTs provides high coupling coefficient and low loss.[102]–[104] Also, acoustic waves generated at bottom surface piezoelectric layer lies in the same level with charge layer (MgZnO) will enhance the direct coupling between electrical energy loss and mechanical movement. (4) The device is fabricated on a glass substrate, using

polycrystalline n-MgZnO and piezoelectric Ni:ZnO for inexpensive, transparent applications.

4.4 Operation Principle

When SAW propagates in a piezoelectric material, an electric field is generated accompanying with mechanical movement. In a piezoelectric-semiconducting (MZONZO) system, this electric field could couple with the carriers existing in the semiconducting MZO layer. The modulation of MZO sheet conductivity σ_d causes changes in SAW attenuation and frequency. The SAW frequency change Δf is defined as the difference between modulated operating SAW frequency f and the unmodulated center SAW frequency f_c . If the semiconductor thickness in the dual-layer structure is much smaller than the acoustic wavelength, the SAW frequency change Δf respect to SAW center frequency f_c and the attenuation Γ can be written as[6]

$$\frac{\Delta f}{f_c} = \frac{K_{eff}^2}{2} \frac{1}{1 + (\sigma_d / \sigma_M)^2}, \quad (4.1)$$

$$\Gamma = k \frac{K_{eff}^2}{2} \frac{(\sigma_d / \sigma_M)}{1 + (\sigma_d / \sigma_M)^2}, \quad (4.2)$$

where v_{sc} is the acoustic velocities when the semiconductor layer is undepleted, K_{eff}^2 denotes the effective electromechanical coupling coefficient of the device, k is the SAW wave vector, $\sigma_d = \int_0^t \sigma_{(z)} dz$ is the average sheet conductivity of semiconductor layer with thickness t , σ_M is the relaxation conductivity at the maximum attenuation, given by $\sigma_M = v_{oc}(\epsilon_p + \epsilon_s)$. v_{oc} is the acoustic velocity when the semiconductor layer is fully depleted, ϵ_p and ϵ_s are the dielectric constants of the piezoelectric and semiconducting layer, respectively. The normalized frequency shifts ($\Delta f/f_c$) are derived by:

$$\frac{\Delta f}{f_c} = \frac{\lambda}{L_{delay}} \frac{\Delta \phi}{360^\circ}, \quad (4.3)$$

where $\Delta \phi$ is the SAW phase shift, λ is the SAW wavelength, and L_{delay} is the edge-to-edge distance between IDTs.

In the MZO-NZO TFT-SAW structure, the SAW velocity and the frequency tuning in NZO are modulated by the sheet conductivity change ($\Delta \sigma_d$) in the underneath semiconductor MZO layer. The conductivity response to gate voltage is critical for frequency tuning, as the rapid conductivity change over gate voltage is the primary concern to achieve fast frequency tuning. Moreover, the starting point of this quick conductivity change defines the minimum dc bias reference that enables frequency tuning. To achieve the low voltage operation requirement, a closed-to-zero starting voltage is preferred for a tunable SAW.

4.5 TFT Transfer Characteristics

The frequency tunability $\Delta f/f_c$ of this TFT-SAW is depicted in Figure 4.9 with the minimum tunability aligned to zero. The maximum tunability of 0.25% is obtained at a high bias voltage range between -34 V and -14 V. Such a high gate bias voltage range and small tunability make this device unsuitable for portable applications. Also, shown in Figure 4.10 is the I_{ds} - V_{gs} transfer characteristics of *regular* MZO TFT with $V_{ds}=0.1$ V. The onset of SAW tunability curve aligns well with the turn-on voltage V_{on} in the *regular* MZO TFT's I_{ds} - V_{gs} curve. When gate-source voltage V_{gs} is less than the turn-on voltage V_{on} , defined by the gate voltage at which the drain current begins to increase in an I_{ds} - V_{gs} curve, the electron density is not high enough create a conducting channel. Thus device operates in the cut-off region. While $V_{gs} > -34$ V and $V_{gs} > V_{ds}$, a bias to the gate electrode enhances

the accumulation of electrons in the channel layer and small V_{ds} biases the TFT into the linear region. The electrons accumulate in the channel layer; the electrical field in x -direction leads to the I_{ds} current flow from source to the drain. The inferior I - V characteristics of this sizable *regular* MZO TFT are also presented by the large sub-threshold swing ($S.S.=\Delta V_{gs}/\log(\Delta I_{ds})$) value of 2.52 V/Dec. In tunable TFT-SAW, $S.S.$ is the inverse current/conductivity response over gate voltage. Higher $S.S$ value indicates smaller sub-threshold slope and less current increase per unit gate voltage. The frequency change is sensitive to the increase rate of the I_{ds} , which corresponds to the sub-threshold of the *regular* MZO TFT. A tunable TFT-SAW device with a larger $S.S.$ requires high gate voltage to achieve a limited frequency tuning. Furthermore, the dynamic voltage control range (-34 V~ -14 V) in which the SAW frequency is tuned in the large reverse biasing region is unfavorable for device operation, especially for the smart sensors and reconfigurable and portable RFID. To achieve a SAW frequency tuning at low voltage operation, a closed-to-zero V_{on} and a small $S.S.$ are preferred.

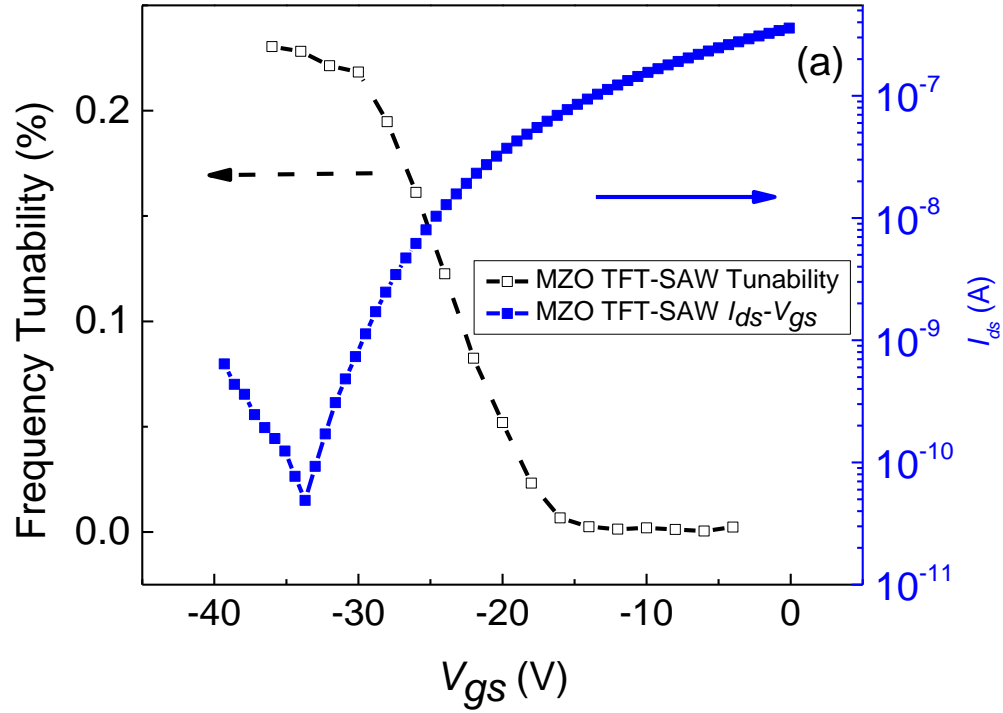


Figure 4. 9: Measured frequency change and measured I_{ds} - V_{gs} transfer characteristics of the *regular* MZO tunable SAW device. V_{ds} is fixed at 0.1 V.

To enhance the SAW tunability under a low biasing voltage, we have designed and engineered the interface between MZO channel and SiO_2 gate dielectric layer by inserting a 5 nm MgO layer. The MgO is selected as the interfacial transition layer due to its wide bandgap (7.8 eV), high thermal conductivity[105] and a large dielectric constant.[106] MgO has been successfully applied as buffer layer[107]–[112] in epitaxial ZnO growth to reduce lattice mismatch and improve crystal quality. In this work, an ultrathin MgO is deposited on SiO_2 , then followed by deposition of an MZO channel layer. The device made by using such interface modulation is defined as *m*-MZO-NZO TFT-SAW to differentiate from the *regular* MZO-NZO TFT-SAW. Figure 4.10 shows the frequency tunability and

I_{ds} - V_{gs} characteristics of the *m*-MZO-NZO TFT-SAW device. 0.53% frequency tuning is achieved within 0-12 V range. Similar as in Figure 4.9, the starting voltage of frequency tuning aligns with V_{on} voltage in I_{ds} - V_{gs} characteristics, indicating the tunability is governed by gate voltage V_{gs} induced conductivity/current change. In comparison with the *regular* MZO-NZO TFT-SAW in Figure 4.9, the *m*-MZO-NZO TFT-SAW device in Figure 4.10 shows a significant increase in frequency tunability (0.53% vs. 0.25%) and a decrease in bias voltage level (0 to 12V vs. -34 to -20V) over the *regular* MZO-NZO TFT-SAW. Moreover, the I_{ds} - V_{gs} characteristics of *m*-MZO-NZO TFT-SAW show a much steeper sub-threshold slope (0.41 V/Dec) over the *regular* MZO-NZO TFT-SAW (2.52 V/Dec). The V_{on} is right shifted from -35 V in *regular* MZO-NZO TFT-SAW to 1.4 V in *m*-MZO TFT. Thus the voltage control ranges corresponding the frequency tuning are adjusted to 0 to 12 V, favorable for the operation.

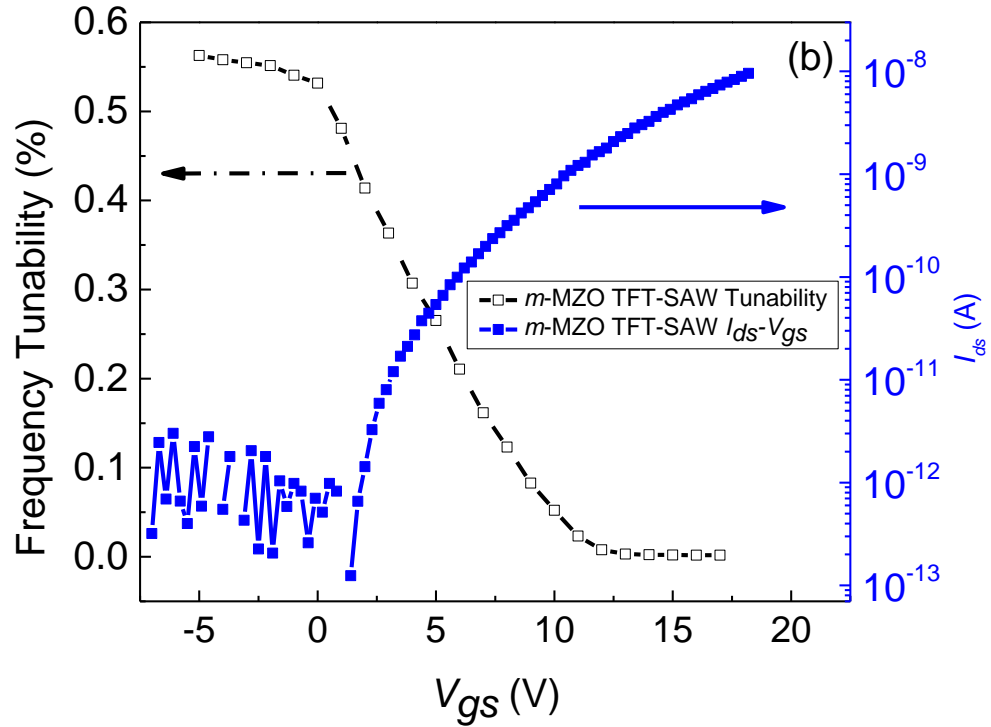


Figure 4. 10: Measured frequency change and measured I_{ds} - V_{gs} transfer characteristics of the m -MZO tunable SAW device. V_{ds} is fixed at 0.1 V.

The improvement of $S.S.$ value relates to the reduction of the total defect density a TFT. Considering that the identical growth conditions of both TFT channels and same SiO_2 thickness, it is reasonable to attribute the performance differences between *regular* MZO device and m -MZO device to the modification of the channel and dielectric interface. The mechanism of the improvement of SAW tunability is studied through comprehensive characterizations and analysis. Shown in Figure 4.11 (a) is the cross-sectional transmission electron microscopy (TEM) images of SiO_2 /MZO interface region of an MZO TFT structure. Within the clear layer structure, the nanocrystal structures in a diameter of 1 nm-5 nm are seen in the amorphous SiO_2 layer, pointed by the black arrows. An energy-

dispersive X-ray spectroscopy (EDS) line scan (~10 points, indicated by the red dots) is performed from MZO layer to SiO₂ layer, and the atomic percentage of Zn and Si are plotted as a function of the scan distance in Figure 4.11 (b). Within MZO region, Zn is the major element and counts for ~90% of total intensity. Near the MZO-SiO₂ interface region, Zn concentration slowly ramps down to 40%. However, in SiO₂ region, a significant amount of Zn (20%) is still detected. The EDS point spectrums are shown in Figure 4.11 (c), corresponding to the three locations: inside the MZO layer, at SiO₂/MZO interface, and inside the SiO₂ layer marked in Figure 4.11 (a) and (b). In MZO layer (green dashed box), in addition to Zn peaks, a small Si peak coexists. At the interface of SiO₂/MZO (purple dashed circle), the intensity of Zn peak gradually decreases while Si peak increases concomitantly. Further moving into the SiO₂ layer (blue dotted box), a high Si peak is detected, and the Zn peak is still observed. It should be noted that no Mg peak is observed during the scanning because the low atomic percentage (~3%) of Mg in MZO is below the detection limit. The EDS results confirm that the nanocrystal structures labeled by the black arrows in the interface and SiO₂ regions of Figure 4.11 (a) are composed of Zn atoms. The interchange of peak intensities at different locations prove intermixture of Zn and Si in SiO₂ layer.

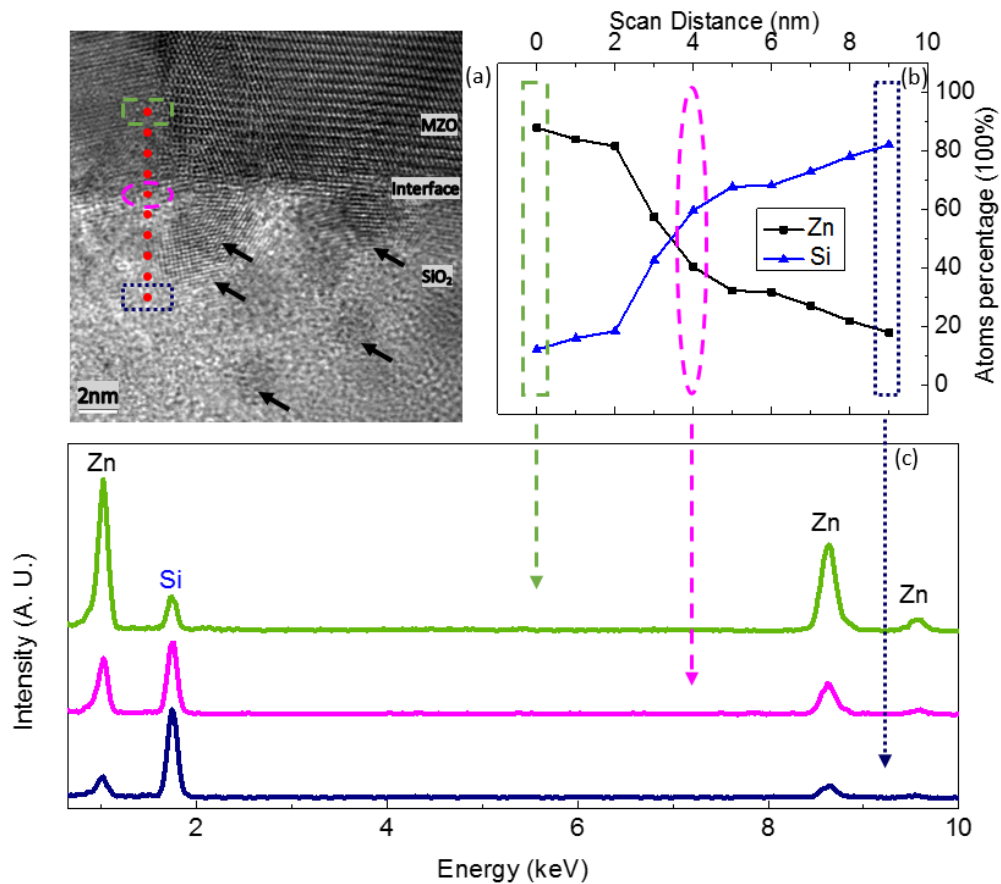


Figure 4. 11: (a) Cross-section TEM of SiO₂/MZO structure, the black arrows indicate the nanocrystal structure found in amorphous SiO₂; (b) EDS line scan from MZO layer to SiO₂ layer; (c) the EDS point detection results corresponding to the labeled positions at three locations in (a) and (b): MZO (green dashed box), interface (purple dashed circle), and SiO₂ (dark blue dotted box).

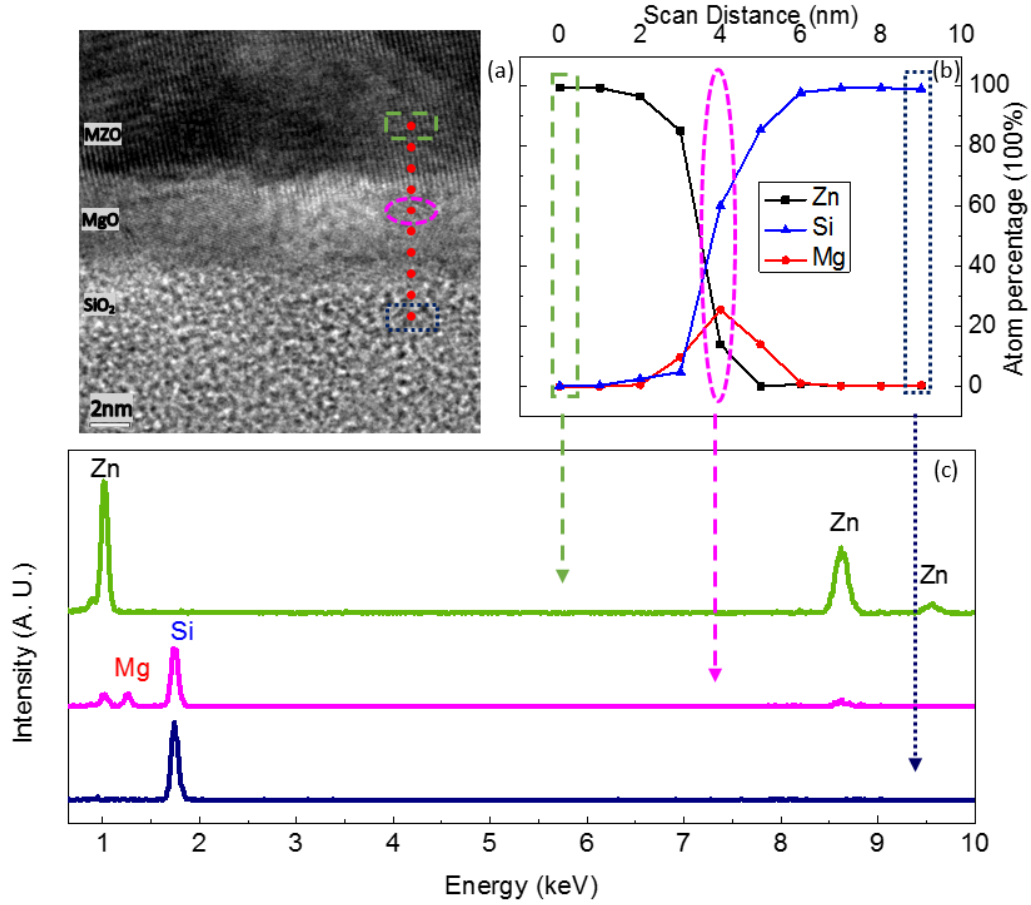


Figure 4. 12: (a) Cross-section TEM of SiO₂/MgO/MZO structure; (b) EDS line scan from MZO layer to SiO₂ layer; (c) EDS point spectrum results corresponding to the labeled positions at three locations in (a) and (b): MZO (green dashed box), MgO (purple dashed circle), and SiO₂ (dark blue dotted box).

In contrast, the cross-sectional TEM image of interface modified *m*-MZO structure shows a nanocrystal-free amorphous SiO₂ layer in Figure 4.12 (a). Similar as in the *regular* MZO TFT case, EDS line scans are performed from MZO to SiO₂, and the atomic percentage of Zn, Mg, and Si are plotted against scan distance as shown in Figure 4.12 (b). Due to the same growth conditions between the *regular* MZO and *m*-MZO channel, 90% of total atoms are Zn, similar to the Zn profile in MZO shown in Figure 4.11 (b). However

in MgO region, as opposed to the *regular* MZO TFT without inserting of the MgO layer in the SiO₂/MZO interface, Zn percentage declines rapidly as Mg percentage increases. Quickly after the turning point of Mg concentration, essentially there is no Zn signal detectable in the SiO₂ region. The same EDS analysis is also performed on *m*-MZO as on the *regular* MZO structures. Within MZO layer (green dashed box), the same Zn peaks are found without the presence of Si peak. In MgO region (purple dashed circle), a new Mg peak is detected, and the Zn peaks decrease dramatically in comparison with the Zn peak intensity at the *regular* SiO₂/MZO interface. Further moving into SiO₂ region (dark blue dotted box), only Si peak is observed without showing Zn peaks. The EDS scan profiles in Figure 4.11 (b) and Figure 4.12 (b) demonstrate that MgO layer in *m*-MZO-NZO TFT-SAW successfully suppressed the interface diffusion of Zn and Si. Thus SiO₂ gate dielectric layer remains intact without being damaged by Zn diffusion.

Zn diffusion would degrade the SiO₂ dielectric layer. It has been proved that at or above 400K; Zn⁰ is oxidized into the Zn²⁺ state in the oxide matrix.[113] Once Zn²⁺ diffuses into the SiO₂ dielectric layer and being trapped, it becomes a fixed charge that attracts electrons, resulting in a negative shift in threshold voltage. This explains the turn-on voltage shift, as well as the significant bias voltage difference for frequency tuning, between *regular* MZO-NZO TFT-SAW and *m*-MZO-NZO TFT-SAW. The shift of turn-on voltage can be related to the amount of the extra equivalent oxide trapped charge density (N_{ox}) in SiO₂ layer $N_{ox} = V_{on} \times C_{ox} / q$. Using the V_{on} value of -34 V and 1.4 V for MZO and *m*-MZO TFT, the additional positive charge in the oxide layer reduced by adding MgO layer is calculated to be $3.63 \times 10^{12} \text{ cm}^{-2}$.

During Zn diffusion from MZO to SiO₂, in addition to its effect on the SiO₂ gate dielectric layer, the penetration of Zn atoms will also damage SiO₂/MZO interface and generate Zn vacancy related defects at MZO channel close to SiO₂. The total trap density can be estimated from the *S.S.* of a TFT from the following Equations:[114]

$$S.S. = \log_e 10 \frac{kT}{q} \left(1 + \frac{qN_{total}}{C_{ox}} \right) \quad (4.4)$$

$$N_{total} = D_{it} + tN_{bulk} \quad (4.5)$$

where k is the Boltzmann constant, T is the absolute temperature; q is the elementary electric charge. N_{total} is the total channel defect density, and C_{ox} is the capacitance of the gate dielectric per area. C_{ox} equals to $1.73 \times 10^{-8} \text{ F cm}^{-2}$ and $1.69 \times 10^{-8} \text{ F cm}^{-2}$ for *regular* MZO-NZO TFT-SAW and *m*-MZO-NZO TFT-SAW, respectively. From Figure 4.9 and Figure 4.10, the *S.S.* values are calculated to be 2.52 V/Dec and 0.41 V/Dec, for *regular* MZO device and *m*-MZO device, respectively. N_{total} consists of two terms as shown in Eqn (4.5), interface trap density represented by D_{it} and channel sheet defect density represented by the product of the channel thickness t and the bulk channel trap density N_{total} . The total trap density N_{total} for MZO TFT and *m*-MZO TFT, including the bulk trap (tN_{bulk}) and the interface trap (D_{it}), are calculated to be $4.45 \times 10^{12} \text{ cm}^{-2}$ and $6.28 \times 10^{11} \text{ cm}^{-2}$, respectively. Assume the bulk trap densities are same for the MZO channels of both devices due to the identical growth conditions, the difference of N_{total} between MZO and *m*-MZO TFT is mainly resulted from the different interface trap density D_{it} , which is estimated to be $3.82 \times 10^{12} \text{ cm}^{-2}$. The increased interface defect density in the *regular* MZO TFT would trap electrons and increase the sub-threshold swing, therefore reduce the gate voltage induced conductivity change and degrade SAW frequency tuning.

Thus, by adding an ultra-thin layer of MgO as the diffusion barrier, the concentration of Zn^{2+} in SiO_2 layer and the Zn diffusion induced defects at SiO_2/MZO interface are significantly reduced. The interface engineering in *m*-MZO TFT successfully reduces the biasing voltage, adjusts the turn-on voltage V_{on} close to 0 V, and makes the S.S. steeper than that of the *regular* MZO TFT. The *m*-MZO-NZO TFT-SAW structure increases the SAW frequency tuning range.

4.6 Dual-Voltage Input for SAW Frequency Tuning

Unlike the most tunable SAW devices which only allow one control voltage input for frequency tuning, this *m*-MZO-NZO TFT-SAW provides the unique advantage in SAW frequency tuning through control of both gate voltage and drain voltage. The tunability measurement results of *m*-MZO-NZO tunable SAW using dual input voltages are presented in Figure 4.13, where frequency tunability is plotted against the control voltage V_{gs} with various V_{ds} applied (-10 V, -5 V, 0 V, 5 V, and 10 V). The 330 MHz SAW frequency peak is shown as in the inset. When V_{ds} equals to 0V, the S and D are both grounded; the TFT-SAW operates under the vertical tuning mode through V_{gs} . Under the negative V_{gs} , SAW frequency does not change and shows a flat line. Under positive V_{gs} , frequency tunability starts to drop almost linearly and then turns into flat again when V_{gs} reaches ~12 V. The frequency tunability of 0.53% is achieved under zero S/D bias condition under the gate bias between 0-12 V. In this *m*-MZO-NZO TFT-SAW device, V_{gs} plays a major role in changing average sheet conductivity by modulating the charge accumulation, thus, is the dominant input voltage. At a negative gate voltage ($V_{gs} < 0$ V), the tunability variation caused by V_{ds} change is barely noticeable. However, at positive gate voltage, V_{ds} provides

the fine frequency tuning mode. The overall SAW frequency tuning between 0.63% and 0.46% is obtained for V_{ds} varying between -10 V and 10 V.

The effect of V_{ds} on the sheet conductivity change can be attributed to the channel charge modulation. With $V_{ds} = 0$ V, the sheet conductivity change is directly controlled by gate voltage V_{gs} induced charge accumulation, and the charges are evenly distributed in x direction from S to D. With drain voltage V_{ds} applied, the voltage difference at S end stays the same, however at D side the voltage is changed into $V_{gd} = V_{gs} - V_{ds}$. This voltage difference could extend along the channel towards to S end. When $V_{ds} > 0$ V, effective applied V_{gs} becomes smaller, thus less total charge Q is induced into channel compared with zero V_{ds} case. In other words, with the same V_{gs} applied at the gate, the presence of a positive V_{ds} would partially counterbalance V_{gs} , and reduce the effective conductivity, thus reduce the frequency tunability. On the alternative V_{ds} polarity ($V_{ds} < 0$ V), as effective V_{gs} increases, more charges are present in channel compared with $V_{ds} = 0$ V, the conductivity is further reduced. Thus a higher tunability is reached.

Shown in Figure 4.14 is the SAW attenuation Γ measured respect to the major loss (IL) through the relationship $IL = 20 \log[\exp(-\Gamma \cdot L_{delay})]$. Larger Γ indicates higher energy loss. For all different V_{ds} , the maximum loss happens at $V_{gs} \sim 5$ V. The attenuation increases with negative V_{ds} and decreases with positive V_{ds} . With V_{ds} equals to 0V, the attenuation was 1.75 dB mm⁻¹. With positive V_{ds} , the attenuation coefficient slightly decreased to 1.59 dB/mm at V_{ds} of 10 V; while with negative V_{ds} , attenuation increases to 2.23 dB mm⁻¹ at $V_{ds} = -10$ V. Since positive V_{ds} reduces the amount of charge in the channel layer, it also brings down the overall ohmic loss and decreases SAW attenuation in Figure 4.15.

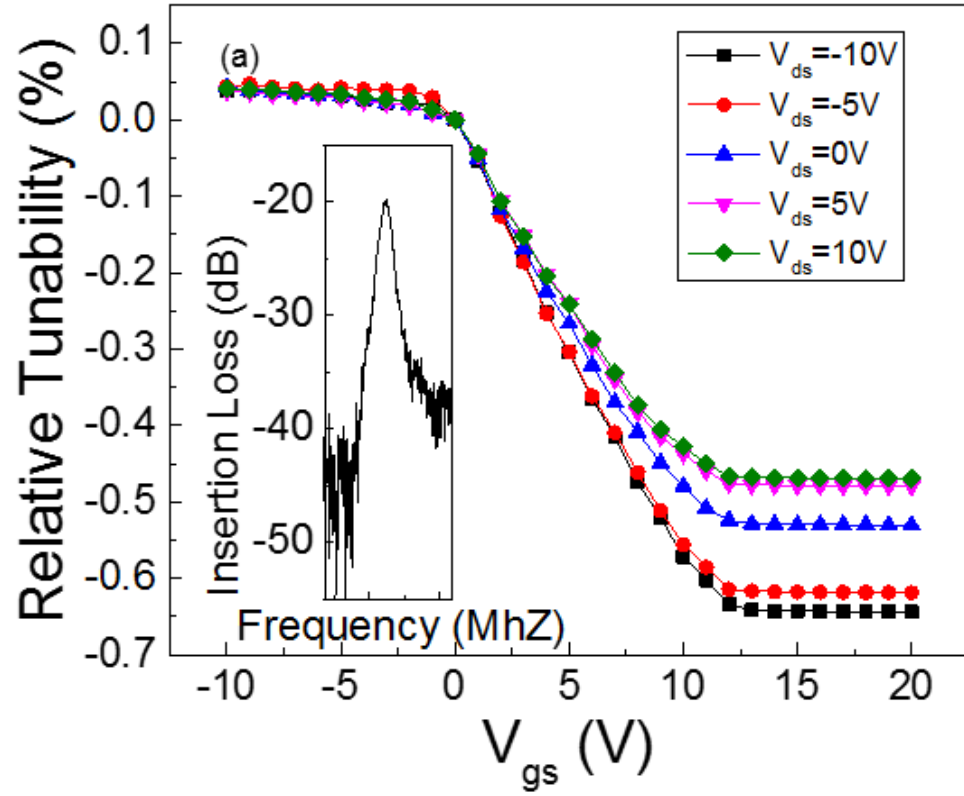


Figure 4. 13: Measured frequency change of the *m*-MZO-NZO tunable SAW device. The different curve represents various V_{ds} voltage (-10 V, -5 V, 0 V, 5 V, 10 V). The inset is 330 MHz SAW frequency peak.

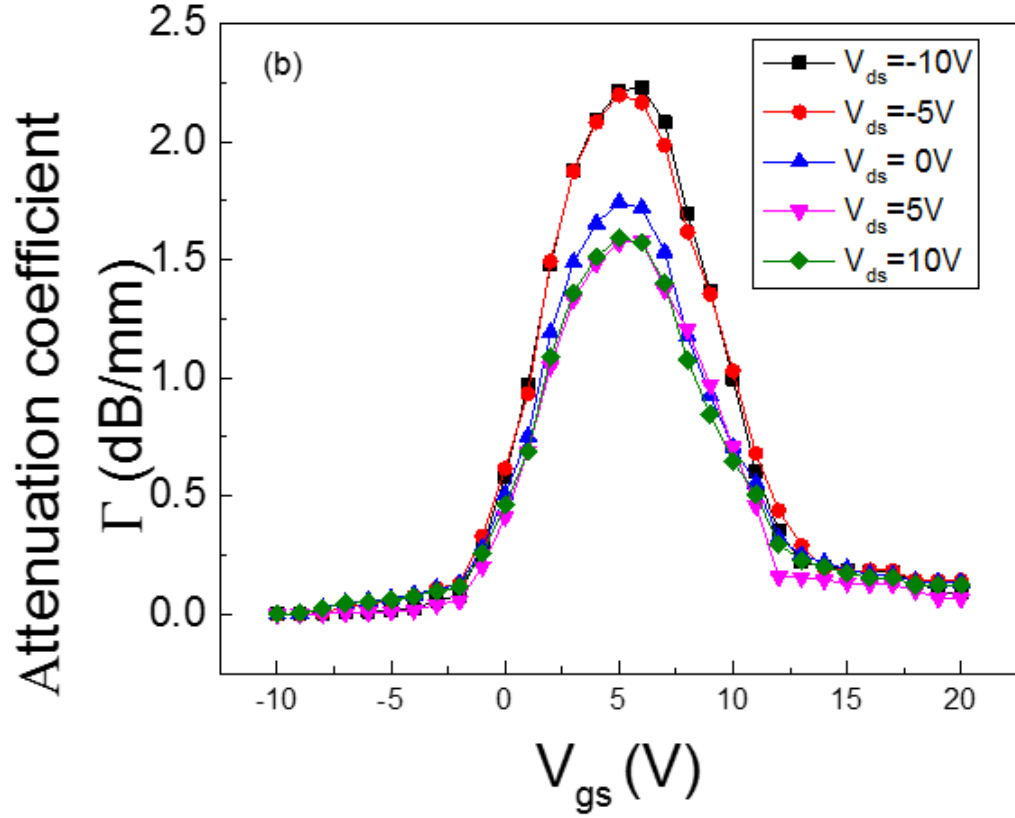


Figure 4. 14: SAW attenuation coefficients as a function of bias voltage V_{gs} . The different curve represents various V_{ds} voltage (-10 V, -5 V, 0 V, 5 V, 10 V).

4.7 Summary

In this chapter, we have demonstrated a dual-voltage-input controlled SAW frequency tuning device by vertical integration of a bottom gate MZO TFT with an NZO SAW delay line on a glass substrate. The device operates at the center frequency of 330 MHz. The acoustoelectric interaction mechanism in the semiconductor/piezoelectric (MZO-NZO) dual layer structure is used to tune the SAW frequency. It is found that the interface diffusion, especially Zn diffusion from MZO channel to SiO₂ gate dielectric layer degrades the MZO TFT and hinders it from effectively tuning SAW frequency. Also, it makes the control voltage for tuning too high to practical applications. The interface

between MZO and SiO₂ in the TFT is engineered by inserting an ultrathin MgO layer as a barrier to suppress the Zn diffusion. The interface modified *m*-MZO-NZO TFT-SAW device shows more than twice frequency tunability ($\Delta f/f_c \sim 0.53\%$) and much lower control voltages ($V_{gs}=0\sim 12\text{V}$) than the *regular* MZO-NZO TFT-SAW ($\Delta f/f_c \sim 0.25\%$; $V_{gs} -30\text{ V}$ to -20 V) without interface modification. The integrated MZO-NZO TFT-SAW device provides the unique dual input voltage (V_{gs} and V_{ds}) control mechanism on frequency tuning. Gate voltage V_{gs} enables the primary frequency tuning mode while the drain voltage V_{ds} provides the fine tuning mode. With 0 to 12 V V_{gs} biasing applied, the SAW frequency tuning of 0.53% is achieved; the frequency tunability can be further finely controlled from 0.46% to 0.63% under the different V_{ds} bias (-10 V to 10 V). By using the dual input voltage mode operation, the *m*-MZO-NZO TFT SAW device extends the frequency tuning range and device flexibility, which are promising for the portable and low-cost reconfigurable systems.

Chapter 5. Conclusions and Future Work

5.1 Conclusions

In the traditional SAW devices, acoustic velocity and frequency cannot be continuously tuned due to the fixed IDT fingers and the delay line length. However, frequency tunability is critically important for many applications, as it enhances design flexibility, allows adaptive signal processing and communication, and enables smart sensing. For example, the tunable SAW biosensor can improve sensitivity and selectivity, extending lifetime by “resetting” the SAW velocity range. The tunable SAW device can also be used as an adjustable RFID tag for wireless identification.

A voltage-tuned SAW phase shifter using the Ni-ZnO/*n*-ZnO/GaN/c-Al₂O₃ multilayer structure is designed and fabricated. Its high-frequency operation at a GHz range is achieved by using the higher-order mode acoustic wave resulted from the unique SAW dispersion relationship in ZnO/GaN. The acoustoelectric interaction in the piezoelectric-semiconductor structure is used to realize frequency tuning through modulation of free charges in the semiconductor *n*-ZnO layer and the confined charges in the *n*-ZnO/GaN heterojunction. The thinner *n*-ZnO layer results in higher frequency tunability. The maximum SAW velocity tuning of 0.9% is achieved at 1.245 GHz center frequency, equivalent to a frequency change of 11.2 MHz. It operates linearly under low gate bias voltage (-10 V, 0 V), at the tuning rate of 0.06% per-volt, corresponding to 747 Hz/V.

To reduce the loss in the ZnO/GaN tunable SAW, the device with the same multilayer structure but with the buried IDT is designed. The buried IDTs are sandwiched between the GaN and the piezoelectric NZO layer, instead of being exposed to air, to improve the acoustic coupling. Compared with the exposed IDT structure, the buried IDT

design reduces overall ohmic loss and improves the signal to noise ratio from 13 dB to 41 dB. It also enhances the frequency tunability from 0.6% to 0.9% at lower biasing voltage range (-12 V, 0 V), and increases the center frequency from 1.245GHz to 1.35GHz. The voltage-controlled tunable SAW technology presents promising potential in adaptive and reconfigurable low power mobile platform, including , adaptive signal processing, secure wireless communication, programmable and resettable sensors.

Before this work, all the reported tunable SAW devices were fabricated on the single crystal substrates, which limited their adaptations in the large-area and low-cost applications, such as disposable sensor and wireless display. For the first time, we have demonstrated a voltage-controlled tunable SAW device on glass operating at the center frequency of 330 MHz. The device consists of the bottom gate MZO TFT vertically integrated with the NZO SAW delay line into an MZO TFT - NZO SAW device on a glass substrate. The interface engineering is conducted by adding an ultrathin MgO layer between MZO channel and SiO₂ gate dielectric layer of the TFT. The MgO acts as a diffusion barrier, enabling to effectively reduce the Zn diffusion from MZO to SiO₂. The interface engineering decreases the total trap density N_{total} from $4.45 \times 10^{12} \text{ cm}^{-2}$ to $6.28 \times 10^{11} \text{ cm}^{-2}$ and reduces sub-threshold swing from 2.52 V/Dec to 0.413 V/Dec. The improvement is attributed to the SiO₂/MgO dual dielectric layer structure reduces Zn²⁺ charged in SiO₂ layer; The V_{gs} - V_{ds} dual-input mechanism provides the unique feature of this integrated TFT – SAW device on frequency tuning. While the gate voltage V_{gs} enables the vertical tuning mode which dominates tunability, the drain voltage V_{ds} provides the secondary tuning effect, horizontal tuning mode, to extend tuning capability and flexibility. With 0 to 12V V_{gs} biasing applied, the SAW frequency tuning can be controlled from 0.46%

to 0.63% under different V_{ds} bias. This device allows the simultaneously sensing and data process for acoustic and electrical signal, therefore, promising for portable and resettable sensors.

5.2 Suggestions for Future Work

Up to date, most tunable surface acoustic wave devices still face the challenges due to the high bias voltage requirement and the small frequency tuning range. In this dissertation, we have demonstrated a ZnO/GaN tunable SAW device with a high center frequency, high tunability, and low bias voltage. A tunable SAW device integrated with TFT is also demonstrated on a glass substrate. However, many issues need to be studied to improve the frequency tuning performances.

5.2.1 Tunable SAW on ZnO/GaN Heterostructure

The device performance with respect to the external bias and velocity tuning range is directly impacted by the efficiency of the conductivity tuning. (1) The material quality of both piezoelectric NZO and semiconducting n -ZNO needs to be further studied. The improvement of NZO leads to better piezoelectric performance and SAW response. The optimization of the n -ZnO layer can increase the electron mobility and thus achieve higher tunability. (2) The n -ZnO layer thickness can be further studied to improve SAW tuning. Current results show thinner n -ZnO layer is preferred to obtain higher frequency tunability. However, with further reducing n -ZnO thickness, the interface scattering increases the influence on carrier mobility. Therefore, thorough understanding and optimum design of the ZnO/GaN heterojunction is needed. (3) Instead of ZnO/GaN junction, using $Mg_xZn_{1-x}O/ZnO$ heterostructure on $c\text{-Al}_2O_3$ or $r\text{-Al}_2O_3$ substrates can also form two-dimensional electron gas (2DEG) which provides high electron mobility. The continuous growth of

$\text{Mg}_x\text{Zn}_{1-x}\text{O}/\text{ZnO}$ provides a better interface; that results in the tunable SAW devices with larger tunability, smaller bias, and faster response. (4) The current highest SAW center frequency is 1.35 GHz using minimum feature IDT of 1.5 μm . With the further shrinking of IDT dimension to sub-micron and even the nanometer level, multi-GHz operation can be achieved with a larger frequency tuning range.

To further solve the energy loss, the acousto-electric amplification effect (AE) can be incorporated into the tunable SAW design. When an acoustic wave travels in a piezoelectric medium, it produces an accompanying electric field parallel to the direction of propagation. In addition to the acoustic wave, if a biasing electric field is imposed in the same direction, the resulting drift current will interact with the acoustic wave. The acoustic wave velocity is substantially constant, but the velocity of the drift charges can be adjusted by changing the bias field and depends on the mobility of the charge carriers. When the drift velocity of the charge carriers is less than that of the acoustic wave, energy is removed from the acoustic wave, and it is attenuated as it travels. However, when the drift velocity of the charged carriers is greater than the acoustic wave velocity, the acoustic wave is amplified as it propagates in the region of interaction. The amplification of acoustic wave through the electrical field is also referred as acousto-electric amplification effect (AE). Two parallel electrodes placed between two IDT sets can generate an electrical field which compensates the energy loss and improves the signal quality.

5.2.2 Tunable SAW on Multifunctional MZO/ZnO Structure

Glass substrate, due to its transparency and low cost, has been widely used in display technology and disposable applications. Especially with the development of high-quality, flexible glass, it is possible to develop wearable devices and systems on glass.

Tunable SAW on glass provides several advantages: (1) potential integration with display technology, especially the SAW touch screen display; (2) large area and high volume manufacturing, compatible with the system on glass (SOG) fabrication technology; (3) flexible glass or other flexible substrates for configurable “smart” wearable electronics.

Tunable SAW device on glass demonstrates the feasibility of low cost and large area tunable SAW device technology. Besides the regular vertical voltage V_{gs} tuning, the additional frequency tunability is achieved using V_{ds} . (1) The simulation shows that the increase of dielectric layer thickness can increase electromechanical coupling coefficient; however, results in a higher biasing voltage. The high dielectric constant (high-k) materials such as HfO_2 and Al_2O_3 , hold a large capacitance at the same dielectric layer thickness, which reduces the gate biasing voltage; (2) Ga-doped ZnO (GZO), which is an excellent transparent conductive oxide (TCO) replaces the Cr gate metallization scheme to realize fully transparent tunable SAW devices on the bendable glass. (3) In the current device, the direction of electrical current in TFT is perpendicular to SAW traveling direction. It is interesting to design the integrated TFT-SAW device where the TFT current and SAW wave in parallel to achieve the acousto-electric amplification through the photon-electron interaction in the same direction. Thus, the surface acoustic wave can be accelerated or decelerated by the horizontal electric field, which could further improve frequency tunability and signal to noise ratio.

Appendix

For general elastic materials, the linear deformation is governed by Hooke's Law:

$$T = cS \quad (\text{A.1})$$

where T is compressional stress, S is strain along the same axis and c is elastic stiffness coefficient, also known as Young's modulus. In 3-dimension crystal structure, considering all possible components of stress and strain, Eqn. (2.2) needs to be expressed into a tensor form:

$$(T) = (c) : (S) \quad (\text{A.2})$$

where (T) and (S) are classed as second order tensors and (c) is referred to as a fourth order tensor. Due to the symmetry of the crystal ($T_{ij}=T_{ji}$, $S_{ij}=S_{ji}$), the stress and strain can be reduced to single suffix instead of two as:

$$\begin{aligned} T_1 &= T_{11}, T_2 = T_{22}, T_3 = T_{33} \\ T_4 &= T_{32} = T_{23}, T_5 = T_{31} = T_{13}, T_6 = T_{12} = T_{21} \\ S_1 &= S_{11}, S_2 = S_{22}, S_3 = S_{33} \\ S_4 &= 2S_{32} = 2S_{23}, S_5 = 2S_{31} = 2S_{13}, S_6 = 2S_{12} = 2S_{21} \end{aligned} \quad (\text{A.3})$$

Tensor Eq. (2.2) can be reduced to a matrix equation $[T] = [c] [S]$. In this way, the elastic stiffness constant is reduced to a 6×6 matrix $[c]$. Now, Hooke's Law becomes:

$$\begin{bmatrix} T_1 \\ T_2 \\ T_3 \\ T_4 \\ T_5 \\ T_6 \end{bmatrix} = \begin{bmatrix} c_{11} & c_{12} & c_{13} & c_{14} & c_{15} & c_{16} \\ c_{21} & c_{22} & c_{23} & c_{24} & c_{25} & c_{26} \\ c_{31} & c_{32} & c_{33} & c_{34} & c_{35} & c_{36} \\ c_{41} & c_{42} & c_{43} & c_{44} & c_{45} & c_{46} \\ c_{51} & c_{52} & c_{53} & c_{54} & c_{55} & c_{56} \\ c_{61} & c_{62} & c_{63} & c_{64} & c_{65} & c_{66} \end{bmatrix} \begin{bmatrix} S_1 \\ S_2 \\ S_3 \\ S_4 \\ S_5 \\ S_6 \end{bmatrix} \quad (\text{A.4})$$

In the linear electrical behavior of the material, the electric displacement $[D]$ will be proportionally related to electric field intensity $[E]$, similar to a parallel plate capacitor. $[\varepsilon]$ is permittivity or dielectric constant of the material, which is measured at zero or constant strain. In matrix form:

$$[D] = [\varepsilon] [E] \quad (\text{A.5})$$

Due to the interaction in piezoelectric materials, the electrical and mechanical parameters are coupled. By introducing the piezoelectric constant matrix $[e]$ and its transpose matrix $[d]$, the general piezoelectric equations of state are given below:

$$[T] = [c][S] - [d][E] \quad (\text{A.6})$$

$$[D] = [e][S] + [\varepsilon][E] \quad (\text{A.7})$$

Because the S term has six components, the dielectric permittivity $[\varepsilon]$ is a 3×3 matrix with 9 elements and the piezoelectric constant terms in $[e]$ will form a 3×6 matrix with 18 elements.

$$[e] = \begin{bmatrix} e_{11} & e_{21} & e_{31} \\ e_{12} & e_{22} & e_{32} \\ e_{13} & e_{23} & e_{33} \\ e_{14} & e_{24} & e_{34} \\ e_{15} & e_{25} & e_{35} \\ e_{16} & e_{26} & e_{36} \end{bmatrix} \quad (\text{A.8})$$

References

- [1] J. Zhu, N. W. Emanetoglu, Y. Lu, J. A. Kosinski, and R. A. Pastore, "A multi-IDT input tunable surface acoustic wave filter," *IEEE Trans. Ultrason. Ferroelectr. Freq. Control*, vol. 48, no. 5, pp. 1383–1388, Sep. 2001.
- [2] T. Yasue, T. Komatsu, N. Nakamura, K. Y. Hashimoto, H. Hirano, M. Esashi, and S. Tanaka, "Wideband tunable Love wave filter using electrostatically actuated MEMS variable capacitors integrated on lithium niobate," *Sensors Actuators, A Phys.*, vol. 188, pp. 456–462, 2012.
- [3] H. Zhou, A. Talbi, N. Tiercelin, and O. Bou Matar, "Multilayer magnetostrictive structure based surface acoustic wave devices," *Appl. Phys. Lett.*, vol. 104, no. 11, p. 114101, Mar. 2014.
- [4] M. Pijolat, C. Deguet, C. Billard, D. Mercier, A. Reinhardt, M. Aïd, S. Ballandras, and E. Defay, "Bias controlled electrostrictive longitudinal resonance in X-cut lithium niobate thin films resonator," *Appl. Phys. Lett.*, vol. 98, no. 23, p. 232902, 2011.
- [5] S. Alzuaga, W. Daniau, R. Salut, T. Baron, S. Ballandras, and E. Defay, "Tunable and high quality factor SrTiO₃ surface acoustic wave resonator," *Appl. Phys. Lett.*, vol. 105, no. 6, p. 62901, Aug. 2014.
- [6] A. Wixforth, J. Scriba, M. Wassermeier, J. Kotthaus, G. Weimann, and W. Schlapp, "Surface acoustic waves on GaAs/Al_xGa_{1-x}As heterostructures," *Phys. Rev. B*, vol. 40, no. 11, pp. 7874–7887, Oct. 1989.
- [7] J. Pedrós, F. Calle, R. Cuervo, J. Grajal, and Z. Bougrioua, "Voltage tunable surface acoustic wave phase shifter on AlGa_N/Ga_N," *Appl. Phys. Lett.*, vol. 96, no. 12, p. 123505, 2010.
- [8] J. Zhu, Y. Chen, G. Saraf, N. W. Emanetoglu, and Y. Lu, "Voltage tunable surface acoustic wave phase shifter using semiconducting/piezoelectric ZnO dual layers grown on r-Al₂O₃," *Appl. Phys. Lett.*, vol. 89, no. 10, p. 103513, 2006.
- [9] M. Rotter, W. Ruile, A. Wixforth, and J. P. Kotthaus, "Voltage controlled saw velocity in gaas/linbo₃-hybrids," *IEEE Trans. Ultrason. Ferroelectr. Freq. Control*, vol. 46, no. 1, pp. 120–125, 1999.
- [10] Y. Chen, N. W. Emanetoglu, G. Saraf, P. Wu, Y. Lu, A. Parekh, V. Merai, E. Udovich, D. Lu, D. S. Lee, E. A. Armour, and M. Pophristic, "Analysis of SAW properties in ZnO/Al_xGa_{1-x}N/c-Al₂O₃ structures," *IEEE Trans. Ultrason. Ferroelectr. Freq. Control*, vol. 52, no. 7, pp. 1161–9, Jul. 2005.
- [11] A. L. Kholkin, N. A. Pertsev, and A. V. Goltsev, "Piezoelectricity and Crystal Symmetry," in *Piezoelectric and Acoustic Materials for Transducer Applications*,

Boston, MA: Springer US, 2008, pp. 17–38.

- [12] L. Rayleigh, “On Waves Propagated along the Plane Surface of an Elastic Solid,” *Proc. London Math. Soc.*, vol. s1-17, no. 1, pp. 4–11, Nov. 1885.
- [13] L. Braile, “Seismic Wave Demonstrations and Animations,” *Review Literature And Arts Of The Americas*, 2016. [Online]. Available: <http://web.ics.purdue.edu/~braile/edumod/waves/WaveDemo.htm>.
- [14] R. M. White and F. W. Voltmer, “DIRECT PIEZOELECTRIC COUPLING TO SURFACE ELASTIC WAVES,” *Appl. Phys. Lett.*, vol. 7, no. 12, p. 314, 1965.
- [15] A. V. Mamishev, K. Sundara-Rajan, F. Yang, Y. Du, and M. Zahn, “Interdigital sensors and transducers,” *Proc. IEEE*, vol. 92, no. 5, pp. 808–844, 2004.
- [16] A. Coon, “SAW filters and competitive technologies: a comparative review,” in *IEEE 1991 Ultrasonics Symposium*, 1991, pp. 155–160.
- [17] R. M. Hays and C. S. Hartmann, “Surface-acoustic-wave devices for communications,” *Proc. IEEE*, vol. 64, no. 5, pp. 652–671, 1976.
- [18] J. D. Maines and E. G. S. Paige, “Surface-acoustic-wave devices for signal processing applications,” *Proc. IEEE*, vol. 64, no. 5, pp. 639–652, 1976.
- [19] M. Lewis, “SAW and Optical Signal Processing,” in *IEEE Ultrasonics Symposium*, 2005, pp. 800–809.
- [20] M. Penza, G. Cassano, A. Sergi, C. Lo Sterzo, and M. . Russo, “SAW chemical sensing using poly-yenes and organometallic polymer films,” *Sensors Actuators B Chem.*, vol. 81, no. 1, pp. 88–98, Dec. 2001.
- [21] A. J. Ricco, R. M. Crooks, and G. C. Osbourn, “Surface Acoustic Wave Chemical Sensor Arrays : New Chemically Sensitive Interfaces Combined with Novel Cluster Analysis To Detect Volatile Organic Compounds and Mixtures,” *Acc. Chem. Res.*, vol. 31, no. 5, pp. 289–296, 1998.
- [22] F. Guo, P. Li, J. B. French, Z. Mao, H. Zhao, S. Li, N. Nama, J. R. Fick, S. J. Benkovic, and T. J. Huang, “Controlling cell–cell interactions using surface acoustic waves,” *Proc. Natl. Acad. Sci.*, vol. 112, no. 1, pp. 43–48, 2015.
- [23] D. J. Collins, B. Morahan, J. Garcia-Bustos, C. Doerig, M. Plebanski, and A. Neild, “Two-dimensional single-cell patterning with one cell per well driven by surface acoustic waves,” *Nat. Commun.*, vol. 6, p. 8686, Nov. 2015.
- [24] H. Jin, J. Zhou, X. He, W. Wang, H. Guo, S. Dong, D. Wang, Y. Xu, J. Geng, J. K. Luo, and W. I. Milne, “Flexible surface acoustic wave resonators built on disposable plastic film for electronics and lab-on-a-chip applications,” *Sci. Rep.*, vol. 3, no. 2, pp. 1–8, Jul. 2013.
- [25] Y. Bourquin, J. Reboud, R. Wilson, Y. Zhang, and J. M. Cooper, “Integrated

immunoassay using tuneable surface acoustic waves and lensfree detection,” *Lab Chip*, vol. 11, no. 16, p. 2725, 2011.

- [26] D. Penunuri, R. Komrmusch, and N. Mellen, “A tunable SAW duplexer,” in *2000 IEEE Ultrasonics Symposium. Proceedings. An International Symposium (Cat. No.00CH37121)*, 2000, vol. 1, pp. 361–366.
- [27] X. Lu, J. Galipeau, K. Mouthaan, E. H. Briot, and B. Abbott, “Reconfigurable multiband SAW filters for LTE applications,” in *2013 IEEE Topical Conference on Biomedical Wireless Technologies, Networks, and Sensing Systems*, 2013, pp. 76–78.
- [28] M. Kadota, T. Kimura, and Y. Ida, “Ultra wide band resonator composed of grooved Cu-electrode on LiNbO₃ and its application to tunable filter,” in *2009 IEEE International Ultrasonics Symposium*, 2009, vol. 1, no. 2, pp. 2668–2671.
- [29] H. Hirano, T. Samoto, T. Kimura, M. Inaba, K. Y. Hashimoto, T. Matsumura, K. Hikichi, M. Kadota, M. Esashi, and S. Tanaka, “Bandwidth-tunable SAW filter based on wafer-level transfer-integration of BaSrTiO₃ film for wireless LAN system using TV white space,” *IEEE Int. Ultrason. Symp. IUS*, pp. 803–806, 2014.
- [30] R. A. York, “Tunable Dielectrics for RF Circuits,” *Multifunct. Adapt. Microw. Circuits Syst.*, pp. 1–54, 2009.
- [31] S. Doberstein, “Switchable low-loss SAW filter banks with MEMS switches,” in *IEEE Ultrasonics Symposium Proceedings*, 2010, pp. 1294–1297.
- [32] S.-C. S. Lin, X. Mao, and T. J. Huang, “Surface acoustic wave (SAW) acoustophoresis: now and beyond,” *Lab Chip*, vol. 12, no. 16, pp. 2766–70, Aug. 2012.
- [33] A. Hietala and W. P. Robbins, “Design Methodology for Tunable SAW Devices Using Magnetostrictive Thin Films,” in *IEEE 1986 Ultrasonics Symposium*, 1986, pp. 239–244.
- [34] W. P. Robbins and A. Hietala, “A simple phenomenological model of tunable SAW devices using magnetostrictive thin films,” *IEEE Trans. Ultrason. Ferroelectr. Freq. Control*, vol. 35, no. 6, pp. 718–22, 1988.
- [35] J. Janušonis, C. L. Chang, P. H. M. van Loosdrecht, and R. I. Tobey, “Frequency tunable surface magneto elastic waves,” *Appl. Phys. Lett.*, vol. 106, no. 18, p. 181601, 2015.
- [36] P. Smole, W. Ruile, C. Korden, A. Ludwig, E. Quandt, S. Krassnitzer, and P. Pongratz, “Magnetically tunable SAW-resonator,” in *IEEE International Frequency Control Symposium and PDA Exhibition Jointly with the 17th European Frequency and Time Forum, 2003. Proceedings of the 2003*, 2003, no. 2, pp. 903–906.
- [37] S. G. Joshi, “Electronically Tunable SAW Oscillator on Temperature Stable Quartz Substrate,” *IEEE 1984 Ultrason. Symp.*, pp. 203–206, 1984.

- [38] A. J. Budreau, P. H. Carr, and J. H. Silva, "New Configuration for Electronically Variable SAW Delay Line," *1982 Ultrason. Symp.*, pp. 399–400, 1982.
- [39] C. Campbell, *Surface acoustic wave devices for mobile and wireless communications*. Boston, MA: Academic Press, 1998.
- [40] A. R. Hutson and D. L. White, "Elastic Wave Propagation in Piezoelectric Semiconductors," *J. Appl. Phys.*, vol. 33, no. 1, p. 40, 1962.
- [41] K. A. Ingebrigtsen, "Linear and nonlinear attenuation of acoustic surface waves in a piezoelectric coated with a semiconducting film," *J. Appl. Phys.*, vol. 41, no. 1970, pp. 454–459, 1970.
- [42] F. S. Hickernell, "ZnO Processing for Bulk- and Surface-Wave Devices," *1980 Ultrason. Symp.*, pp. 785–794, 1980.
- [43] R. Kubo, H. Fujii, H. Kawamura, M. Takeuchi, K. Inoue, Y. Yoshino, T. Makino, and S. Arai, "Fabrication of 5GHz band film bulk acoustic wave resonators using ZnO thin film," in *IEEE Symposium on Ultrasonics, 2003*, 2003, vol. 0, no. c, pp. 166–169.
- [44] N. W. Emanetoglu, G. Patounakis, Shaohua Liang, C. R. Gorla, R. Wittstruck, and Yicheng Lu, "Analysis of SAW properties of epitaxial ZnO films grown on R-Al/sub 2/O/sub 3/ substrates," *IEEE Trans. Ultrason. Ferroelectr. Freq. Control*, vol. 48, no. 5, pp. 1389–1394, Sep. 2001.
- [45] T. Mitsuyu, S. Ono, and K. Wasa, "Structures and SAW properties of rf-sputtered single-crystal films of ZnO on sapphire," *J. Appl. Phys.*, vol. 51, no. 5, p. 2464, 1980.
- [46] I. S. Didenko, F. S. Hickernell, and N. F. Naumenko, "The experimental and theoretical characterization of the SAW propagation properties for zinc oxide films on silicon carbide," *IEEE Trans. Ultrason. Ferroelectr. Freq. Control*, vol. 47, no. 1, pp. 179–187, Jan. 2000.
- [47] I. S. Didenko, F. S. Hickernell, and N. F. Naumenko, "Theoretical aspects of GSAW and HVPSAW propagation properties for zinc oxide films on silicon carbide and correlation with experimental data," in *1999 IEEE Ultrasonics Symposium. Proceedings. International Symposium (Cat. No.99CH37027)*, 1999, vol. 1, no. c, pp. 313–316.
- [48] H. Nakahata, A. Hachigo, K. Itakura, and S. Shikata, "Fabrication of high frequency SAW filters from 5 to 10 GHz using SiO/sub 2//ZnO/diamond structure," in *2000 IEEE Ultrasonics Symposium. Proceedings. An International Symposium (Cat. No.00CH37121)*, 2000, vol. 1, no. Cvd, pp. 349–352.
- [49] A. Hachigo, H. Nakahata, K. Itakura, S. Fujii, and S. Shikata, "10 GHz narrow band SAW filters using diamond," in *1999 IEEE Ultrasonics Symposium. Proceedings. International Symposium (Cat. No.99CH37027)*, 1999, vol. 1, pp. 325–328.
- [50] F. Moeller, T. Vandahl, D. C. Malocha, N. Schwesinger, and W. Buff, "Properties

- of thick ZnO layers on oxidized silicon,” *Proc. IEEE Ultrason. Symp. ULTSYM-94*, pp. 403–406 vol.1, 1994.
- [51] B. S. Panwar, “Characteristics of surface acoustic wave convolver in the monolithic metal–zinc oxide–silicon nitride–silicon dioxide–silicon structure,” *Appl. Phys. Lett.*, vol. 80, no. 10, p. 1832, 2002.
 - [52] Yoonkee Kim, W. D. Hunt, F. S. Hickernell, R. J. Higgins, and Cheng-Kuei Jen, “ZnO films on {001}-cut <110>-propagating GaAs substrates for surface acoustic wave device applications,” *IEEE Trans. Ultrason. Ferroelectr. Freq. Control*, vol. 42, no. 3, pp. 351–361, May 1995.
 - [53] T. Gryba, A. Haddou, V. Sadaune, V. Zhang, J. E. Lefebvre, E. Doghech, E. Cattani, and D. Remiens, “Integration of RF filters on GaAs substrate,” in *2001 IEEE Ultrasonics Symposium. Proceedings. An International Symposium (Cat. No.01CH37263)*, 2001, vol. 1, no. I, pp. 57–60.
 - [54] T. Shiba, A. Yuhara, M. Moteki, Y. Ota, K. Oda, and K. Tsubouchi, “Low loss SAW matched filters with low sidelobe sequences for spread spectrum communications,” in *1995 IEEE Ultrasonics Symposium. Proceedings. An International Symposium*, 1996, vol. 1, pp. 107–112.
 - [55] I. S. Didenko, F. S. Hickernell, and N. F. Naumenko, “The experimental and theoretical characterization of the SAW propagation properties for zinc oxide films on silicon carbide,” *IEEE Trans. Ultrason. Ferroelectr. Freq. Control*, vol. 47, no. 1, pp. 179–87, Jan. 2000.
 - [56] S. Nakamura, T. Mukai, and M. Senoh, “High-brightness InGaN/AlGaIn double-heterostructure blue-green-light-emitting diodes,” *J. Appl. Phys.*, vol. 76, no. 12, p. 8189, 1994.
 - [57] S. D. Lester, “High dislocation densities in high efficiency GaN-based light-emitting diodes,” vol. 66, no. 10, pp. 1249–1251, 2001.
 - [58] G. Popovici, W. Kim, A. Botchkarev, H. Tang, H. Morkoç, and J. Solomon, “Impurity contamination of GaN epitaxial films from the sapphire, SiC and ZnO substrates,” *Appl. Phys. Lett.*, vol. 71, no. 23, p. 3385, 1997.
 - [59] T. Nishihara, T. Yokoyama, T. Miyashita, and Y. Satoh, “High Performance and Miniature Thin Film Bulk Acoustic Wave Filters for 5 GHz,” vol. 0, no. c, pp. 969–972, 2002.
 - [60] H. P. Lobl, M. Klee, C. Metzmacher, W. Brand, R. Milsom, P. Lok, and F. van Straten, “Piezoelectric materials for BAW resonators and filters,” in *2001 IEEE Ultrasonics Symposium. Proceedings. An International Symposium (Cat. No.01CH37263)*, 2001, vol. 1, pp. 807–811.
 - [61] Y. Takagaki, P. V. Santos, E. Wiebicke, O. Brandt, H.-P. Schönherr, and K. H. Ploog, “Superhigh-frequency surface-acoustic-wave transducers using AlN layers

- grown on SiC substrates,” *Appl. Phys. Lett.*, vol. 81, no. 14, p. 2538, 2002.
- [62] T. Palacios, F. Calle, J. Grajal, E. Monroy, M. Eickhoff, O. Ambacher, and F. Omnes, “High frequency SAW devices on AlGaIn: fabrication, characterization and integration with optoelectronics,” in *2002 IEEE Ultrasonics Symposium, 2002. Proceedings.*, 2002, vol. 0, no. c, pp. 57–60.
 - [63] Y. Takagaki, P. Santos, E. Wiebicke, O. Brandt, H.-P. Schönherr, and K. Ploog, “Guided propagation of surface acoustic waves in AlN and GaN films grown on 4H-SiC(0001) substrates,” *Phys. Rev. B*, vol. 66, no. 15, p. 155439, Oct. 2002.
 - [64] K. Hohkawa, K. Koh, K. Nishimura, and N. Shigekawa, “DC Variable Harmonic Pass Band Operation of AlGaIn/GaN Surface Acoustic Wave Devices,” *Jpn. J. Appl. Phys.*, vol. 47, no. 9, pp. 7104–7107, Sep. 2008.
 - [65] K. Tsubouchi, K. Sugai, and N. Mikoshiba, “Zero Temperature Coefficient Surface-Acoustic-Wave Devices Using Epitaxial AlN Films,” in *1982 Ultrasonics Symposium*, 1982, no. 1, pp. 340–345.
 - [66] K. Uehara, H. Nakamura, H. Nakase, and K. Tsubouchi, “AlN epitaxial film with atomically flat surface for GHz-band SAW devices,” in *2002 IEEE Ultrasonics Symposium, 2002. Proceedings.*, 2002, vol. 0, no. c, pp. 135–138.
 - [67] Suk-Hun Lee, Hwan-Hee Jeong, Sung-Bum Bae, Hyun-Chul Choi, Jung-Hee Lee, and Yong-Hyun Lee, “Epitaxially grown GaN thin-film SAW filter with high velocity and low insertion loss,” *IEEE Trans. Electron Devices*, vol. 48, no. 3, pp. 524–529, Mar. 2001.
 - [68] Young-Jin Kim, Gune Hwan Lim, Kook Hyun Choi, Su Jin Chung, Hyeong Joon Kim, Haesung Park, and Hyeong Soo Park, “SAW characteristics of GaN epitaxial films deposited on different plane sapphire substrates using MOCVD,” in *2002 IEEE Ultrasonics Symposium, 2002. Proceedings.*, 2002, vol. 0, no. c, pp. 427–430.
 - [69] K. Brueckner, F. Niebelschuetz, K. Tonisch, S. Michael, A. Dadgar, A. Krost, V. Cimalla, O. Ambacher, R. Stephan, and M. a. Hein, “Two-dimensional electron gas based actuation of piezoelectric AlGaIn/GaN microelectromechanical resonators,” *Appl. Phys. Lett.*, vol. 93, no. 17, p. 173504, 2008.
 - [70] K.-Y. Wong, W. Tang, K. M. Lau, and K. J. Chen, “Surface acoustic wave device on AlGaIn/GaN heterostructure using two-dimensional electron gas interdigital transducers,” *Appl. Phys. Lett.*, vol. 90, no. 21, p. 213506, 2007.
 - [71] T. Detchprohm, K. Hiramatsu, H. Amano, and I. Akasaki, “Hydride vapor phase epitaxial growth of a high quality GaN film using a ZnO buffer layer,” *Appl. Phys. Lett.*, vol. 61, no. 22, p. 2688, 1992.
 - [72] W. Götz, L. T. Romano, J. Walker, N. M. Johnson, and R. J. Molnar, “Hall-effect analysis of GaN films grown by hydride vapor phase epitaxy,” *Appl. Phys. Lett.*, vol. 72, no. 10, p. 1214, 1998.

- [73] S. Gu, R. Zhang, J. Sun, L. Zhang, and T. F. Kuech, "Role of interfacial compound formation associated with the use of ZnO buffers layers in the hydride vapor phase epitaxy of GaN," *Appl. Phys. Lett.*, vol. 76, no. 23, p. 3454, 2000.
- [74] A. Nahhas, H. K. Kim, and J. Blachere, "Epitaxial growth of ZnO films on Si substrates using an epitaxial GaN buffer," *Appl. Phys. Lett.*, vol. 78, no. 11, p. 1511, 2001.
- [75] S.-K. Hong, T. Hanada, H. Makino, Y. Chen, H.-J. Ko, T. Yao, A. Tanaka, H. Sasaki, and S. Sato, "Band alignment at a ZnO/GaN (0001) heterointerface," *Appl. Phys. Lett.*, vol. 78, no. 21, p. 3349, 2001.
- [76] D. C. Oh, T. Suzuki, J. J. Kim, H. Makino, T. Hanada, M. W. Cho, T. Yao, J. S. Song, and H. J. Ko, "Electrical characterization for ZnO layers grown on GaN templates by molecular-beam epitaxy," *J. Vac. Sci. Technol. B Microelectron. Nanom. Struct.*, vol. 23, no. 3, p. 1281, 2005.
- [77] J. O. Song, K.-K. Kim, S.-J. Park, and T.-Y. Seong, "Highly low resistance and transparent Ni/ZnO ohmic contacts to p-type GaN," *Appl. Phys. Lett.*, vol. 83, no. 3, p. 479, 2003.
- [78] Y. I. Alivov, J. E. Van Nostrand, D. C. Look, M. V. Chukichev, and B. M. Ataev, "Observation of 430 nm electroluminescence from ZnO/GaN heterojunction light-emitting diodes," *Appl. Phys. Lett.*, vol. 83, no. 14, p. 2943, 2003.
- [79] J. Zhong, H. Chen, G. Saraf, Y. Lu, C. K. Choi, J. J. Song, D. M. Mackie, and H. Shen, "Integrated ZnO nanotips on GaN light emitting diodes for enhanced emission efficiency," *Appl. Phys. Lett.*, vol. 90, no. 20, p. 203515, 2007.
- [80] Y. Chen, G. Saraf, Y. Lu, L. S. Wielunski, and T. Siegrist, "a-plane $\text{Mg}_x\text{Zn}_{1-x}\text{O}$ films deposited on r-sapphire and its surface acoustic wave characteristics," *J. Vac. Sci. Technol. A Vacuum, Surfaces, Film.*, vol. 25, no. 4, p. 857, 2007.
- [81] M. M. De Lima and P. V Santos, "Modulation of photonic structures by surface acoustic waves," *Reports Prog. Phys.*, vol. 68, no. 7, pp. 1639–1701, Jul. 2005.
- [82] D. L. Smythe, "A surface-acoustic wave/metal-oxide-silicon field-effect transistor memory correlator," *Appl. Phys. Lett.*, vol. 38, no. 11, p. 886, 1981.
- [83] J. B. Green, G. S. Kino, J. T. Walker, and J. O. Shott, "The SAW/FET: A New Programmable SAW Transversal Filter," in *1982 Ultrasonics Symposium*, 1982, pp. 436–441.
- [84] J. B. Green, "Integrated surface acoustic wave/field-effect transistor high-speed analog memory," *Appl. Phys. Lett.*, vol. 42, no. 12, p. 1015, 1983.
- [85] D. E. Oates, D. L. Smythe, and J. B. Green, "SAW/FET Programmable Transversal Filter with 100-MHz Bandwidth and Enhanced Programmability," in *IEEE 1985 Ultrasonics Symposium*, 1985, pp. 124–129.

- [86] J. B. Green and G. S. Kino, "The SAW-FET Signal Processor," *IEEE Trans. Sonics Ultrason.*, vol. 32, no. 5, pp. 734–744, Sep. 1985.
- [87] J. B. Green, D. E. Oates, P. M. Grant, and D. L. Smythe, "Adaptive and Matched Filtering with a SAW/FET Programmable Transversal Filter," in *IEEE 1986 Ultrasonics Symposium*, 1986, pp. 137–142.
- [88] D. E. Oates, D. L. Smythe, J. B. Green, and R. S. Withers, "SAW/FET programmable filter with varistor taps for improved performance," in *IEEE 1988 Ultrasonics Symposium Proceedings.*, 1988, pp. 155–158.
- [89] I. Rýger, G. Vanko, T. Lalinský, M. Valloa, M. Tomáška, and A. Ritomský, "AlGa_N/Ga_N based SAW-HEMT devices for chemical gas sensors operating in GHz range," *Procedia Eng.*, vol. 25, pp. 1101–1104, 2011.
- [90] X. Lu, J. Ma, X. L. Zhu, C. M. Lee, C. P. Yue, and K. M. Lau, "A novel Ga_N-based monolithic SAW/HEMT oscillator on silicon," in *2012 IEEE International Ultrasonics Symposium*, 2012, pp. 2206–2209.
- [91] O. Satoshi, K. Koh, and K. Hohkawa, "A basic study on SAW resonator with AlGa_N/Ga_N film," *Proc. Symp. Ultrason. Electron.*, vol. 30, pp. 277–278, 2009.
- [92] L. Shao, M. Zhang, A. Banerjee, P. Bhattacharya, and K. P. Pipe, "Emission and detection of surface acoustic waves by AlGa_N/Ga_N high electron mobility transistors," *Appl. Phys. Lett.*, vol. 99, no. 24, pp. 12–15, 2011.
- [93] C. G. Van De Walle, "Hydrogen as a cause of doping in zinc oxide," *Phys. Rev. Lett.*, vol. 85, no. 5, pp. 1012–1015, 2000.
- [94] A. Janotti and C. G. Van de Walle, "Hydrogen multicentre bonds," *Nat. Mater.*, vol. 6, no. 1, pp. 44–47, 2007.
- [95] S. Lee, H. Jeong, S. Bae, H. Choi, J. Lee, and Y. Lee, "Epitaxially grown Ga_N thin-film SAW filter with high velocity and low insertion loss," *IEEE Trans. Electron Devices*, vol. 48, no. 3, pp. 524–529, Mar. 2001.
- [96] K. Inoue and K. Sato, "Propagation Characteristics of Surface Acoustic Waves on Langasite," *Jpn. J. Appl. Phys.*, vol. 37, no. Part 1, No. 5B, pp. 2909–2913, 1998.
- [97] R. Li, P. I. Reyes, S. Ragavendiran, H. Shen, and Y. Lu, "Tunable surface acoustic wave device based on acoustoelectric interaction in ZnO/Ga_N heterostructures," *Appl. Phys. Lett.*, vol. 107, no. 7, p. 73504, Aug. 2015.
- [98] C.-J. Ku, Z. Duan, P. I. Reyes, Y. Lu, Y. Xu, C.-L. Hsueh, and E. Garfunkel, "Effects of Mg on the electrical characteristics and thermal stability of Mg_[sub x]Zn_[sub 1-x]O thin film transistors," *Appl. Phys. Lett.*, vol. 98, no. 12, p. 123511, 2011.
- [99] C.-J. Ku, W.-C. Hong, T. Mohsin, R. Li, Z. Duan, and Y. Lu, "Improvement of Negative Bias Stress Stability in Mg_{0.03}Zn_{0.97}O Thin-Film Transistors," *IEEE Electron Device Lett.*, vol. 36, no. 9, pp. 914–916, 2015.

- [100] Y. Chen, P. I. Reyes, Z. Duan, G. Saraf, R. Wittstruck, Y. Lu, O. Taratula, and E. Galoppini, "Multifunctional ZnO-Based Thin-Film Bulk Acoustic Resonator for Biosensors," *J. Electron. Mater.*, vol. 38, no. 8, pp. 1605–1611, Aug. 2009.
- [101] A. H. Fahmy and E. L. Adler, "Propagation of acoustic surface waves in multilayers: A matrix description," *Appl. Phys. Lett.*, vol. 22, no. 10, pp. 495–497, 1973.
- [102] P. Ventura, P. Dufilie, and F. Hecht, "Optimized STW devices with buried electrodes based on a mixed FEM/BEM numerical model," in *2011 IEEE International Ultrasonics Symposium*, 2011, pp. 563–567.
- [103] C. Caliendo, "Analytical Study of the Propagation of Fast Longitudinal Modes along wz-BN/AlN Thin Acoustic Waveguides," *Sensors*, vol. 15, no. 2, pp. 2525–2537, Jan. 2015.
- [104] M. Solal, J. Gratier, R. Aigner, K. Gamble, B. Abbott, T. Kook, A. Chen, and K. Steiner, "A method to reduce losses in buried electrodes RF SAW resonators," in *2011 IEEE International Ultrasonics Symposium*, 2011, pp. 324–332.
- [105] G. a Slack, "Thermal Conductivity of MgO, Al₂O₃, MgAl₂O₄, and Fe₂O₄ Crystals from 3 to 300 K," *Phys. Rev.*, vol. 126, no. 2, pp. 427–441, 1962.
- [106] M. A. Subramanian, R. D. Shannon, B. H. T. Chai, M. M. Abraham, and M. C. Wintersgill, "Dielectric constants of BeO, MgO, and CaO using the two-terminal method," *Phys. Chem. Miner.*, vol. 16, no. 8, pp. 741–746, Nov. 1989.
- [107] Y. Chen, H.-J. Ko, S.-K. Hong, and T. Yao, "Layer-by-layer growth of ZnO epilayer on Al₂O₃(0001) by using a MgO buffer layer," *Appl. Phys. Lett.*, vol. 76, no. 5, p. 559, 2000.
- [108] J. Goo, S. Kyu, S. Mo, S. Hong, J. Wook, J. Yong, J. Song, Y. Eon, D. Kim, J. Sub, H. Lee, and T. Yao, "Effects of low temperature ZnO and MgO buffer thicknesses on properties of ZnO films grown on (0001) Al₂O₃ substrates by plasma-assisted molecular beam epitaxy," *Thin Solid Films*, vol. 519, no. 1, pp. 223–227, 2010.
- [109] H. Q. Huang, F. J. Liu, J. Sun, J. W. Zhao, Z. F. Hu, Z. J. Li, X. Q. Zhang, and Y. S. Wang, "Effect of MgO buffer layer thickness on the electrical properties of MgZnO thin film transistors fabricated by plasma assisted molecular beam epitaxy," *Appl. Surf. Sci.*, vol. 257, no. 24, pp. 10721–10724, Oct. 2011.
- [110] K. M. Iyamato, M. S. Ano, H. K. Ato, and T. Y. Ao, "Effects of ZnO / MgO Double Buffer Layers on Structural Quality and Electron Mobility of ZnO Epitaxial Films Grown on c -Plane Sapphire," *Jpn. J. Appl. Phys.*, vol. 41, no. 11, pp. 1203–1205, Nov. 2002.
- [111] A. Setiawan, H. J. Ko, and T. Yao, "Effects of annealing of MgO buffer layer on structural quality of ZnO layers grown by P-MBE on c-sapphire," *Mater. Sci. Semicond. Process.*, vol. 6, no. 5–6, pp. 371–374, Oct. 2003.
- [112] H. Zhou, H. Q. Wang, Y. Li, K. Li, J. Kang, J. C. Zheng, Z. Jiang, Y. Huang, L. Wu,

- L. Zhang, K. Kisslinger, and Y. Zhu, "Evolution of wurtzite ZnO films on cubic MgO (001) substrates: A structural, optical, and electronic investigation of the misfit structures," *ACS Appl. Mater. Interfaces*, vol. 6, no. 16, pp. 13823–13832, Aug. 2014.
- [113] M. Xue, Q. Guo, K. Wu, and J. Guo, "Initial Oxidation and Interfacial Diffusion of Zn on Faceted MgO(111) Films," *Langmuir*, vol. 24, no. 16, pp. 8760–8764, Aug. 2008.
- [114] M. K. Ryu, S. Yang, S. H. K. Park, C. S. Hwang, and J. K. Jeong, "High performance thin film transistor with cosputtered amorphous Zn-In-Sn-O channel: Combinatorial approach," *Appl. Phys. Lett.*, vol. 95, no. 7, pp. 8–11, 2009.

Publications

1. **Rui Li**, Pavel I. Reyes, Sowmya Ragavendiran, H. Shen and Yicheng Lu*, “Tunable Surface Acoustic Device Based on Acoustoelectric Interaction in ZnO/GaN heterostructures”, Applied Physics Letters 107, 073504, 2015
2. **Rui Li**, Guangyuan Li, Wen-Chiang Hong, Pavel I. Reyes, Ke Tang, Keyang Yang, Szu-Ying Wang, Hongfei Ye, Yuxuan Li, Lihua Zhang, Kim Kisslinger and Yicheng Lu*, “Tunable surface, acoustic wave device using semiconducting MgZnO and piezoelectric NiZnO dual-layer structure on glass”, Advanced Materials Technologies, 2016, (Submitted)
3. **Rui Li**, Pavel Ivanoff Reyes, Guangyuan Li, Ke Tang, Keyang Yang, Szu-Ying Wang, Jingjing Han and Yicheng Lu*, “Tunable SAW Devices Based on Ni:ZnO/ZnO/GaN Structures with Buried IDTs”, Journal of Vacuum Science and Technology A, (To be submitted)
4. Yang Zhang, **Rui Li**, Lihua Zhang, Kim Kisslinger, Pavel I. Reyes, Tengfei Xu, Wen-Chiang Hong, Yicheng Lu*, “Effect of Compliance Current on Multiple Switching Modes in ZnO-based Resistive Random Access Memory”, Journal of Vacuum Science and Technology B, 2016 (Submitted)
5. Wen-Chiang Hong, Chieh-Jen Ku, **Rui Li**, Siamak Abbaslou, Pavel I. Reyes, Szu-Ying Wang, Guangyuan Li, Ming Lu, Kuang Sheng, Yicheng Lu*, “MgZnO High Voltage Thin Film Transistors on Glass for Inverters in Building Integrated Photovoltaics”, Scientific Reports, 2016, 6, 34169
6. Pavel I. Reyes, Keyang Yang, Andrew Zheng, **Rui Li**, Guangyuan Li, Yicheng Lu*, Chi Kwan Tsang, Steven X.F. Zheng, “Dynamic monitoring of antimicrobial resistance using magnesium zinc oxide nanostructure-modified quartz crystal microbalance”, Biosensors and Bioelectronics, 2016 (In Press)
7. Chieh-Jen Ku, Wen-Chiang Hong, Tanvir Mohsin, **Rui Li**, Ziqing Duan, and Yicheng Lu*, “Improvement of Negative Bias Stress Stability in $\text{Mg}_{0.03}\text{Zn}_{0.97}\text{O}$ Thin Film Transistors”, IEEE Electron Device Letters, September 2015, VOL. 36, NO. 9
8. Chieh-Jen Ku, Pavel I. Reyes, Ziqing Duan, Wen-Chiang Hong, **Rui Li**, and Yicheng Lu*, “ $\text{Mg}_x\text{Zn}_{1-x}\text{O}$ Thin-Film Transistor-Based UV Photodetector with Enhanced Photo Response”, Journal of Electronic Material, March 2015, Volume 44, Issue 10, pp 3471-3476
9. Yang Zhang, Ziqing Duan, **Rui Li**, Chieh-Jen Ku, Pavel I. Reyes, Almamun Ashrafi, Jian Zhong and Yicheng Lu*, “Vertically integrated ZnO-Based 1D1R structure for resistive switching”, J. Phys. D: Appl. Phys. 2013 ,46 145101
10. Yang Zhang, Ziqing Duan, **Rui Li**, Chieh-Jen Ku, Pavel I. Reyes, Almamun Ashrafi, and Yicheng Lu*, “FeZnO-Based Resistive Switching Devices”, Journal of Electronic Material, October 2012, Volume 41, Issue 10, pp 2880-2885

Patent

Yicheng Lu, Wen-Chiang Hong, C. J. Ku, Kuang Sheng, **Rui Li**, “ZnO-based high voltage thin film transistor (HVTFT)”, The U.S. Provisional Application (62/377,317), October 2016